DOCTOR OF PHILOSOPHY

An assessment of CFD applied to a catalytic converter system with planar diffuser

Porter, Sophie Jane

Award date:
2016

Awarding institution:
Coventry University

AN ASSESSMENT OF CFD APPLIED TO A CATALYTIC CONVERTER SYSTEM WITH PLANAR DIFFUSER

Sophie Jane Porter

A thesis submitted in partial fulfilment of the University's requirements for the Degree of Doctor of Philosophy

June 2016

ABSTRACT

Catalytic converters are widely used in the automotive industry to comply with increasingly stringent emissions regulations. The flow distribution across the catalyst substrate significantly affects its conversion efficiency. Measuring the flow in a catalyst system is challenging; computational fluid dynamics (CFD) provides an alternative approach for the assessment of different design concepts and is therefore commonly employed to model flow behaviour. This thesis studies the application of CFD to modelling flow in a two-dimensional system consisting of a catalyst monolith downstream of a wide-angled planar diffuser, with total included angle 60°.

Computational models are developed using the commercial CFD software STAR-CCM+. Flow predictions are compared to experimental data collected by Mat Yamin, (2012) and also as part of this study. Measurements were obtained on a two-dimensional isothermal flow rig using particle image velocimetry (PIV) and hot-wire anemometry (HWA).

Steady flow studies compare different methods of modelling the monolith. Models include the common approach of modelling the monolith as a porous medium and the computationally expensive individual channels model. A hybrid model is developed that combines the two approaches, benefiting from the respective merits of each method. Two monolith lengths are considered, with flow at varying Reynolds numbers.

The porous model predicts the downstream velocity profile well for the shorter monolith but overpredicts flow maldistribution for the longer monolith. The inclusion of an entrance effect to account for the pressure losses associated with oblique entry into the monolith channels is studied. Best agreement in downstream velocity is observed when the pressure losses are limited using a critical angle approach.

The individual channels model is found to be the most consistently accurate across monolith lengths, attributable to the accurate capture of flow behaviour upon entry into the monolith channels. A novel hybrid model is proposed, which combines the computational efficiency of the porous model with the geometrical accuracy of individual channels. The model is evaluated and is found to provide results similar to the individual channels model, with

improved predictions of velocity maxima and minima.

Pulsating flow studies present three transient flow regimes with similar inlet pulse shapes and varying Reynolds number and frequency. Predicted velocities in the diffuser are in good agreement with PIV flow fields, however CFD predicts higher magnitudes at the shear layer. The model predicts large residual vortices present at the end of the cycle where experimental data shows none; it is concluded that CFD underpredicts turbulence diffusion. Evidence of cyclic variation in experimental data highlights the limitation of URANS turbulence models.

Acknowledgements

I would like to express my sincere gratitude to my director of studies, Dr Svetlana Aleksandrova, for her continued support and guidance throughout my PhD. I greatly appreciate the friendship and encouragement she has offered me.

I am extremely grateful to have worked under the supervision of Prof. Stephen Benjamin, Dr Humberto Medina and Dr Carol Roberts. Their passion and encouragement have contributed immeasurably to the successful completion of this thesis.

I also thank my colleague, Mr Jonothan Saul, for his support and camaraderie. I wish him every success with the continuation of his doctoral studies.

I would also like to express my appreciation for the technical assistance provided by Mr Robert Gartside and Mr Lawrance King.

Publications

This work has contributed to the following publications:

Porter, S. J., Mat Yamin, A. K., Aleksandrova, S., Benjamin, S. F., Roberts, C. A., and Saul, J. M. (2014). 'An assessment of CFD applied to steady flow in a planar diffuser upstream of an automotive catalyst monolith'. *SAE International Journal of Engines* 7: 1697-1704. DOI: 10.4271/2014-01-2588.

Porter, S. J., Saul, J. M., Mat Yamin, A. K., Aleksandrova, S., Benjamin, S. F., and Medina, H. J. (2015). 'Pulsating Flow in a Planar Diffuser Upstream of Automotive Catalyst Monoliths: A CFD Study'. *10^{th} Pacific Symposium on Flow Visualization and Image Processing.* Naples, Italy, June 2015.

Saul, J. M., Porter, S. J., Mat Yamin, A. K., Medina, H. J., Aleksandrova, S., and Benjamin, S. F. (2015) 'Influence of cycle variance on the performance of URANS for pulsating flow upstream of an automotive catalyst monolith'. Proceedings of the IMechE Internal Combustion Engines Conference, London, December 2015.

Medina, H. J., Beechook, A., Saul, J. M., Porter, S. J., Aleksandrova, S., and Benjamin, S. F. (2015). 'Open source Computational Fluid Dynamics using OpenFOAM'. *Light Aircraft Design: Methods and Tools. Royal Aeronautical Society, General Aviation Conference.* London, November 2015.

Porter, S. J., Saul, J. M., Aleksandrova, S., Medina, H. J., and Benjamin, S. F. (In press). 'Hybrid Flow Modelling Approach Applied to Automotive Catalysts'. *Applied Mathematical Modelling.* DOI: 10.1016/j.apm.2016.04.024.

Contents

Figures

Tables

Nomenclature

Abbreviations

CCD	charge coupled device
CFD	computational fluid dynamics
CFL	Courant-Friedrichs-Lewy
DNS	direct numerical simulation
DPF	diesel particulate filter
H-P	Hagen-Poiseuille
HC	hydrocarbon
HWA	hot-wire anemometry
K-W	Küchemann-Weber
LDV	laser doppler velocimetry
LES	large eddy simulation
NO_X	nitrogen oxide
PIV	particle image velocimetry
PM	particulate matter
PN	particle number
RANS	Reynolds-averaged Navier-Stokes
RST	Reynolds Stress Transport
SIMPLE	Semi-Implicit Method for Pressure Linked Equations
TWC	three-way catalyst

Greek Symbols

α	angle of attack, $^\circ$
α_c	critical angle, $^\circ$
α_s	subcritical angle, $^\circ$
$\alpha_{c,v}$	critical angle dependent on flow rate, $^\circ$

β	axial porous viscous resistance tensor coefficient
Δh	change in water elevation, m
ΔP	pressure drop, Pa
ΔP^*	non-dimensional pressure loss, $(\Delta P)/(\frac{1}{2}\rho U^2)$
ΔP^*_{obl}	non-dimensional oblique pressure loss, $\Delta P_{\text{obl}}/(\frac{1}{2}\rho U^2)$
ΔP_{obl}	pressure loss due to oblique flow, Pa
δ	boundary layer thickness, m
ϵ	turbulent dissipation rate, m^2/s^3
η	conversion efficiency
γ	axial porous inertial resistance tensor coefficient
κ	Kármán's constant
μ	dynamic viscosity, kg/ms
μ_t	turbulent viscosity, kg/ms
ν	kinematic viscosity, m^2/s
ω	specific dissipation rate, $\sim \epsilon/k$
ϕ	arbitrary instantaneous flow field
ψ	monolith porosity
ρ	density, kg/m^3
σ	standard deviation of cycle inlet velocities, m/s
τ	shear stress, Pa
τ_{ij}	specific Reynolds stress tensor, m^2/s^2
ξ	non-uniformity index
ζ	mass flow weighted velocity over monolith face, m/s

Roman Symbols

C	Courant number, sum of ratios of time-step to characteristic convection time, $\Delta t \sum_{i=1}^{n} u_{x_i}/\Delta x_i$
$C_{\max}$	maximum Courant number for a convergent solution
D	cell density, cells/cm^2

D_h	nozzle hydraulic diameter, m
d_h	channel hydraulic diameter, m
F	friction factor, $2\tau/\rho\mathbf{u}^2$
f	frequency, Hz
F_{app}	apparent friction factor
$\mathbf{f_p}$	porous source term
g	gravity, m/s^2
J	ratio of pulse period to residence time in diffuser, $U_{\text{in}}/L_d f$
K	additional dimensionless pressure drop due to change of momentum
k	turbulent kinetic energy, m^2/s^2
k_c	mass transfer coefficient, m/s
L	length of monolith channel, m
l	length of computational monolith region, m
L_d	length of diffuser, m
$\dot{m}$	mass flow rate, kg/s
$\mathbf{P}$	porous resistance tensor
P	pressure, Pa
$\mathbf{P}_{\text{i}}$	porous inertial resistance tensor, kg/m^4
$\text{P}_{\text{i}x}$	axial component of porous inertial resistance tensor, kg/m^4
$\text{P}_{\text{i}y}$	transverse component of porous inertial resistance tensor, kg/m^4
$\mathbf{P}_{\text{v}}$	porous viscous resistance tensor, $\text{kg/m}^3\text{s}$
$\text{P}_{\text{v}x}$	axial component of porous viscous resistance tensor, $\text{kg/m}^3\text{s}$
$\text{P}_{\text{v}y}$	transverse component of porous viscous resistance tensor, $\text{kg/m}^3\text{s}$
Re_c	channel Reynolds number
S^*_{ij}	mean strain-rate tensor
$\mathbf{S}^v_i$	momentum source term
s_{ij}	strain-rate tensor

t	time, s
$\mathbf{u}$	superficial velocity, m/s
U	velocity magnitude, m/s
u	axial velocity component, m/s
u^+	dimensionless velocity, U/u_τ
u_τ	friction velocity, m/s
u_c	axial channel velocity
U_{in}	mean velocity at diffuser inlet, m/s
U_{mean}	cycle-averaged mean velocity at diffuser inlet, m/s
U_{out}	mean velocity downstream of monolith, m/s
u_s	superficial channel velocity, m/s
v	transverse velocity component, m/s
v_c	transverse velocity at α_c, m/s
W	outlet sleeve width, mm
$\mathbf{x}$	position vector, m
x^+	non-dimensional distance along the monolith, $x/d_h\text{Re}_c$
y	normal distance from surface, m
y^+	dimensionless distance from surface, $u_\tau y/\nu$

1 | Introduction

1.1 Motivation

The continued development of automotive exhaust catalyst systems is driven by increasingly stringent emissions regulations. The first emissions legislation was enacted in California in 1959 and the European Union first adopted directives for road vehicle emissions in 1970. Following the introduction of emissions standard Euro 1 in 1992, standards have been regularly revised to reduce the level of pollutant emissions and thereby lessen their harmful effects upon human health and the ecosystem. EU legislation focuses on four main pollutants: carbon monoxide (CO), nitrogen oxides (NO_X), hydrocarbons (HC) and particulate matter (PM).

Table 1.1: Euro emission standards for passenger cars (DieselNet, 2015)

Table 1.1 shows the progression of standards for passenger cars. All limits have decreased over the years to counteract increases in vehicle numbers, annual mileage and traffic density. Individual standards for HC and NO_X have been established and limitations of PM emissions for petrol engines

have been introduced in the past decade. More recent legislation includes a particle number (PN) emission limit in addition to the mass-based limits.

To comply with emissions standards, it is necessary to use a catalytic converter downstream of the engine to facilitate the conversion of pollutants in the pulsating exhaust flow into less harmful emissions. A two-way (oxidation) catalyst converts hydrocarbons and carbon monoxide into carbon dioxide and water. Originally employed in petrol engine exhausts, two-way converters are now typically used only in diesel engine exhausts due to the need for treatment of nitrous oxides. For petrol engine vehicles, the two-way catalyst was superseded by the three-way (oxidation-reduction) catalyst (TWC), benefiting from the additional reaction of the reduction of nitrous oxides to nitrogen and oxygen.

Figure 1.1: Schematic of a TWC

Figure 1.1 shows a typical TWC. The catalyst is a monolith structure in ceramic or metal. The monolith comprises many parallel channels with small hydraulic diameter. A thin washcoat applied to the channel walls provides a large surface area for the reaction of exhaust pollutants, as illustrated in Figure 1.2. Embedded in the washcoat are precious metals, such as platinum, rhodium and palladium, which increase the chemical reaction rate at lower temperature. The size and shape of monolith depends on vehicle size and packaging constraints, however a typical passenger vehicle monolith would have a circular or oval cross-section and a cell density between 15 and 95 cells/cm^2 (Pundir, 2007).

The catalyst does not function effectively before reaching operating temperature. From cold-start, the catalyst is initially heated by exhaust gases alone. Once reactions start to occur in the catalyst, their exothermic nature results in a 'snowballing' effect and therefore increased conversion efficiency. This warming-up process is known as *light-off*. Characteristic behaviour may then be expressed by the *light-off temperature* or *light-off time*, respectively denoting the temperature and time at which conversion efficiency passes a specified level. For 50% conversion, a TWC has a light-off temperature

Figure 1.2: Schematic of washcoated monolith

of 250–350°C (Kašpar et al., 2003). Light-off time is heavily dependent on the location of the catalyst. An under-body TWC has a light-off time of 90–120 s, however this drops to 10–20 s when the catalyst is closely coupled to the engine (Kašpar et al., 2003).

Petrol engines are generally internal combustion engines, where combustion is started through spark ignition. A key factor for the efficiency of emissions aftertreatment in spark ignition engine vehicles is the air-fuel ratio. Reduced fuel levels give a 'lean' air-fuel ratio, i.e. with high oxygen content. An insufficient level of reducing agents (e.g. CO, HC) leads to an oxidising combustion, resulting in increased O_2 and NO_X emissions and lower CO and HC (Taylor, 1984). Increased fuel levels lead to chemically reducing 'rich' combustion, i.e. with low oxygen content. This results in reduced NO_X emissions, but higher levels of CO and HC. Ideal combustion occurs at the point of *stoichiometry*, where exhaust gases consist only of nitrogen, water and carbon dioxide, with no residual oxygen or fuel. An emission control system is typically used to maintain the air-fuel ratio near stoichiometric level.

Ignition of engines using diesel oil is through compression of the charge and the air-fuel ratio is always lean, so the exhaust reaction is always oxidising. As with lean-burn spark ignition engines, the treatment of NO_X is thereby impeded, however the presence of PM complicates the issue further. A trade-off then exists in the combustion process of the two emissions, such that controlling the engine-out levels of both is problematic. The main device for the aftertreatment of PM is the Diesel Particulate Filter (DPF), where channels are alternately closed at either end of the catalyst and exhaust gases are filtered as they pass through the porous walls into neighbouring channels.

Ageing of the catalyst results in the degradation of its activity. Sintering at high temperatures

reduces the reactive surface area, whilst poisoning occurs from chemicals present in fuel and engine oil (Martin et al., 1998). When the catalyst is routinely subjected to non-uniform flow, the most utilised areas age faster, resulting in more rapid deterioration of efficiency.

Energy losses inside aftertreatment devices cause a pressure drop, resulting in an increased exhaust back-pressure which lowers engine efficiency. Back-pressure may be reduced by using a monolith of shorter length. For sufficient catalyst surface area for maximum conversion, it is therefore necessary for the cross-sectional area of the catalyst to be significantly larger than the inlet pipe. As a result, a large expansion is required between the exhaust pipe and the catalyst. Short wide-angled diffusers are typically used due to space constraints, thus increasing flow maldistribution in the catalyst (Clarkson, 1995).

Flow separates at the expansion, resulting in a confined jet that traverses the diffuser. Flow behaviour in the diffuser is illustrated in Figure 1.3(a). Close to the monolith face the flow decelerates and spreads radially, with part of the flow entering the monolith and the remaining flow feeding into vortices located between the jet and diffuser wall. As a result the flow entering the monolith is maldistributed, with higher velocities in the central channels of the monolith. Flow enters the channels axially on the centre line and obliquely at increased radial distance from the centre. Oblique flow at the monolith face results in separation at the channel entry and thus increased resistance in these areas, see Figure 1.3(b). Radial flow approaching the diffuser wall at the front face of the monolith stagnates. This causes an increase in pressure at these locations and some flow is obliged to enter the outermost channels of the monolith, resulting in secondary velocity peaks near the diffuser walls. A typical velocity profile across the monolith is shown in Figure 1.3(a).

Flow maldistribution in the monolith affects the pressure drop across the system as well as the conversion efficiency and degradation rate of the catalyst. The development of improved catalytic converter design concepts therefore requires an understanding of the effect of flow behaviour upon catalyst performance. Flow characteristics may either be studied empirically through experimental analysis, or predicted numerically using modelling techniques. Considering the extra cost, time and practical challenges associated with detailed flow measurements, computational fluid dynamics (CFD) provides an attractive alternative for studying flow behaviour and is therefore increasingly used to assess designs. CFD is commonly employed for this purpose, however the accuracy of predictions and the level of computational resources required for solution require assessment. This thesis addresses these issues through the development and analysis of several models.

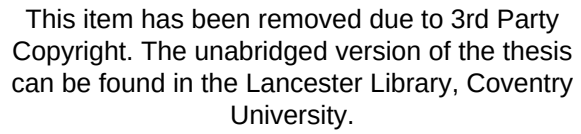

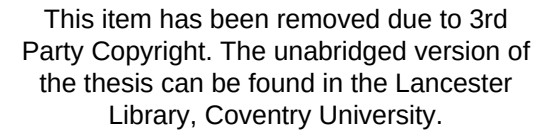

(a) Flow field in diffuser and typical velocity profile inside monolith

(b) Recirculation bubbles formed at channel walls

Figure 1.3: Example of flow behaviour in a catalytic converter system

1.2 Aims and Objectives

The overall aim of this thesis is to assess the performance of computational fluid dynamics as applied to catalytic converters systems using RANS-based turbulence modelling, and to develop novel methodologies for modelling catalyst monoliths for the improvement of CFD predictions, thus aiding the design process of the next generation of aftertreatment devices.

The specific objectives are to:

- Assess and validate the performance of existing CFD methodologies for modelling catalyst systems, combining state-of-the-art RANS turbulence models and various porous medium modelling approaches;
- Develop new computational methodologies aimed at improving on both the accuracy and efficiency of the porous medium model applied to the catalyst monolith;
- Evaluate the predictive capability of RANS-based simulations for transient flow through a simplified catalyst system geometry, in order to gain a better understanding of the fundamental flow features representative of typical engine operation conditions.

1.3 Thesis Outline

An overview of studies and literature relevant to this work is given in Chapter 2.

The methodology is then presented. The process of experimental data collection is detailed in Chapter 3 and the development of computational models is demonstrated in Chapter 4.

Chapter 5 presents results from the steady flow models and Chapter 6 presents pulsating flow results. Model predictions are compared to experimental measurements as axial velocity profiles downstream of the monolith and velocity fields in the diffuser.

The thesis is concluded in Chapter 7 by a summary of the principal findings and contributions presented in the work, with suggestions for future research.

2 | Literature Review

This chapter presents an overview of studies most relevant to this thesis. Significant works relating to flow maldistribution and pressure drop in the system are presented, and the previous application of CFD to modelling catalyst systems is summarised.

The exhaust gas flow is typically strongly pulsating, however pulsations in the flow complicate measurement in the system. For simplification, many studies have been undertaken with the assumption of steady or non-pulsating flow.

2.1 Flow distribution studies

For optimum conversion rates, the catalyst monolith is typically of a larger cross-sectional area than the connecting pipes. Inlet and outlet cones connect the monolith to the exhaust, however space constraints result in cones of relatively short length and wide angle. The sudden expansion results in a non-uniform flow profile upon entry into the catalyst, as observed by Wendland and Matthes, (1986).

Flow uniformity is a key factor in catalytic converter design since maldistributed flow adversely affects the performance of the catalyst. Flow profiles have been found to be more uniform with smaller Re (Benjamin et al., 1996; Lai et al., 1991) and higher monolith resistance (Clarkson, 1995; Lai et al., 1991).

The centre of the catalyst, observing higher velocities and temperatures, degrades at an increased rate, as found experimentally by Martin et al., (1998). In this regard, Howitt and Sekella, (1974) studied the effect of various flow deflection devices designed to inhibit flow to the monolith centre. It was found that improved uniformity of the flow carries with it an increased light-off time due to the reduction of gas flow concentration.

Will and Bennett, (1992) modelled the conversion in a catalytic converter and obtained a non-uniform predicted conversion profile at the monolith exit. Comfort, (1974) carried out a mathematical study on the effect of velocity distribution on conversion efficiency. Assuming reaction rates determined by mass transfer, a more uniform profile was found to improve efficiency. Experimental measurements by Martin et al., (1998) showed improved conversion rates of HC, CO and NO_X for increased uniformity, in particular for aged catalysts.

The velocity profile entering the catalyst is heavily dependent on the geometry of the diffuser connecting the exhaust to the catalyst body. Wollin, (2002) used diffusers with total included angle, denoting the overall diffuser expansion, of 60° and 180°. The total flow separation resulting from the 180° diffuser resulted in a less uniform profile than the 60° diffuser under pulsating flow conditions, however similar results were obtained for both diffusers under steady flow conditions. Hauber et al., (1998) studied the influence of inlet cone angle in a two-piece catalytic converter, where two monoliths are situated one after the other with a space between the two. It was observed that the inlet cone angle had a significant influence on the flow distribution in the first monolith, but negligible impact in the second monolith. Clarkson, (1995) studied the effect of total included diffuser angle and found that reducing the diffuser angle improved flow uniformity and decreased pressure drop across the system, however the size constraints of practical applications typically impede the use of low-angled diffusers.

Measurements are often taken downstream of the monolith in order to characterise flow in the monolith. However, the comparison of downstream profiles from numerical models and experimental data as a means of assessing monolith modelling techniques assumes an accurate description of flow behaviour in the diffuser upstream, e.g. Liu, (2003) and Weltens et al., (1993). The advance of non-intrusive optical measurement techniques has enabled the study of flow behaviour in the diffuser, e.g. Shuai et al., (2001), Turner et al., (2011), and Kim et al., (1995). Studies including measurements both upstream and downstream of the diffuser enable identification of areas of flow redistribution and provide further insight into the accuracy of CFD models.

Quadri et al., (2009b) used PIV to measure flow in the diffuser and were thus able to compare velocity profiles approximately 3 mm upstream with HWA profiles 30 mm downstream of the monolith. Significant differences in profile shape were observed (Figure 2.1). Since the flow cannot redistribute in the transverse direction inside the monolith, and only minimal mixing is expected downstream due to the uni-directional nature of the flow, the comparison demonstrates a dramatic redistribution of flow immediately before entering the monolith channels. Fluid is forced outwards directly in front of the monolith face, producing secondary peaks consistent with the study by Persoons et al., (2008).

PIV flow fields obtained by Quadri et al., (2009b) captured flow behaviour in a planar diffuser. A free shear layer separates the central jet from recirculating vortices on either side which occupy the rest of the diffuser. The potential core narrows as flow traverses the diffuser, whilst the recirculation regions feed into the jet. A saddle-shape velocity profile develops and is then suppressed as flow spreads at the monolith face. Velocities in the diffuser were found to be independent of Reynolds number, whilst a higher monolith resistance downstream was seen to flatten velocity profiles in the diffuser. Mat Yamin et al., (2013) measured steady state velocity profiles 2.5 mm from the monolith

Figure 2.1: Comparison of axial velocity profile shape upstream and downstream of monolith (Quadri et al., 2009b)

face and observed flatter profiles for lower Re.

Arias-García et al., (2001) compared steady and pulsating flows in a close-coupled catalyst and observed lower maldistribution for pulsating flow. Benjamin et al., (2002) compared different pulsating flow regimes, finding more uniform flow distribution at higher frequency, resulting in a reduced pressure drop across the system. The maldistribution for pulsating flows was found to be less sensitive to changes in Re than in the steady case. Benjamin et al., (2002) also introduced the non-dimensional parameter J, reciprocal of the Strouhal number, to characterise flows by the ratio of pulse period to residence time in the diffuser.

$$J = \frac{U_{\text{in}}}{L_d f} \tag{2.1}$$

where U_{in}, f and L_d respectively denote mean inlet pipe velocity, frequency and length of diffuser.

Flow maldistribution was found to reliably correlate with J (Benjamin et al., 2002). Liu et al., (2003) observed less uniform flow than Benjamin et al., (2002), although this was attributed to reduced inlet mean-peak ratio and the absence of periods of zero inlet velocity. Mat Yamin et al., (2013) measured flow in a similar system under pulsating conditions. Two flow regimes with similar J were seen to show similar flow fields. Lower J (lower Re and/or higher frequency) flows resulted in more uniform profiles within the monolith, since flow was able to reattach downstream of separation bubbles.

2.2 Monolith Pressure Drop

While flow distribution is linked to conversion efficiency and catalyst ageing, minimising the pressure drop is important for engine performance and fuel economy. Clarkson, (1995) found that a shorter inlet expansion and a longer monolith both decreased the pressure drop across the system. Wendland et al., (1991) found the pressure drop to increase with flow rate to a power between 1.1 and 1.5. However normalised pressure loss, calculated as the ratio of pressure loss to inlet pipe dynamic head, was found to decrease with flow rate. By normalising the pressure drop, the relationship between Reynolds number and pressure loss was found to be the same for hot flow, cold flow and exhaust flow (Wendland et al., 1991).

Pressure losses in the system may be estimated by theoretical formulations. Principal losses result from the developing boundary layer at channel walls.

Shah, (1978) developed the following expression for non-dimensional pressure drop ΔP^* along a channel:

$$\begin{aligned} \Delta P^* &= (F\mathrm{Re}_c)(4x^+) + K(x) \\ &= (F_{\mathrm{app}}\mathrm{Re}_c)(4x^+) \end{aligned} \tag{2.2}$$

where

$$\Delta P^* = \frac{\Delta P}{\frac{1}{2}\rho U^2} \tag{2.3}$$

denotes the non-dimensional pressure drop,

$$x^+ = \frac{L}{d_h Re_c} \tag{2.4}$$

denotes the non-dimensional distance along the monolith, and

$$F_{\mathrm{app}}\mathrm{Re}_c = \frac{3.44}{\sqrt{x^+}} + \frac{(F\mathrm{Re}_c) + \frac{K(\infty)}{4x^+} - \frac{3.44}{\sqrt{x^+}}}{1 + C(x^+)^{-2}} \tag{2.5}$$

denotes the apparent friction factor based on the total pressure drop from $x = 0$ to L. $K(x)$ is an additional dimensionless pressure drop due to change of momentum. $K(0) = 0$ at the duct inlet and increases monotonically to a constant value $K(\infty)$ in fully-developed flow. For laminar flow in square channels, $K(\infty) = 1.43$, $FRe_c = 14.227$ and $C = 0.000212$ (Shah and London, 1978). For fully-developed channel flow, Eq. 2.2 reduces to the Hagen-Poiseuille (H-P) relationship:

$$\Delta P^* = (F\mathrm{Re}_c)(4x^+) \tag{2.6}$$

Will and Bennett, (1992) compared the theoretical H-P pressure drop with measurements from a catalyst monolith and found good agreement. Benjamin et al., (1996) measured the pressure drop

across both washcoated and unwashcoated monoliths and compared the results with the theoretical formulations given by Eqs 2.2 and 2.6. The expression for fully-developed flow (Eq. 2.6) was found to agree well with experimental data for $x^+ > 0.2$. For lower x^+, losses due to developing flow were non-negligible and measurements in this region better matched the Shah equation (Eq. 2.2).

CFD simulations were performed for a catalyst system, using Eqs 2.2 and 2.6 to calculate the pressure drop across the 'porous' monolith (Benjamin et al., 1996; Haimad, 1997). CFD predictions were very similar for the two models, with the Shah equation resulting in a slightly more uniform velocity profile downstream of the monolith. This was attributed to increased back pressure associated with boundary layer development (Haimad, 1997). In comparison with an experimentally measured velocity profile, maldistribution of the flow downstream was found to be underpredicted by the models. Velocities at locations corresponding to areas of highly oblique flow at the monolith face were noticeably overpredicted. It was concluded that the model over-simplified the system, with pressure losses only associated with one-dimensional flow.

In reality, flow approaching a series of parallel plates obliquely will result in separation at the surface and a redistribution of the flow in the channel. Figure 1.3(b) shows flow approaching parallel channels at an angle α, with axial velocity u, transverse velocity v and velocity magnitude U. Due to the high angle of attack, recirculation bubbles form at the wall of each monolith cell as flow enters the channels, which results in increased pressure loss in the channel.

During their work on heat exchangers, Küchemann and Weber, (1953) developed an expression for pressure loss due to oblique flow, given by

$$\Delta P_{\text{obl}} = \frac{\rho v^2}{2} \tag{2.7}$$

The inclusion of this additional pressure loss term in a computational model was found by Benjamin et al., (2001) to improve velocity predictions downstream of the monolith, with increased maldistribution and higher velocity maxima.

Expressing a non-dimensional oblique pressure loss by $\Delta P^*_{\text{obl}} = (\Delta P_{\text{obl}})/(\frac{1}{2}\rho U^2)$, Eq. 2.7 is equivalent to

$$\Delta P^*_{\text{obl}} = \sin^2 \alpha \tag{2.8}$$

Persoons et al., (2008) measured pressure losses due to oblique flow for annular swirling flow entering a catalyst. For angle of attack $\alpha \leq 33^\circ$, they found that the pressure loss could be approximately expressed by

$$\Delta P^*_{\text{obl}} = 0.459 \sin^2 \alpha \tag{2.9}$$

Expressing oblique pressure loss measurements as a function of Reynolds number and angle of incidence, Quadri et al., (2009a) derived the piecewise relationship for the range of angles studied:

$$\Delta P^*_{\text{obl}} = \begin{cases} 0.021\ \text{Re}^{0.5} \sin^2 \alpha & 30^\circ \leq \alpha \leq 45^\circ \\ 0.18\ \text{Re}^{0.24} \sin^2 \alpha & 55^\circ \leq \alpha \leq 70^\circ \\ 0.525\ \text{Re}^{0.1} \sin^2 \alpha & \alpha = 75^\circ \end{cases} \tag{2.10}$$

Quadri et al., (2009a) combined Eqs 2.6 and 2.10 to model pressure drop in the monolith and found good agreement downstream, with some overprediction of maldistribution near to the wall, as had been observed by Benjamin et al., (2001) using Eq. 2.7.

The overprediction of pressure losses at regions of oblique flow suggests that the relationship between angle of attack and pressure loss changes past a certain angle, i.e. a *critical angle*. Since channel height restricts the size of the recirculation bubble, it follows that entry pressure losses should remain constant above a certain angle of attack. Eq. 2.7 would then become

$$\Delta P^*_{\text{obl}} = \begin{cases} \sin^2 \alpha & \alpha < \alpha_c \\ \sin^2 \alpha_c & \alpha \geq \alpha_c \end{cases} \tag{2.11}$$

where α_c denotes the *critical angle*.

Küchemann and Weber, (1953) also presented a critical angle effect using the Betz assumption that there is no overall increase in pressure and thus oblique entry losses may not exceed the subsequent pressure drop within the channel. The angle α_c is then dependent on the flow rate, and may be denoted $\alpha_{c,v}$. Using the Hagen-Poiseuille formulation given in Eq. 2.6, the critical angle may be derived,

$$\alpha_{c,v} = \tan^{-1} \sqrt{\frac{(4F\text{Re}_c)\mu L}{\rho \psi d_h^2} \frac{u_s}{u^2}} \tag{2.12}$$

Liu, (2003) modelled the total pressure drop across the monolith using Eq. 2.6 and Eq. 2.11 with $\alpha_c = \alpha_{c,v}$. Comparing predictions with and without a critical angle approach, the inclusion of a critical angle was found to significantly improve the accuracy of the downstream velocity profile. Minima were in better agreement, however velocities at the wall were still overpredicted.

Quadri, (2008) also assumed fully-developed laminar flow in the channels and compared various fixed critical angles α_c using

$$\Delta P^*_{\text{obl}} = \text{A}(\text{Re}_c)^{\text{B}} \left(\frac{L}{d_h}\right)^{\text{C}} (\sin^2 \alpha_c)^{\text{D}} \tag{2.13}$$

where the coefficients A=0.447, B=0.1233, C=0.0756 and D=0.1287 were derived from experimental measurements (Quadri, 2008). It was found that $\alpha_c = 81^\circ$ best agreed with experimental data.

Velocity profiles were found to be quite sensitive to the choice of α_c. Maximum velocities were overpredicted using $\alpha_c = 85°$, but limited with $\alpha_c = 75°$. Reduction of the critical angle value resulted in limited pressure loss at regions of highly oblique flow corresponding to troughs in the downstream velocity profile. Velocity minima were therefore increased and the conservation of mass resulted in lower velocity maxima predictions at the centre and at the walls, giving a more uniform profile.

It is worth noting that accurate CFD predictions immediately upstream of the monolith have not been obtained and that the inclusion of entrance effects for the improvement of predictions may therefore only compensate for modelling inadequacies in the diffuser.

2.3 CFD Studies in Automotive Catalysts

Approaches to Modelling the Catalyst

For simplicity and economy of computation, the large majority of CFD studies in catalyst systems consider steady state cases. Several transient CFD simulations have been used for prediction of flow behaviour but results have not been validated against experimental data (e.g. Kim et al., 1993; Benjamin and Roberts, 2000; Jeong and Kim, 1997; Arias-García et al., 2001).

Initial CFD studies of pulsating pipe flow have been compared with experimental measurements of heat transfer coefficient (Al-Haddad and Al-Binally, 1989) and instantaneous velocity profiles (Cho and Hyun, 1990).

Full 3D models of a close-coupled catalyst (CCC) system have been developed by Park et al., (1998) for comparison with a limited range of LDV measurements, and by Bressler et al., (1996) for comparison of cross-sectional partial volume flow contours, however the comparisons presented in these studies are limited by their qualitative nature.

Liu et al., (2003) quantitatively analysed pulsating flow predictions in an axisymmetric system. A 5° wedge section of the system was modelled and both instantaneous and cycle-averaged velocity profiles downstream of the monolith were compared with HWA measurements. Predictions were found to agree fairly well with experiment for gently pulsating flow, however agreement deteriorated for more severely pulsating conditions. It was suggested that the turbulence model was inappropriate for such conditions. A more complex model using LES was employed by García-Villalba et al., (2006) but without experimental comparison.

Resolving the entire fluid domain over the intricate geometry of the monolith channels carries very

high computational demand. An alternative approach is to regard the overall pressure drop across the monolith. This is commonly achieved by modelling the monolith as an equivalent continuum (e.g. Jeong and Kim, 1997; Lai et al., 1991), or even as an infinitesimally thin interface (Ozhan et al., 2014). Via theoretical or empirical formulations, the pressure drop of the substrate may then be applied directly to the model.

The solution of flow in a small number of channels may provide information on flow behaviour in the monolith channels, whilst limiting the computational cost incurred. Single channel studies have been carried out for quantification of oblique pressure losses (Haimad, 1997) and heat transfer studies (Benjamin and Roberts, 2000; Day et al., 1999). Haimad, (1997) conducted an individual channels study in order to assess the limitations of the porous media approach. Six channels were modelled as parallel plates with two-dimensional flow. Comparing the predicted pressure drop of a porous medium model for the same system, it was found that the channels model predicted a pressure drop approximately 8% greater.

Background to Turbulence Modelling

Typical Reynolds numbers in the engine exhaust fall between 10^3– 5×10^4 (Kandylas and Stamatelos, 1999). Flow in the diffuser is turbulent, however flow inside the monolith is laminar due to the small hydraulic diameter of the channels. Since the behaviour of flow in the diffuser significantly affects the flow profile entering the monolith, it is necessary to accurately predict the level of turbulence exhibited.

Turbulent motion occurs once the inertia of the fluid overcomes its viscous stresses and the previously laminar motion of the fluid becomes unstable. Indeed, analysis of the Navier-Stokes equations (Eq. 4.2) shows linearity of all terms except the inertial term. Laminar flow is regular in nature and is so-called because it was believed to move in smooth layers, or laminae. Disturbances affecting the flow may decay over time, allowing the flow to remain stable. If disturbances do not decay, the behaviour of fluid particles destabilises and fluctuations increase.

Turbulence may be characterised by irregularity, diffusion, non-linearity and highly fluctuating vorticity (Garde, 2010) and is composed of an eddying motion, i.e. local swirling flow with high vorticity. An eddy is a group of particles that moves laterally and longitudinally. Turbulent eddies are three-dimensional, even in two-dimensional flow. Eddies are generated in regions of high shear and varying sizes are present, with large-scale eddies carrying the smaller disturbances along the flow. With the decay of turbulence, the kinetic energy transfers from the larger eddies to smaller ones and

then, via molecular viscosity, they dissipate into heat. This is known as *Kolmogov's equilibrium theory.*

Modelling the turbulence of a given system is challenging since no turbulence model has yet been established to be valid for all flows. Wilcox, (2006) states that 'an ideal model should introduce the minimum amount of complexity while capturing the essence of the relevant physics'. Many approaches exist to model turbulence, however they may largely be classified as belonging to one of three groups: Reynolds-averaged Navier-Stokes (RANS), Large Eddy Simulation (LES) or Direct Numerical Simulation (DNS).

RANS models treat the irregularity of turbulent flow statistically. Each instantaneous flow field ϕ may be expressed as the sum of a mean $\overline{\phi}$ and a fluctuating part $\phi^{'}$, so that

$$\phi(\mathbf{x},t) = \overline{\phi}(\mathbf{x}) + \phi^{'}(\mathbf{x},t) \tag{2.14}$$

When the statistical flow parameters of the flow do not vary over time, the turbulent flow field is called *stationary* or *quasi-steady.* The time averaged mean $\overline{\phi}$ may then be defined

$$\overline{\phi} = \lim_{t^* \to \infty} \frac{1}{t^*} \int_t^{t+t^*} \phi \, \mathrm{d}t \tag{2.15}$$

and the time average of turbulent fluctuations is zero:

$$\overline{\phi^{'}} = \lim_{t^* \to \infty} \frac{1}{t^*} \int_t^{t+t^*} \phi^{'} \, \mathrm{d}t = 0 \tag{2.16}$$

Decomposition of all flow variables in the Navier-Stokes equations (Eq. 4.2) forms the Reynolds-averaged Navier-Stokes (RANS) equations:

$$\rho \frac{\partial u_i}{\partial t} + \rho u_j \frac{\partial u_i}{\partial x_j} = -\frac{\partial p}{\partial x_i} + \frac{\partial}{\partial x_j} \left(2\mu s_{ij} + \rho \tau_{ij} \right) \tag{2.17}$$

where s_{ij} is the strain-rate tensor given by

$$s_{ij} = \frac{1}{2} \left(\frac{\partial u_i}{\partial x_j} + \frac{\partial x_j}{\partial u_i} \right) \tag{2.18}$$

and $\tau_{ij} = -\overline{u_j^{'} u_i^{'}}$ denotes the specific Reynolds stress tensor, given by

$$\tau_{ij} = - \begin{bmatrix} \overline{u_i u_i} & \overline{u_i u_j} & \overline{u_i u_k} \\ \overline{u_j u_i} & \overline{u_j u_j} & \overline{u_j u_k} \\ \overline{u_k u_i} & \overline{u_k u_j} & \overline{u_k u_k} \end{bmatrix} \tag{2.19}$$

τ_{ij} describes the stress acting on the control volume. It is symmetric and therefore has six independent components. The diagonal and non-diagonal elements respectively represent the three normal stress components and three shear stress components. These, along with the unknown mean-flow

properties of the pressure and velocity components, result in ten unknown values. Mass conservation (Eq. 4.1) and the three components of Eq. 2.17 collectively make four equations in ten unknowns and thus the system is not closed. Closure of the system is achieved by modelling τ_{ij} in terms of the mean flow quantities. Turbulence models may be classified by the number of additional equations involved in order to close the system.

The Boussinesq eddy-viscosity approximation forms the basis of most RANS turbulence models. It assumes proportionality of the Reynolds stress tensor to the product of the eddy viscosity μ_t and the mean strain-rate tensor S^*_{ij}, such that

$$\tau_{ij} = 2\mu_t S^*_{ij} - \frac{2}{3}\rho k \delta_{ij} \tag{2.20}$$

Algebraic turbulence models are the simplest models. Using the Boussinesq approximation (Eq. 2.20), the eddy viscosity is calculated from the mixing length. Both properties being dependent on the flow, an algebraic relation between the two must be specified and thus the model is by definition incomplete.

Eddy viscosity models use the turbulent viscosity μ_t to model τ_{ij}. They include the two-equation k-ϵ and k-ω models. In a k-ϵ model, transport equations are solved for the turbulent kinetic energy k and the turbulent dissipation rate ϵ. k-ω models solve for k and for the specific dissipation rate ω, where $\omega \sim \epsilon/k$. Eddy viscosity models also include Spalart-Allmaras models, where a single transport equation is solved to determine μ_t. The k-ϵ model assumes a velocity scale of k, however in the near-wall region v^2 is more appropriate (Durbin, 1991). In addition to solving for k and ϵ, the v^2f turbulence model also solves the normal stress function and the elliptic function f. Reynold stress transport models solve transport equations for all components of τ_{ij}. They are therefore complex and incur high computational demand.

Large eddy simulations make a distinction between eddies of different size. Large eddies are computed since they are directly affected by boundary conditions and carry the majority of Reynolds stresses. The smallest eddies, so called subgrid-scale (SGS), are modelled since the small-scale turbulence here is less critical. The turbulent SGS stress tensor is modelled using the Boussinesq approximation. El-Behery and Hamed, (2011) compared various two-equation RANS models for flow in an asymmetric diffuser and found best agreement with experimental and LES results using the v^2f model. Young and Ooi, (2007) compared LES and three-dimensional Unsteady RANS (URANS) to two-dimensional URANS for flow around a cylinder. Using three-dimensional URANS gave only slight improvement, whilst LES significantly improved predictions of wake structure and behaviour. Catalano et al., (2003) also considered flow around a cylinder, observing LES to be in excellent agreement

with experimental data for mean pressure distribution. URANS provided satisfactory predictions but RANS results were relatively poor.

Direct numerical simulations produce a complete three-dimensional time-dependent solution of the Navier-Stokes and continuity equations. They represent numerically accurate solutions of exact equations of motion, i.e. no turbulence closure approximation is used, and thus carry high computational demand. Cokljat et al., (2003) compared various RANS models with DNS results for recirculating flows. The v^2f model was found to be comparable to the most accurate two-equation models and in some cases improved accuracy. Ozhan et al., (2014) conducted DNS for a catalytic converter system, using adaptive mesh refinement to economise on computational resources.

Although most of the boundary layer is turbulent like the freestream flow, there exists a very thin layer adjacent to the surface where fluctuations are negligible. Viscous effects become more important close to the wall and the velocity profile varies logarithmically with distance from the surface. This is known as the *law of the wall* and is given by

$$\frac{U}{u_\tau} = \frac{1}{\kappa} \ln \frac{u_\tau y}{\nu} + C \tag{2.21}$$

where κ is Kármán's constant (≈ 0.41) and C is a dimensionless constant of integration. Expressing Eq. 2.21 in terms of the dimensionless velocity $u^+ \equiv \frac{U}{u_\tau}$ and distance $y^+ \equiv \frac{u_\tau y}{\nu}$, we may write

$$u^+ = \frac{1}{\kappa} \ln y^+ + C \tag{2.22}$$

Turbulence models do not inherently account for changes in flow behaviour at a surface and thus require the inclusion of a wall treatment to resolve the boundary layer. The all-y^+ treatment available in STAR-CCM+ assumes that the viscous sublayer is resolved for fine meshes and, for coarse meshes, assumes that the near-wall cell lies within the log layer and derives shear stress, turbulent production and turbulent dissipation from equilibrium turbulent boundary layer theory (CD-adapco, 2013).

In a catalytic converter system the dominant flow characteristics are the separation in the diffuser and the resultant vortices. Algebraic models are too simplistic for such a case (Durbin, 1995), however the standard k-ϵ model is not valid at the wall where viscous effects dominate over turbulent effects (Rodi and Scheuerer, 1986). To account for this, various wall functions have been developed such that near-wall flow behaviour is embodied in the equations. Clarkson, (1995) compared the standard k-ϵ and renormalisation group (RNG) k-ϵ models with wall functions and with the Norris-Reynolds one equation near-wall model for flow in a catalyst system. For both models, the one equation model at the wall significantly improved velocity and pressure predictions compared to wall functions.

2.4 Summary

The behaviour of flow in catalytic converters has been widely studied since their introduction and is a continued field of international research. Technological developments have extended both experimental and modelling capabilities. Flow measurements are increasingly accurate and are possible in previously inaccessible regions of the system, whilst sophisticated numerical models benefit from the extensive computational resources offered by high performance computing.

DNS and LES provide improved accuracy of predictions compared to RANS-based modelling, however the computational cost incurred still hinders widespread use and RANS remains the common approach for current industrial practices. Many turbulence models have been developed for RANS modelling, and the v^2f model has been found to improve the accuracy of turbulent boundary layer prediction compared to other models.

Flow maldistribution and pressure drop are the characteristics of principal interest in catalyst design. Studies of flow uniformity in a catalyst system have revealed an association with the upstream flow behaviour and a strong dependence on the geometry of the system. Efforts to successfully predict the downstream profile, characteristic of flow in the catalyst, have failed to provide accurate agreement of flow maldistribution. Discrepancies have largely been attributed to inaccuracies of pressure loss predictions in the monolith channels, in particular at the channel entrance where flow enters obliquely.

Pressure losses associated with the monolith have been studied and theoretical formulations, incorporated into a porous domain, have been found to provide moderate agreement but be insufficient without the consideration of additional entry losses. Measurements of oblique entry pressure losses have yielded various expressions dependent on the angle of attack. Incorporation of an entrance effect improves CFD predictions, however some disagreement still remains.

A limited amount of single channel studies have been conducted, therefore an overall prediction and analysis of flow behaviour within the channels has not yet been realised. Comparison between CFD and experimental studies is very limited for pulsating flow, and no validation has been presented for prediction of flow in the upstream diffuser region. The purpose of the work contained in this thesis is to expand on previous CFD studies, developing accurate modelling techniques and contributing to a more comprehensive understanding of catalytic converter flow behaviour.

3 | Experimental Data Collection

All experimental data presented in this work has been collected in the flow laboratory at Coventry University. The measurements were taken as part of this work and also by Mat Yamin, (2012), and are detailed in Section 3.4.

3.1 Flow Rig

3.1.1 Monolith Pressure Drop

Pressure loss across the monoliths was measured on the rig shown schematically in Figure 3.1. Air is supplied via a calibrated viscous flow meter (1) to a plenum (2) with flow straightener (3) and axisymmetric contracting nozzle (4). Four equidistant pressure taps (5) are located around the nozzle and the plenum attaches to the front face of the monolith (6). Pressure drop measurements are carried out using a 20 channel water manometer.

The pressure drop is calculated by

$$\Delta P = \rho g \overline{\Delta h} \tag{3.1}$$

where $\overline{\Delta h}$ is the mean change in water elevation $\Delta h_i = h_i - h_a$ from the four channels, i =1–4, and h_a is the water elevation at ambient pressure.

Figure 3.1: Schematic diagram of 2D isothermal flow rig used for pressure drop measurements

3.1.2 Catalytic Converter System

Figure 3.2 shows a schematic diagram of the isothermal flow rig used for flow measurements. The high pressure line supplies air through a viscous flow meter into the flow rig (1) where a plenum (2)

with flow straightener (3) and axisymmetric nozzle (4) leads to a pulse generator (5). Air then flows through another flow straightener (6) and past a resonator box (7), installed to shape pulses during pulsating flow studies. A particle generator (9) supplies seeding to a second plenum (8) with flow straightener (10) to minimise any swirl components. A two-dimensional nozzle (11) provides uniform flow to the planar diffuser (12), thus generating well-defined inlet conditions for CFD. The nozzle has outlet dimensions 24 × 96 mm, giving a hydraulic diameter of D_h=38.4 mm, or 0.0384 m.

Figure 3.2: Schematic diagram of 2D isothermal flow rig

The diffuser (12), shown in Figure 3.3, is made of crown glass for optimal optical conditions for PIV. It has inlet dimensions 24 × 96 mm, outlet dimensions 78× 96 mm, length 48 mm and a total included angle of approximately 60°.

The diffuser outlet attaches to an unwashcoated monolith (13) of length 27 mm or 100 mm. The monoliths are made of cordierite ($2\,MgO \cdot 2\,Al_2O_3 \cdot 5\,SiO_2$), a low-thermal-expansion ceramic (Pundir, 2007), and have channel hydraulic diameter 1.12 mm, a nominal cell density of 62 cells/cm^2 and porosity 0.77.

An outlet sleeve (14) of length 50 mm minimised any influence from air outside the rig. Two sleeves were used: a fitted sleeve of dimensions 78 × 96 mm and a wide sleeve of outlet dimensions 125 × 96 mm.

Figure 3.3: Schematic diagram of planar diffuser

3.2 Measurement

Flow within the diffuser was measured using particle image velocimetry (PIV) and axial velocity profiles at the nozzle exit and downstream of the monolith were obtained using hot-wire anemometry (HWA).

3.2.1 Particle Image Velocimetry

Measurements in the diffuser were obtained using PIV, a non-intrusive optical imaging technique which measures the velocity at thousands of points in a flow field. As the fluid passes through the measurement plane, seeded particles are intermittently illuminated by a laser sheet and are captured on a CCD camera. Each image is divided into a grid of small interrogation regions where, using the timing and sequence of the acquisition of image pairs, particle velocities are obtained.

A six-jet atomiser at 25 psi produced olive oil droplets of approximately 0.6 μm diameter. A cylindrical lens of -25 mm focal length was combined with a spherical lens of 500 mm to transform the circular beam from a 120 mJ solid-state Nd:YAG laser into an approximately 1 mm thick light sheet at a stand-off distance of 0.5 m to illuminate the seeded flow. A 4-megapixel CCD camera with resolution of 2048 $\times$ 2048 pixel was used to capture the flow field. The camera was coupled with a 105 mm lens and was placed 0.8 m from the measurement plane to cover an 80 $\times$ 60 mm field of view, resulting in a magnification factor of 0.155. An f number of 11 enabled a particle image diameter

above 2 pixels, avoiding pixel locking. INSIGHT-3G software was used for image processing. The recursive Nyquist method with a 64 × 64 initial grid and a final grid of 32 × 32 pixels yielded 95% valid vectors in each field and a vector resolution of 0.76 mm.

The majority of the flow field was captured with a sampling size of 2048 points, however some data loss occurred at the sealed joints of the diffuser inlet and outlet. The measurement closest to the monolith face is at a distance 2.5 mm upstream. An example of the range of valid data points is given in Figure 3.4.

Figure 3.4: Example of collected data set

3.2.2 Hot wire Anemometry

Axial velocity profiles at the nozzle exit and downstream of the monolith were obtained using HWA, an intrusive fluid measurement method. The anemometer uses the priniciple of convective theory to measure the velocity of a fluid. As air passes over the probe, the wire is maintained at a constant temperature through adjustment of the voltage. The current required is used to calculate the heat lost due to fluid convection, and thus the velocity of the flow.

The system used was a TSI IFA 300 constant temperature HWA system, pictured in Figure 3.5(a), with 5 μm platinum-plated tungsten wires (Dantec 55P11), shown in Figure 3.5(b), calibrated on an automatic TSI 1129 calibration rig. A 1 MHz 4 channel 12 bit A/D converter converted the IFA output voltage ($\pm$5 V) to a digital signal to be processed by ThermalPro software.

(a) HWA system (TSI Incorporated, 2010)

(b) 5 μm tungsten wire (Dantec Dynamics, 2014)

Figure 3.5: Schematic of HWA system

The majority of the velocity profile is captured, however the width of the probe affects the closest possible measurement to a surface.

3.3 Flow Regimes

Mat Yamin, (2012) measured steady state axial velocity profiles with HWA at the nozzle exit and 40 mm downstream of the 27 mm monolith across both planes for a range of Reynolds numbers. Acceptable uniformity of the upstream profiles, presented in Figure 3.6, and approximate symmetry and limited variation across the z-plane of the downstream profiles, presented in Figure 3.7, led to the presumption of symmetrical two-dimensional flow in the system. This is confirmed by PIV flow fields in the diffuser, presented in Figure 3.8 for steady and pulsating flows.

Figure 3.6: HWA velocity profiles at centre of nozzle exit (Mat Yamin, 2012)

(a) $\mathrm{Re} = 2.2 \times 10^4$ (b) $\mathrm{Re} = 4.2 \times 10^4$

Figure 3.7: HWA velocity profiles 40 mm downstream of 27 mm monolith (Mat Yamin, 2012)

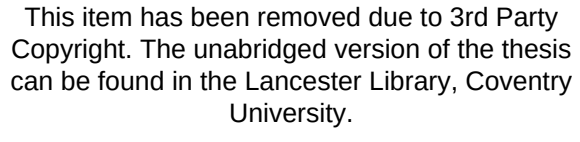

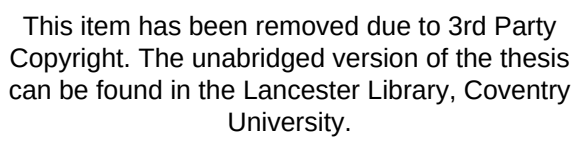

(a) Steady flow
$L = 27$ mm, Re $= 4.3 \times 10^4$

(b) Pulsating flow
$L = 27$ mm, Re $= 4.2 \times 10^4$, $f = 50$ Hz at $t/T = 0.5$

Figure 3.8: Symmetry of velocity vectors in diffuser (Mat Yamin et al., 2013)

3.3.1 Steady Flow

Steady state measurements were taken for systems with monoliths of length 27 mm and 100 mm, at Reynolds numbers of 2.2×10^4, 3.0×10^4, 4.2×10^4 and 6.0×10^4. Re is defined by the mean velocity at the diffuser inlet U_{in}, obtained from HWA profiles, and the hydraulic diameter of the nozzle.

3.3.2 Pulsating Flow

Pulsating flow Reynolds numbers are defined by the cycle-averaged mean velocity at the diffuser inlet U_{mean}, obtained from HWA profiles, and the hydraulic diameter of the nozzle D_h. Pulsation frequencies of 50 Hz and 100 Hz represent exhaust pulses of a 4 cylinder engine at 1500 and 3000 RPM respectively (Mat Yamin, 2012).

Pulsating flow measurements were taken over 100 cycles. The data presented for comparison is the phase-average at each timestep. The pulse shapes are approximately sinusoidal, as shown in Figure 3.9.

Figure 3.9: Inlet pulse shapes at centre of nozzle exit (Mat Yamin, 2012). Time t is normalised by the pulse period T.

3.4 Summary

Tables 3.1 and 3.2 present the experimental data used for analysis of CFD predictions in this thesis. The superscript '*' denotes measurements collected by Mat Yamin, (2012).

Table 3.1: Steady flow test case parameters

Table 3.2: Pulsating flow test case parameters

4 | CFD Methodology

The velocity and pressure of the air flow are described by the conservation of mass, Newton's Second Law, and the conservation of energy. By applying these physical principles to a given control mass, the following equations are obtained.

Continuity

$$\frac{\partial \rho}{\partial t} + \nabla(\rho \mathbf{u}) = 0 \tag{4.1}$$

Navier-Stokes

$$\rho \left[\frac{\partial \mathbf{u}}{\partial t} + (\mathbf{u} \cdot \nabla)\mathbf{u} \right] = -\nabla P + \mu \nabla^2 \mathbf{u} \tag{4.2}$$

These are known as the *governing equations*. The Navier-Stokes equations include a transient term $\partial \mathbf{u}/\partial t$, convective flux $(\mathbf{u} \cdot \nabla)\mathbf{u}$, diffusive flux $\mu \nabla^2 \mathbf{u}$ and pressure gradient ∇P. Since an analytical solution for the Navier-Stokes equations has not yet been established, computational fluid dynamics is used to obtain a numerical solution to the governing equations.

Assumptions in the models, made for practical calculation or justified by experimental measurement (Figures 3.6–3.8), are:

- isothermal air flow
- Newtonian fluid
- uniform inlet flow
- planar flow - 2D flow or periodic in z-direction
- symmetry with respect to $y = 0$

4.1 Discretisation

STAR-CCM+ uses a finite volume method for the discretisation of Eqs 4.1–4.2. The solution domain is divided into control volumes and the integral form of the conservation equations is applied to each volume. The computational node is at the centre of each control volume and boundaries are defined by the grid imposed on the domain. The net flux across the boundary is the sum of integrals over the faces of the control volume. Figure 4.1 shows the flux of the arbitrary flow variable ϕ over a control volume.

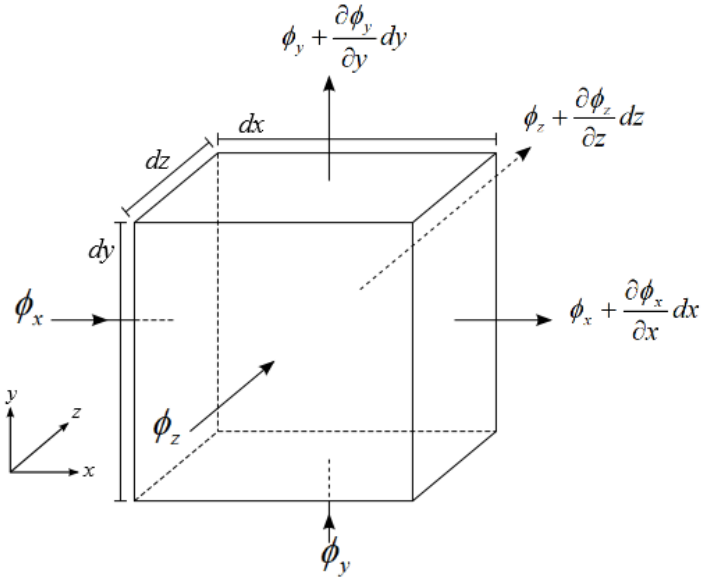

Figure 4.1: Flux balance over a control volume

Discretisation of the convective term in Eq. 4.2 requires an approximation of the first derivative. An upwind differencing scheme computes the convective flux at a face using information from the upstream CV. The second order upwind scheme computes the convective flux as:

$$(\dot{m}\phi)_f = \dot{m}_f \phi_f = \begin{cases} \dot{m}_f \phi_{f,0} & \text{for } \dot{m}_f \geq 0 \\ \dot{m}_f \phi_{f,1} & \text{for } \dot{m}_f < 0 \end{cases} \tag{4.3}$$

where $\dot{m}_f$ and ϕ_f respectively denote mass flow rates and scalar values at the face f. The values $\phi_{f,0}$ and $\phi_{f,1}$ are linearly interpolated from cell values either side of the face via

$$\begin{aligned} \phi_{f,0} &= \phi_0 + (\mathbf{x}_f - \mathbf{x}_0) \cdot (\nabla\phi)_{r,0} \\ \phi_{f,1} &= \phi_1 + (\mathbf{x}_f - \mathbf{x}_1) \cdot (\nabla\phi)_{r,1} \end{aligned} \tag{4.4}$$

where $\mathbf{x}_0$, $\mathbf{x}_1$ are the cell centroids, $\mathbf{x}_f$ is the position of the boundary face f and $(\nabla\phi)_{r,0}$, $(\nabla\phi)_{r,1}$ denote the limited reconstruction gradients in each cell (CD-adapco, 2013).

The transient term is only included for the pulsating flow model. The first-order (Euler implicit) scheme discretises the unsteady term using the solutions at the current time-step t and at the previous time-step $t-1$, such that

$$\left(\frac{d\phi}{dt}\right)_t = \frac{\phi_t - \phi_{t-1}}{\Delta t} \tag{4.5}$$

4.2 Solution Algorithm

Two flow solvers are available in STAR-CCM+, *coupled* and *segregated*. When applying the coupled flow solver, conservation equations for mass and momentum are solved simultaneously using a time-marching approach. For the steady flow case, a pseudo-transient term is used instead of the physical time derivative. As the solution advances in pseudo-time, this term is driven to zero and the governing equations reach a steady state. The segregated flow model solves the flow equations for velocity and pressure separately. The SIMPLE (Semi-Implicit Method for Pressure Linked Equations) algorithm is used to calculate the flow field. By expressing the pressure p at a point as the sum of the estimated value p^* and its correction p', and defining the velocity components likewise, an iterative procedure is performed using the discretised momentum and continuity equations for the solution of a given flow field. The algorithm is summarised in Figure 4.2, where the superscripts '$*$' and '$'$' denote the intermediate value and correction term respectively and ϕ represents an arbitrary flow variable.

A coupled flow model is best for compressible flows, whereas a segregated flow model requires less computational resources and is thus an ideal alternative for incompressible or mildly compressible flow (CD-adapco, 2013). All studies presented in this work assume air as an incompressible Newtonian fluid and thus use the segregated flow solver.

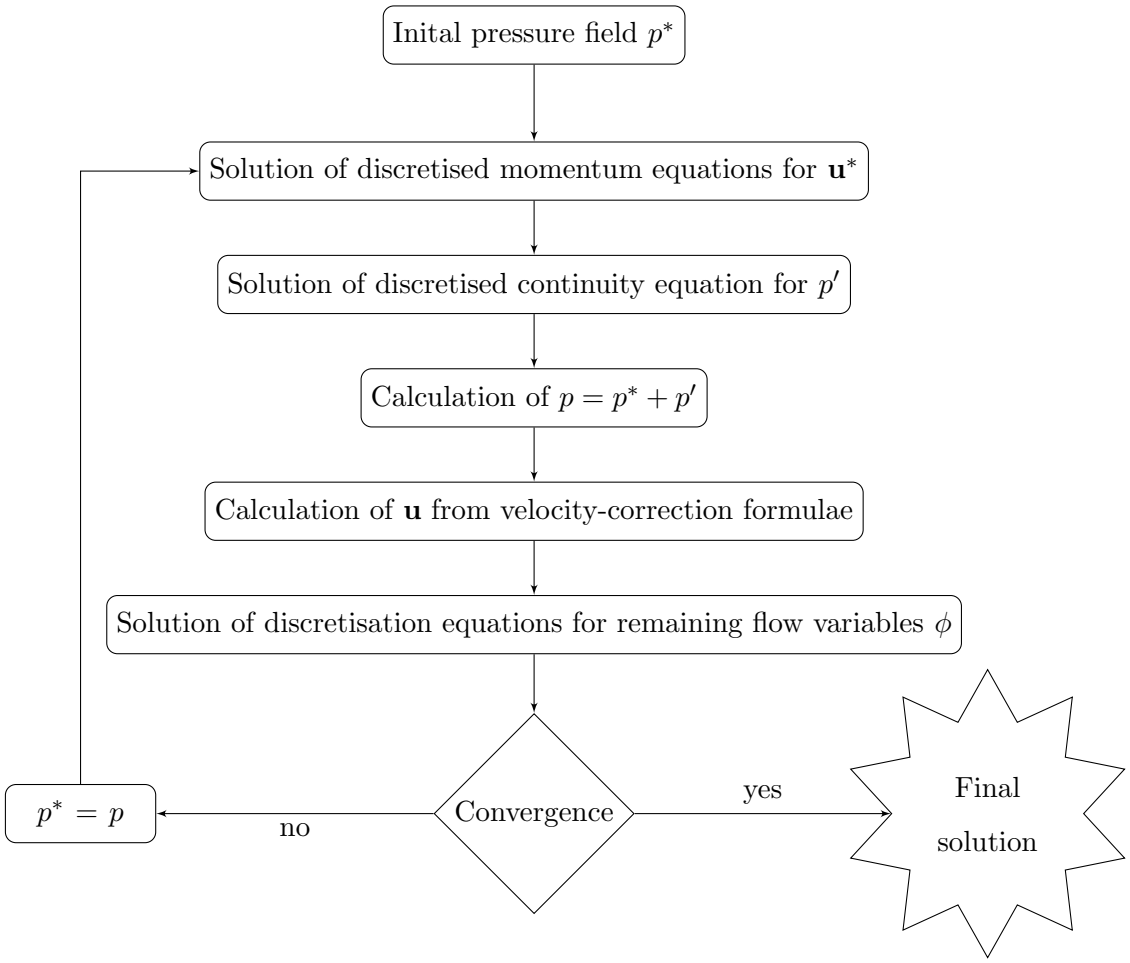

Figure 4.2: SIMPLE algorithm

4.3 Mesh

STAR-CCM+ includes an automated meshing algorithm to generate control volumes based on surface size, cell size limitations and growth rate. These values may be specified explicitly or defined as a proportion of a characteristic dimension, called the *base size*.

All models presented in this work have predominantly hexahedral meshes with trimmed cells at the surface, as illustrated in Figure 4.3. Refinement at wall surfaces or boundaries is achieved using orthogonal prismatic layers. As demonstrated in Figure 4.4, cell width (normal to the wall) increases with distance from the wall. Considering the dimensionless distance from the surface $y^+ \equiv u_\tau y/\nu$, values of $y^+ \leq 1$ enable the model to capture flow behaviour at the developing boundary layer.

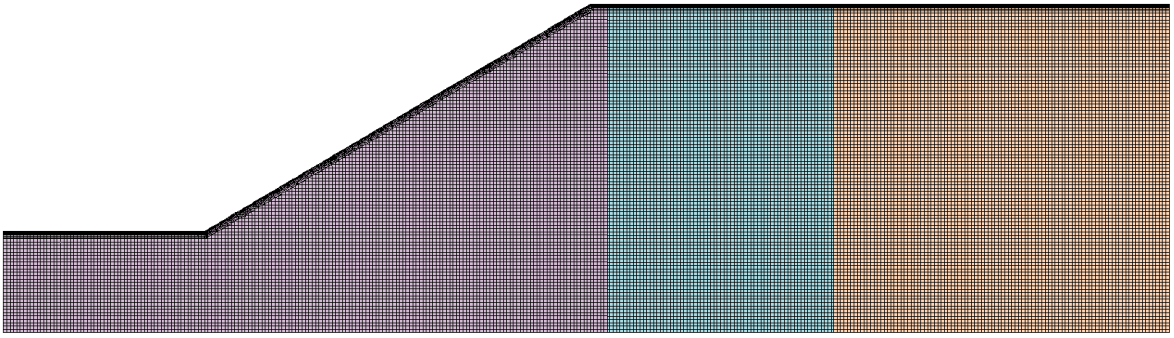

Figure 4.3: 2D mesh of porous medium model

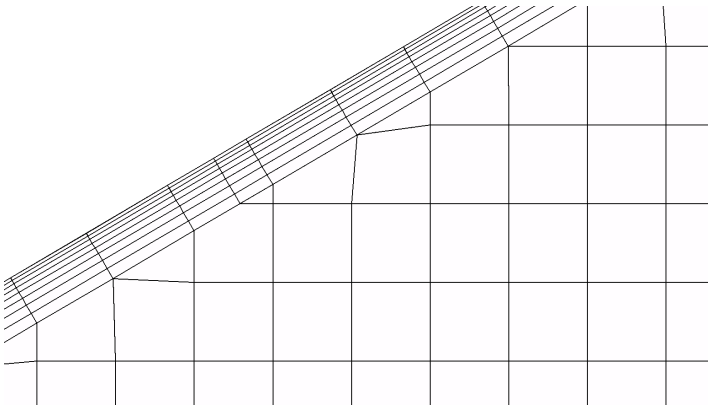

Figure 4.4: Mesh with prism layers at wall boundary and hexahedral cells in main body, with trimmed cells at the interface

Mesh independence studies have been conducted to ensure a well-determined solution. By considering the effect of mesh size on a suitable flow parameter, it is possible to assess the reliance of a

simulation on its computational grid. Table 4.1 and Figure 4.5 present the mesh independence test for the porous medium model. The 27 mm monolith, Re = 2.2×10^4 case with K-W entrance effect is considered. Axial velocity profiles are compared at the pressure outlet and the velocity maximum at the outlet $u_{\max}$ is studied as a characteristic of the final solution.

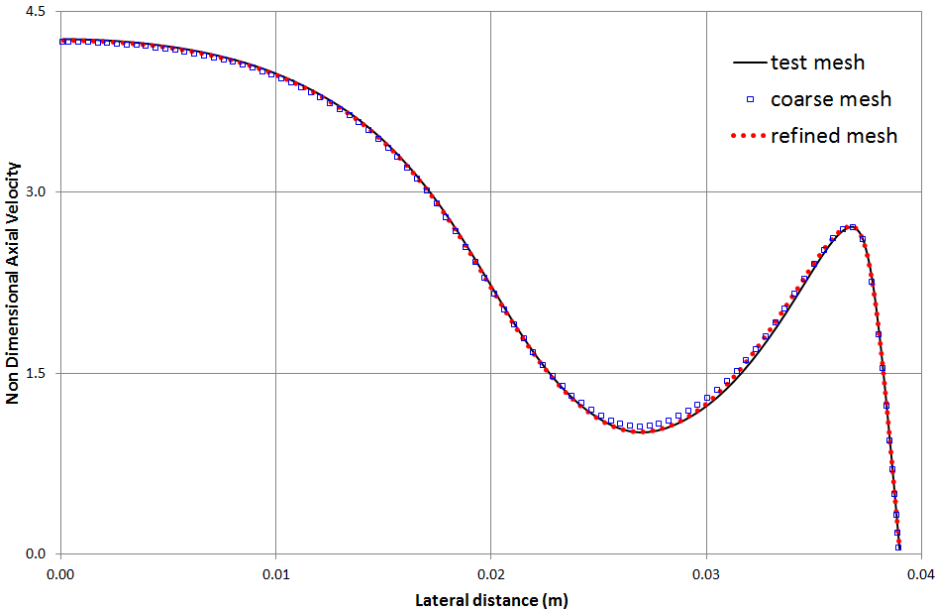

Figure 4.5: Mesh independence test

Table 4.1: Mesh independence test

	Base size (m)	# cells	$u_{\max}$	
test	4.0×10^{-4}	2.8×10^4	4.2707	
refined	3.5×10^{-4}	3.7×10^4	4.2601	$\pm 0.25\%$
coarse	4.5×10^{-4}	2.3×10^4	4.2460	$\pm 0.57\%$

4.4 Modelling the Monolith

The development of a reliable model for the flow through a monolith is challenging. An accurate model must account for the change in pressure due to the compression and expansion of flow as it enters and exits the monolith, as well as friction losses in the channels and losses associated with oblique flow entry. Resolving fluid flow over the whole domain carries high computational demand. An alternative method is to model the monolith as an equivalent continuum, or porous medium, as introduced by Aris, (1977).

4.4.1 Porous Medium Approach

The porous medium approach to modelling the monolith focuses on the overall effect of the substrate rather than the internal flow of individual channels. The method is attractive due to its relatively low computational demand.

The porous region is treated in Star-CCM+ by the inclusion of a porous source term $\mathbf{f}_\mathrm{p}$ in the momentum equations of Eq. 4.2, such that

$$\mathbf{f_p} = -\mathbf{P} \cdot \mathbf{u} \tag{4.6}$$

where $\mathbf{P}$ denotes the porous resistance tensor, defined by

$$\mathbf{P} = \mathbf{P}_\mathrm{i}|\mathbf{u}| + \mathbf{P}_\mathrm{u} \tag{4.7}$$

$\mathbf{P}_\mathrm{i}$ and $\mathbf{P}_\mathrm{u}$ denote the inertial and viscous resistance tensors respectively (CD-adapco, 2013).

The monolith consists of parallel channels with solid walls, so no mass transfer occurs between monolith channels. Moreover, the small size of the channel cross-section means that the transverse flow redistribution inside the channels has minimal effect on the overall velocity profile of the monolith. It is therefore justified to assume unidirectional flow inside the monolith. Consequently, there is negligible pressure loss in the direction normal to the flow and principal losses occur in the streamwise direction. Coefficients for the resistance tensors in the axial direction may be derived via theoretical calculations or measured directly. The CFD studies presented in this work use axial resistance tensor components obtained experimentally for each monolith and suitably high transverse resistance tensors are prescribed.

4.4.1.1 Pressure Drop Due to Channel Flow

Eqs 4.6 and 4.7 give

$$\mathbf{f_p} = -\left(\mathbf{P}_\mathrm{i}|\mathbf{u}| \cdot \mathbf{u} + \mathbf{P}_\mathrm{u} \cdot \mathbf{u} \right) \tag{4.8}$$

i.e. the axial pressure in the monolith is a second order polynomial with respect to superficial velocity.

Axial resistance tensor components were obtained for two monoliths. The monoliths used in this study were of length 27 mm and 100 mm and had identical channel geometry. Coefficient values in the axial direction were derived by fitting a second order polynomial function to the measured values of superficial velocity and pressure drop per unit length to obtain an expression of the form

$$\frac{\Delta P}{L} = \beta u_s^2 + \gamma u_s \tag{4.9}$$

as shown in Figure 4.6. The components of the axial porous resistance tensor are then $\mathrm{P}_{\mathrm{i}x} = \beta$ kg/m^4, $\mathrm{P}_{\mathrm{v}x} = \gamma$ kg/m^{3}s. Unidirectional flow in the monolith is achieved via high transverse resistance tensors $\mathrm{P}_{\mathrm{i}y} = 10^7$ kg/m^4 and $\mathrm{P}_{\mathrm{v}y} = 10^7$ kg/m^{3}s. The porous medium models in this work are two-dimensional, so resistance tensor components need only be defined for x and y (streamwise direction and transverse to streamwise direction, respectively).

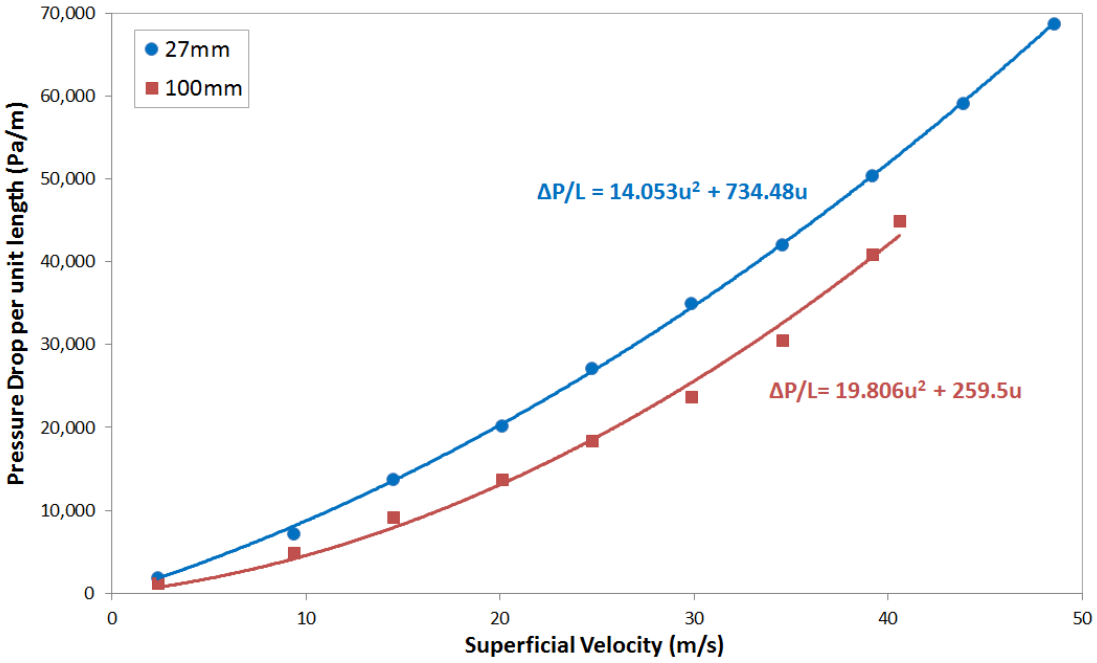

Figure 4.6: Measured pressure drop per unit length as a function of superficial velocity

Pressure losses due to friction in monolith channels may also be derived from theoretical expressions,

e.g. Eqs. 2.2–2.6. Figure 4.7 compares the experimental values with the theoretical Shah and Hagen-Poiseuille (H-P) models. Data points lie close to the Shah curve for low x^+ and approach the H-P line as x^+ increases, demonstrating increasingly developed flow along the monolith at higher velocities. The fact that values from the 100 mm monolith lie directly upon the H-P equation at high x^+ confirms the presence of mostly fully-developed flow in the channels of the longer monolith.

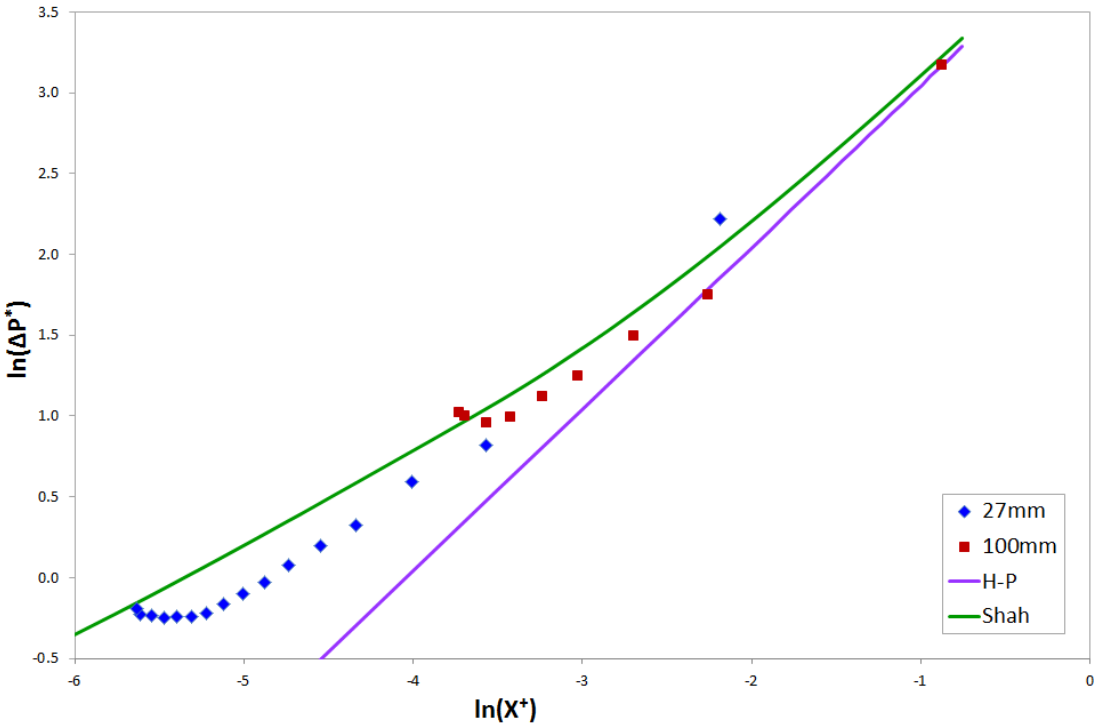

Figure 4.7: Theoretical and measured monolith pressure drop

4.4.1.2 Oblique Entrance Effects

Pressure losses due to oblique entry into the monolith channels are accounted for using the Küchemann-Weber (K-W) expression given in Eq. 2.7. The *critical angle* adaptation limits the pressure drop by assuming constant losses at regions with flow of obliqueness above an angle α_c. Since the K-W effect is found to greatly over-predict velocities in the central downstream region of the longer monolith, this work proposes to neglect the angle of attack for less oblique flow. This is effected by imposing a *subcritical angle*, below which there is no additional pressure loss.

Entrance effects are imposed by specification of the momentum source term $\mathbf{S}_i^v$. The source terms for the K-W oblique entrance effect and its critical angle adaptations are defined by

K-W

$$\mathbf{S}_i^v = -\frac{\rho v^2}{2} \tag{4.10}$$

Critical angle

$$\mathbf{S}_i^v = \begin{cases} -\frac{\rho v^2}{2} & \alpha < \alpha_c \\ -\frac{\rho v_c^2}{2} & \alpha \geq \alpha_c \end{cases} \tag{4.11}$$

Subcritical angle

$$\mathbf{S}_i^v = \begin{cases} 0 & \alpha \leq \alpha_s \\ -\frac{\rho v^2}{2} & \alpha > \alpha_s \end{cases} \tag{4.12}$$

Source term values are calculated from velocity data extracted from the simulation 1 mm upstream of the monolith. The flow here represents sufficient with accuracy the flow behaviour upon entry into the monolith, as demonstrated by Haimad, (1997).

4.4.2 Individual Channels

The individual channels approach resolves the entire geometry by modelling the monolith as a three-dimensional system of multiple parallel channels. Flow profiles in the z-direction (normal to the diffuser plane) having been found to be acceptably uniform (Mat Yamin, 2012), periodicity is presumed in this direction, with symmetry across the cell height. It is therefore sufficient to model half the channel height with half the wall thickness. As for the porous medium model, half the monolith width is included. The symmetry plane passes through the centre of a channel, as illustrated in Figure 4.8.

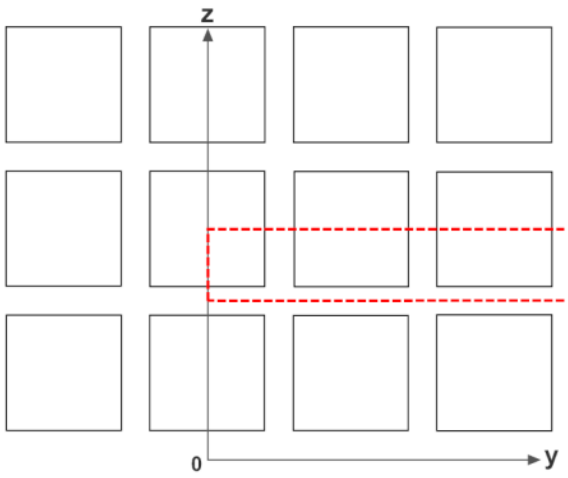

Figure 4.8: Modelled section of monolith

The geometry of the channel domain is defined as per the monolith specification. The monoliths used in this study are unwashcoated with porosity 0.77 and channel hydraulic diameter 1.12 mm. Variation of the cell hydraulic diameter and wall diameter is present, however homogeneity of cell dimensions across the monolith is assumed for the purposes of this study. A nominal cell density of 62 cells/cm^2 gives the domain dimensions shown in Figure 4.9.

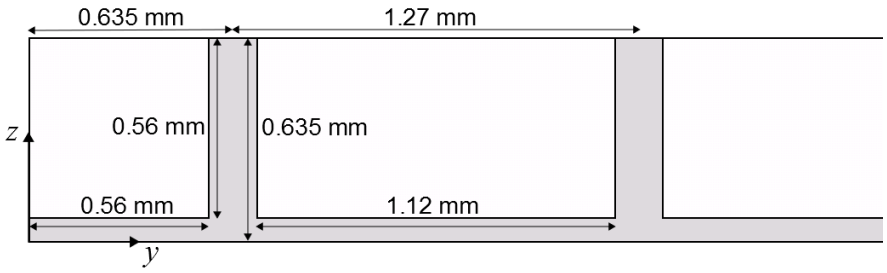

Figure 4.9: Cell dimensions

4.5 Steady Flow Models

Flow in the exhaust system is strongly pulsating, however the assumption of a steady state simplifies both experimental measurement and computational method. The development of an accurate steady state model is an essential initial process for the long-term development of models for direct industrial application.

Regarding the J factor defined in Eq. 2.1, the steady case may be considered as the case of an infinitely long pulse, where J tends to infinity. The simplified nature of the steady model lends itself to the study of different methods for modelling the monolith. Various modelling approaches are presented in this work.

Results, presented in Chapter 5, have been published (Porter et al., 2014; Porter et al., In press) and have also contributed to work by Medina et al., (2015).

Steady state models were developed for monoliths of length 27 mm and 100 mm and flows of Reynolds number 2.2×10^4, 3.0×10^4, 4.2×10^4 and 6.0×10^4 for validation against experimental data.

All steady state simulations in this work model turbulence using the low Re v^2f k-ϵ model with all y^+ treatment, which solves the normal stress function and the elliptic function in addition to k and ϵ (CD-adapco, 2013). The model is used since it provides a good balance between computational demand and accuracy and is thus suitable for recirculating flows (CD-adapco, 2013). The model has been designed to capture near-wall effects in turbulent boundary layers (CD-adapco, 2013) and this has been demonstrated for separating flows (Cokljat et al., 2003). The low-Re method is an extension of the model to the laminar and semi-laminar regions of near-wall flow, where the differential equations for k and ϵ include coefficients dependent on turbulence Reynolds number.

4.5.1 Porous Medium Models

Models using the approach described in Section 4.4.1 are presented.

4.5.1.1 Full Length Monolith

The initial porous medium geometry includes full lengths of the flow rig parts. Figure 4.10 shows the two-dimensional domain. The model is also adapted to include a sleeve wider than the diffuser

outlet. This geometry corresponds to the rig used by Mat Yamin, (2012) and is shown in Figure 4.11. The resistance of the monolith is incorporated using the coefficients of the corresponding quadratic equation $\frac{\Delta P}{L}$, as given in Figure 4.6.

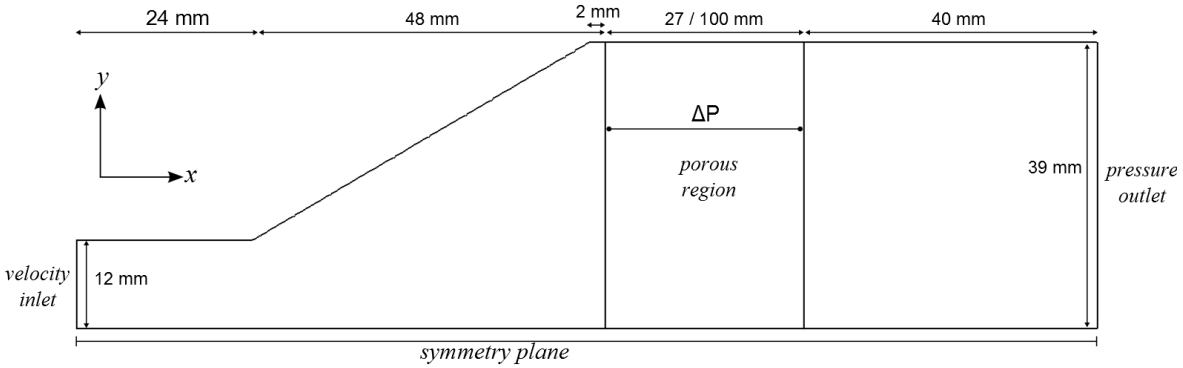

Figure 4.10: Computational domain of porous medium model with fitted outlet sleeve

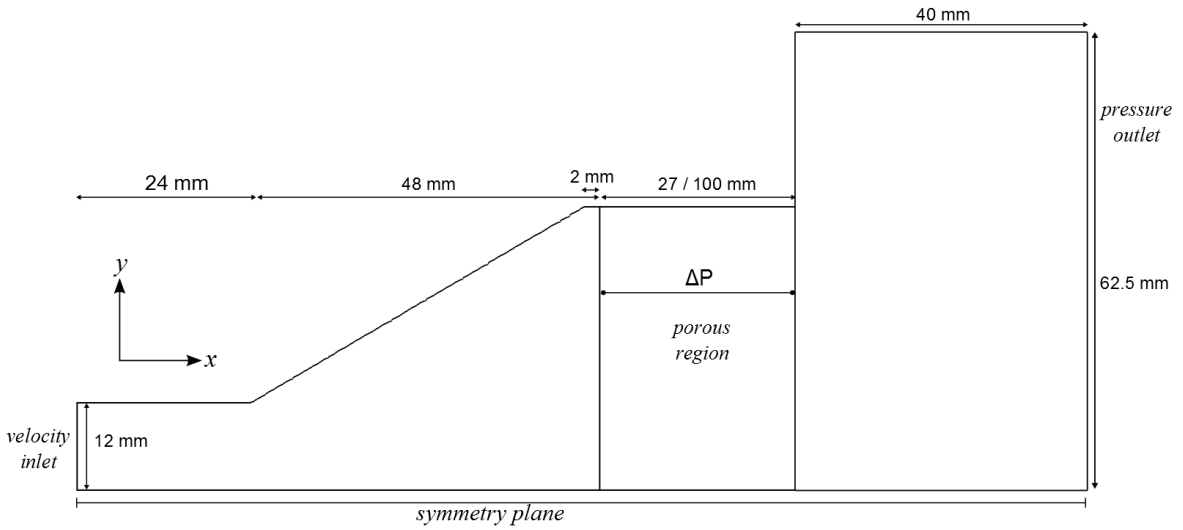

Figure 4.11: Computational domain of porous medium model with wide outlet sleeve

4.5.1.2 Condensed Monolith

Since the porous source term represents only a macroscopic consideration of the region and is applied per unit length, it is possible to reduce the number of cells used to resolve the monolith. By increasing the porous resistance tensor correspondingly, the overall pressure drop remains unchanged and the model is simplified with negligible impact on the solution. For a 'condensed' length l, the

measured axial resistance per unit length of the 27 mm monolith is increased by a factor of $27/l$. Table 4.2 presents the cases studied and the results are displayed in Figure 5.7.

Table 4.2: Condensed monolith model test cases

Length (m)	Number of lengthwise cells	Axial porous resistance tensor coefficients	
		P_{i_x}	P_{v_x}
2.7×10^{-2}	68	14.053	734.48
4×10^{-3}	10	94.858	4957.7
8×10^{-4}	2	474.29	24789

4.5.2 Individual Channels

The individual channels approach assumes a three-dimensional domain, as shown in Figure 4.12. The diffuser and the outlet sleeve include symmetry planes on the xy-plane so that the flow is modelled as planar in these regions, and the channels are modlled using the method described in Section 4.4.2. Figure 4.13 shows the interface between the diffuser and the channels. Prism layers are included at the channel walls in order to capture developing boundary layers, as shown in Figure 4.14.

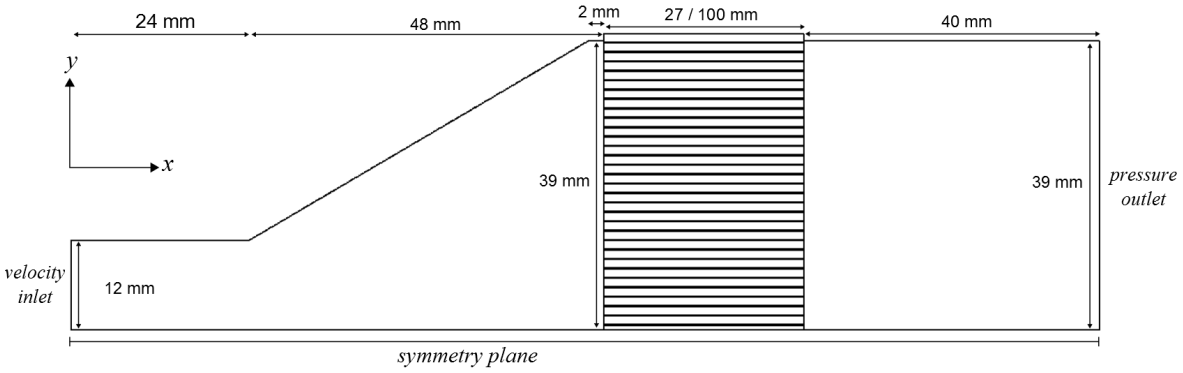

Figure 4.12: Computational domain cross-section of individual channels model

4.5.3 Hybrid Model

Whilst the individual channel model has the advantage of being able to accurately model the behaviour of flow upon and immediately after entrance into the monolith, it carries high computational

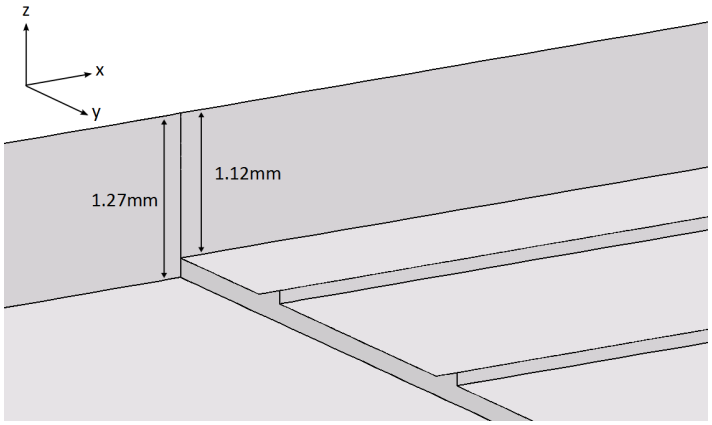

Figure 4.13: Model at diffuser/channels interface

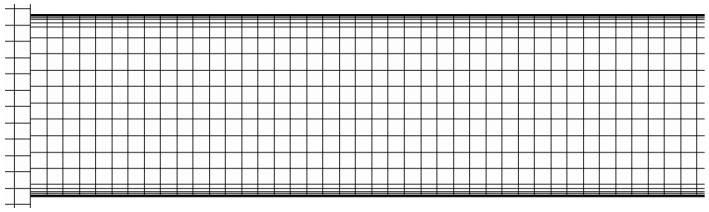

Figure 4.14: Mesh resolution of channel

demand compared to modelling the monolith as a porous medium. A novel hybrid model is therefore developed to combine the two approaches.

The monolith is modelled as a combination of channels and porous media. Individual channels at the entrance to the monolith are able to accurately capture the effects of the flow behaviour immediately downstream of the monolith face, i.e. flow separation in the channels as illustrated in Figure 1.3(b). Once the flow is fully developed, the domain is treated as an equivalent continuum. Figure 4.15 shows the geometry.

The channel section is 13 mm long, sufficient for capturing the effects of oblique entry into the channels. Justification for this arises from predictions by the individual channels model, which are presented in more detail in Section 5.2. For the high Reynolds number case with 27 mm monolith (i.e. with greatest flow development length), the channels observing most oblique flow at the entrance are identifiable. The predicted pressure fluctuation along these four channels is presented in Figure 4.16. Once oblique entry pressure losses have taken effect, the pressure drop is linear and may be therefore approximated using the Hagen-Poiseuille formulation (Eq. 2.6).

A 1 mm porous section downstream of the channels implements the overall pressure drop associated

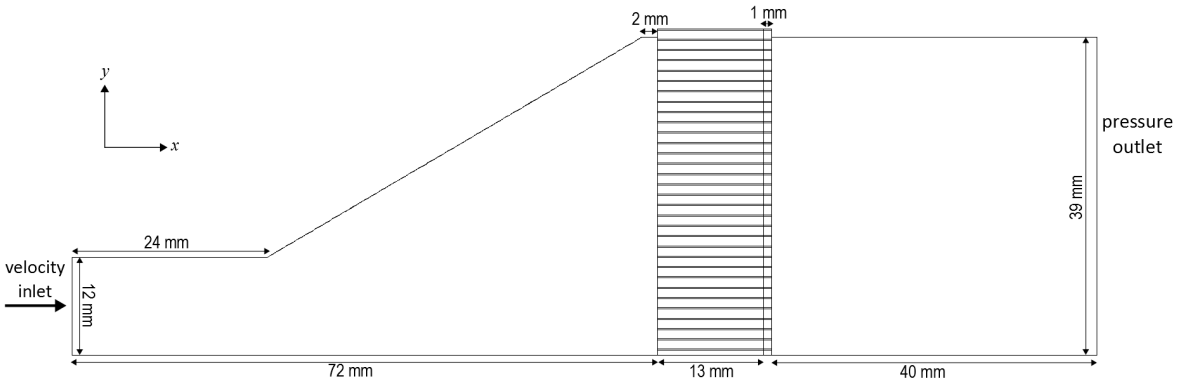

Figure 4.15: Computational domain of hybrid model

with the fully-developed flow, as presented in Figure 4.17. Each channel in the porous section has slip walls, i.e. shear stress $\tau = \mu \partial u / \partial y = 0$, where u and y denote the velocity of the fluid along the boundary and the distance from the boundary respectively. This ensures that no mass flux occurs between channels, whilst allowing the flow to redistribute across the channel width.

Since the Hagen-Poiseuille equation assumes fully-developed flow, the viscous effects of the flow dominate in this region and $\mathbf{P}_\mathrm{i}$ has zero magnitude. Eq. 2.6 may be arranged to give a linear relationship between pressure drop per unit length and channel velocity,

$$\frac{\Delta \mathrm{P}}{L} = \frac{2(F\mathrm{Re}_c)\mu}{d_h^2} u_c \tag{4.13}$$

For a condensed 1 mm porous section representing a length l, the axial viscous resistance coefficient is then defined

$$\mathrm{P}_{\mathrm{v}x} = \frac{2(f\mathrm{Re}_c)\mu}{d_h^2} l \tag{4.14}$$

Transverse resistance coefficients are set to 0 to allow flow redistribution within each channel of the porous region.

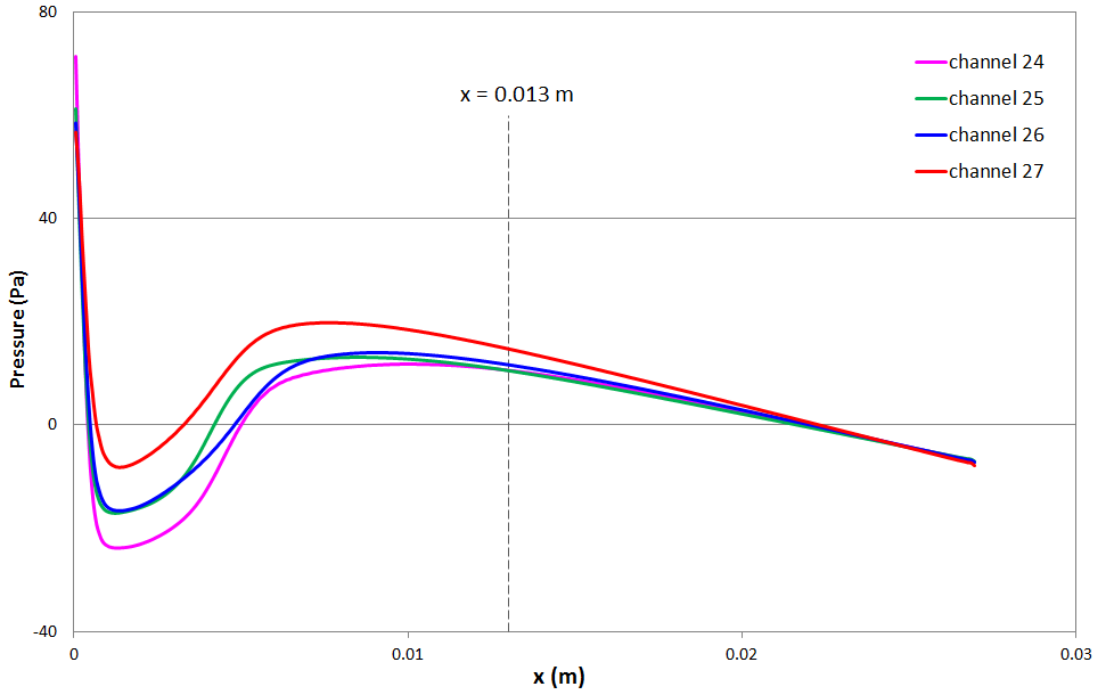

Figure 4.16: Predicted pressure fluctuation along channels with most oblique entrance flow. $L = 27$ mm, Re $= 6.0 \times 10^4$. The legend refers to the channels considered, where the individual channels of the model are numbered from the centre outwards, such that channel 1 is the half channel lying on the symmetry plane, and channel 31 is the outermost channel next to the diffuser wall.

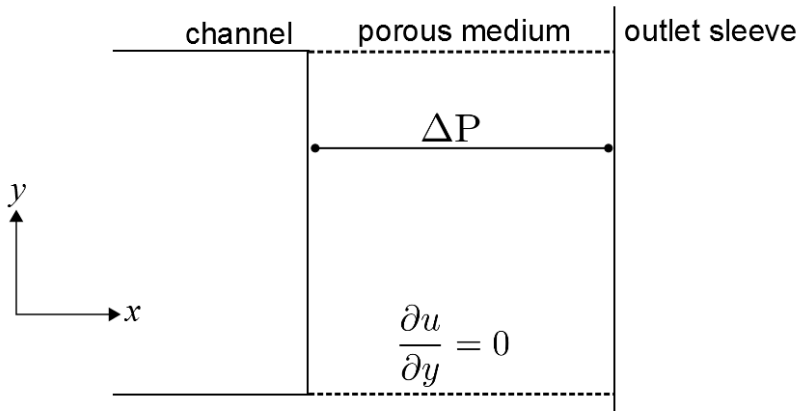

Figure 4.17: Hybrid model schematic of downstream monolith region (one channel)

4.6 Pulsating Flow Model

A time-dependent model of pulsating flow is developed and applied to three flow regimes studied experimentally at Coventry University by Mat Yamin, (2012), as presented in Table 3.2. The results, given in Chapter 6, have been presented at an international conference (Porter et al., 2015) and have also contributed to the study by Saul et al., (2015).

A combination of Reynolds numbers of 2.2×10^4 and 4.2×10^4, and frequencies of 50 Hz and 100 Hz, present three flows, characterised by the ratio J. Reynolds numbers are defined by the cycle-average mean inlet velocity and the hydraulic diameter of the nozzle.

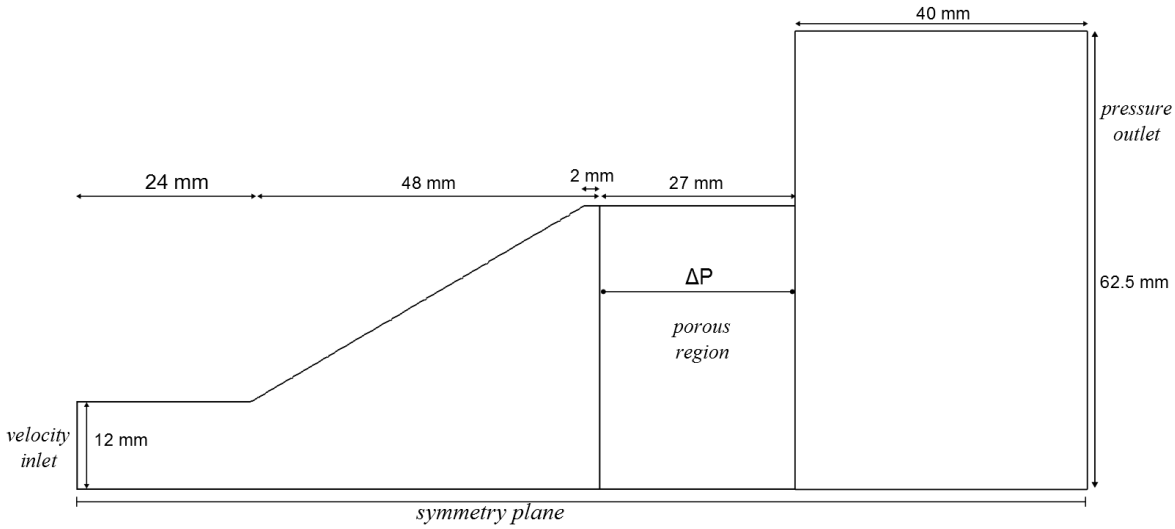

Figure 4.18: Geometry schematic

Inlet velocity is uniform and periodic. Velocities were extracted directly from phase-averaged PIV data for the ten time-steps of each pulse. To obtain a smooth inlet velocity profile in the simulation, average values from the furthest upstream measurements were interpolated at each computational time-step using B-spline interpolation. Pulse shapes, given in Figure 4.19, are approximately sinusoidal and are similar for the three cases.

The monolith is modelled using the porous medium method detailed in Section 4.4.1. The formulation derived by Küchemann and Weber, (1953) (Eq. 2.7) is included as an approximation of the pressure losses due to oblique channel entry. This is sufficient for the purposes of this study. Entry losses primarily affect flow in the monolith and downstream of the monolith outlet, however steady flow studies for the geometry considered (wide outlet sleeve) show unsatisfactory agreement in the downstream region and thus the diffuser is the principal area of interest for this study.

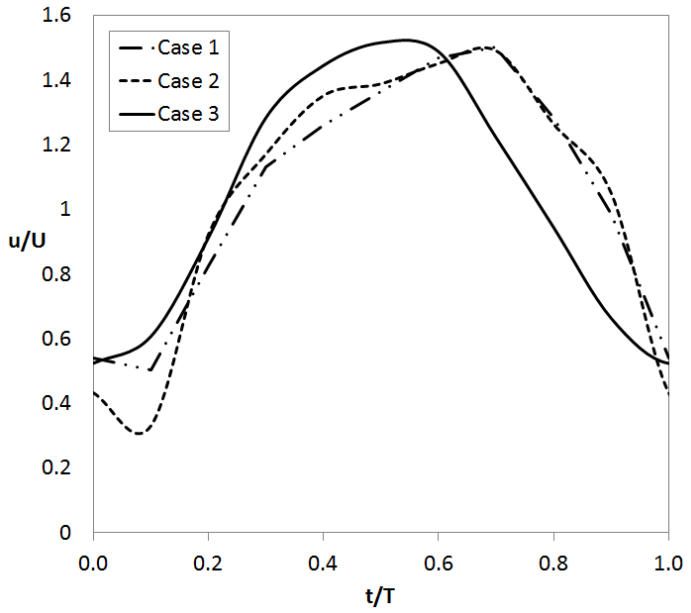

Figure 4.19: Inlet pulse shape, with time t normalised by pulse period T.

Turbulence is modelled using the linear pressure-strain two-layer Reynolds Stress Transport (RST) model. During initial investigation, the v^2f model resulted in multiple recirculation regions in the diffuser. The model was disregarded due to the extent of disagreement with experimental data, and the RST model was found to produce more physically realistic results.

The model incorporates the linear pressure-strain model of Gibson and Launder, (1978) into a two-layer (shear driven) formulation, as suggested by Rodi, (1991). The model inherently accounts for anisotropy of the turbulent stress field since transport equation are solved for all specific Reynolds stress tensor components (CD-adapco, 2013).

An implicit unsteady scheme is used for time integration, with first-order temporal discretisation. Each 1×10^{-4} s time-step converges over a minimum of 1000 inner iterations.

The transient model was initialised from the converged solution of an equivalent steady state model. The simulation was run until reaching a periodic solution, and a length of ten cycles was found to be sufficient. Figure 4.20 shows the evolution of maximum axial velocity throughout ten cycles for Case 2.

Transient flows models must satisfy the CFL condition, which is a necessary, but not sufficient, requirement for the convergence of a solution. Considering the sum of the ratios of time-step Δt to the characteristic convection time $\Delta x_i/u_{x_i}$ for the spatial component i, the *Courant number* C is

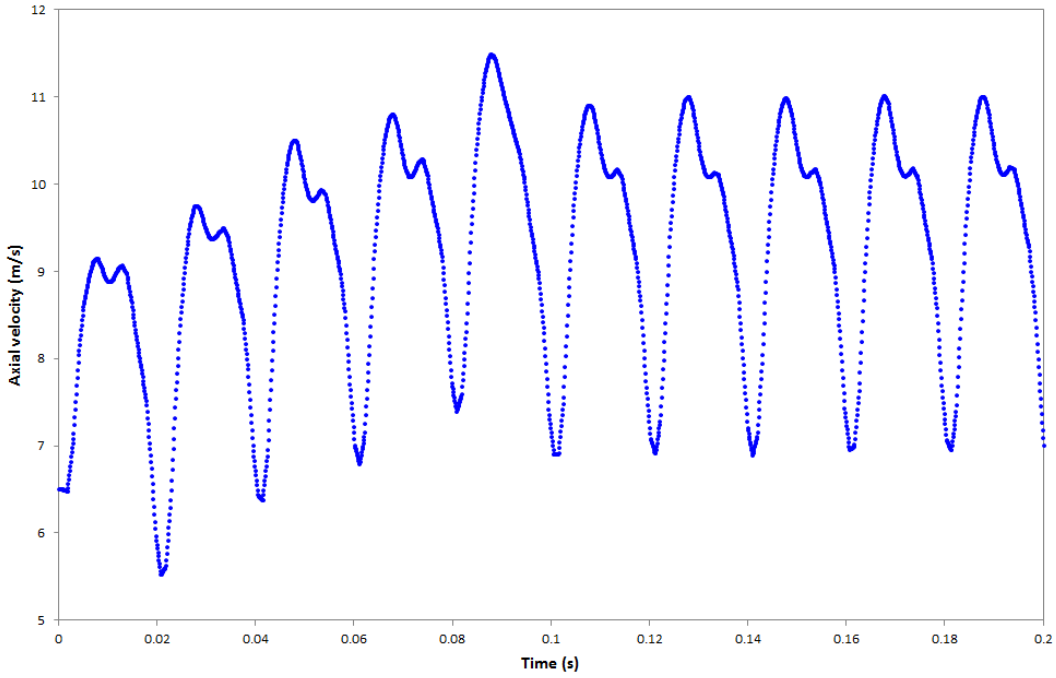

Figure 4.20: Maximum axial velocity at pressure outlet, showing the development of periodicity for Case 2

defined

$$C = \Delta t \sum_{i=1}^{n} \frac{u_{x_i}}{\Delta x_i} \tag{4.15}$$

for a system in n dimensions. The CFL condition,

$$C \leq C_{\max} \tag{4.16}$$

requires that the physical domain of dependence at a point is contained within the numerical domain of dependence, i.e. the temporal discretisation of a numerical solution is sufficiently refined for the propagation of information in the spatial discretisation. $C_{\max} = 1$ when an explicit unsteady solver is used. However, an implicit unsteady solver is less sensitive to numerical instabilities and thus values greater than unity may be acceptable.

5 | Steady Flow

This chapter presents the results from steady flow models presented in Section 4.5. Flow parameters predicted by the CFD models are compared with experimental data collected during this work and also by Mat Yamin, (2012). Results have been published (Porter et al., 2014) and also contributed to the study by Medina et al., (2015).

5.1 Porous Medium Model

Results from the porous medium model detailed in Section 4.4.1 are presented. The flow structure in the diffuser is discussed first. The approaches for simulating the pressure drop across the monolith are then presented, and the analysis is repeated to a case with a wide outlet sleeve. Finally, a 'condensed monolith' approach is discussed.

Figure 5.1 illustrates the simulated flow behaviour of the model. Across the porous section, transverse velocity is negligible due to extremely high resistance tensors and thus the shape of the flow profile is preserved along the monolith length. The jet spreads in the sleeve downstream and a boundary layer develops at the sleeve wall.

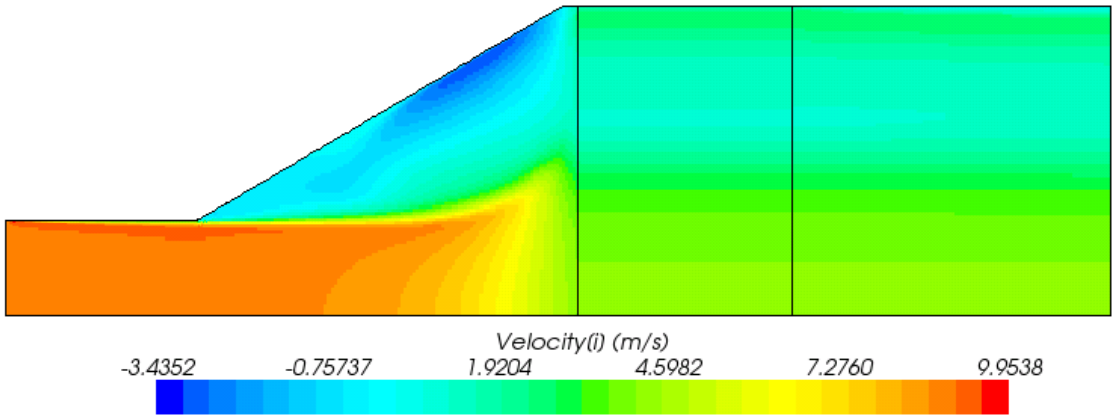

Figure 5.1: Axial velocity field prediction using porous medium approach model.
$L = 27$ mm, Re $= 2.2 \times 10^4$.

Diffuser

Figure 5.2 presents a comparison of CFD and PIV velocity magnitudes in the diffuser for four Reynolds numbers. A planar jet, separating from the diffuser wall at its expansion, traverses the diffuser and spreads sharply immediately upstream of the monolith. Most of the flow enters the monolith, and part of the flow recirculates between the jet and the diffuser wall. These recirculation regions then 'squeeze' the jet.

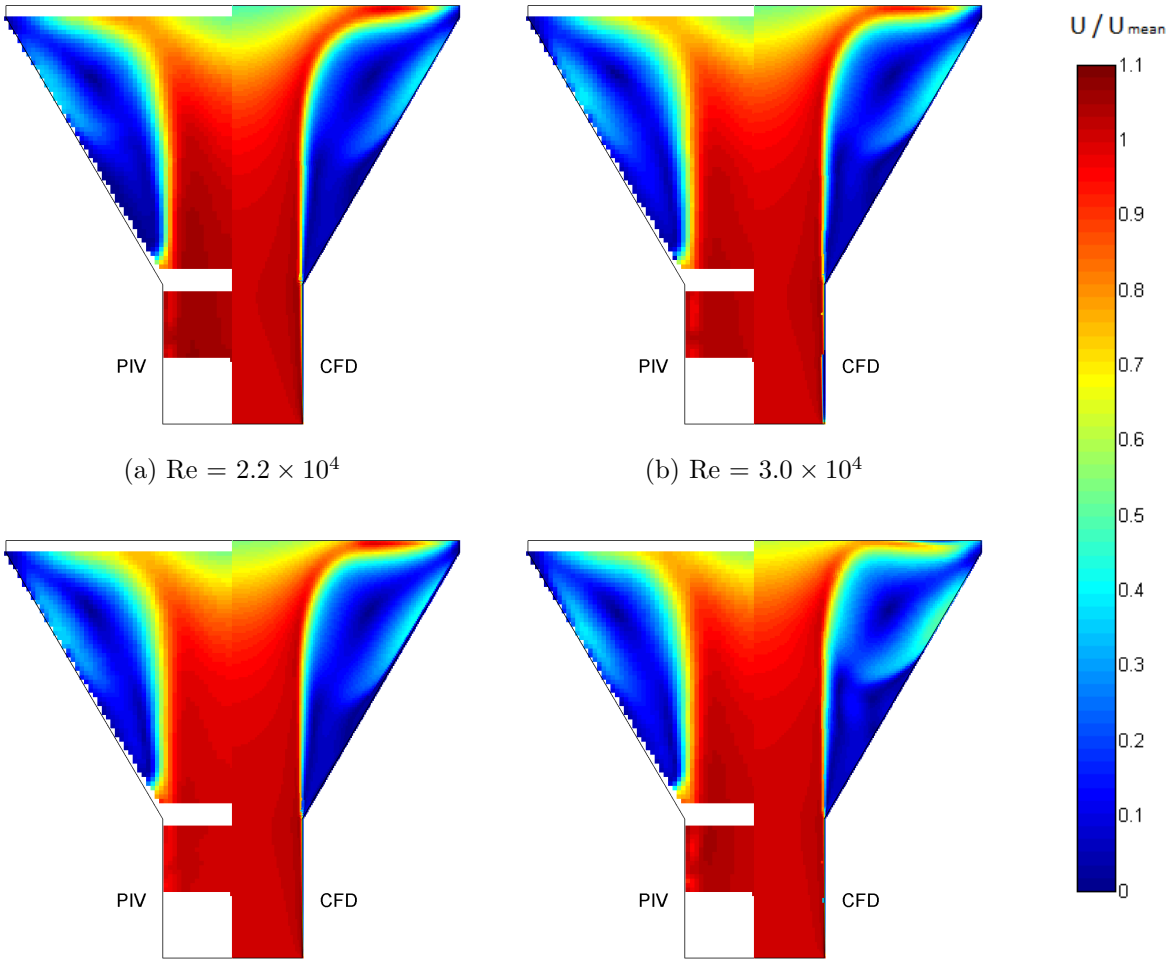

(a) Re = 2.2×10^4 (b) Re = 3.0×10^4

(c) Re = 4.2×10^4 (d) Re = 6.0×10^4

Figure 5.2: Velocity fields in diffuser upstream of 27 mm monolith

CFD predictions show a thinner shear layer at the jet periphery than PIV, leading to larger width of the potential core. This shows an underestimation of mixing by the model, also illustrated by differences in the shape of the recirculation region. The shear layer of the PIV results follows a gentler

curve. Narrowing of the jet width near the point of expansion indicates the influence of the vortex on the jet, whereas CFD shows weaker interaction between the recirculation region and the upstream flow of the diffuser.

Close to the monolith face, PIV shows the jet spreading further upstream of the monolith face than predicted by CFD, and this distance increases with Reynolds number. The recirculating flow then occurs further upstream, 'squashing' the jet at the most upstream point possible, close to the expansion of the diffuser.

Flow immediately upstream of the monolith face is further analysed via comparison of velocity profiles near the diffuser outlet. Velocity profiles are extracted at three cross-sections in the diffuser: 2.5 mm, 5.55 mm and 10.13 mm upstream of the monolith face, as illustrated in Figure 5.3. The 2.5 mm upstream cross-section is studied since it is the closest measured distance to the monolith.

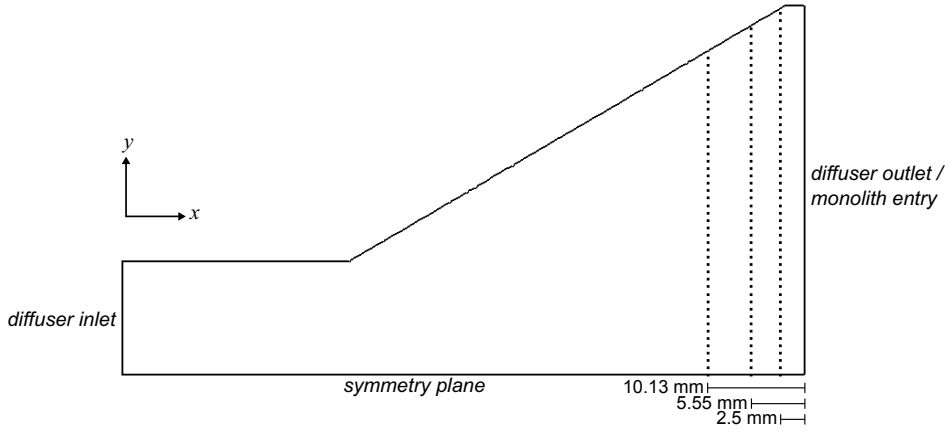

Figure 5.3: Location of examined cross-sections in diffuser

Figure 5.4 presents the axial and transverse velocity components at these locations for the 27 mm monolith configuration. Upon approach to the monolith face, the central jet widens and flattens, and flow enters individual monolith channels at an increasingly oblique angle.

Profiles are in good qualitative agreement with experimental data except immediately upstream of the monolith (maximum transverse velocity predicted by CFD up to 34% higher than PIV at a distance of 2.5 mm). High in the central region and low elsewhere, axial velocities show comparative over-preservation of the potential core, even at the location closest to the monolith face. The steeper gradient exhibited by CFD predictions in the shear layer shows the underestimation of mixing by the model, leading to an over-predicted jet width. Well-matched transverse velocities in the central region show that the model is correctly predicting the spreading effect of the monolith resistance on

the flow in this area, however over-predicted obliqueness of the flow outside of the central jet shows an under-predicted level of spreading at the monolith face. Part of the flow does not enter the channels and instead moves towards the wall of the diffuser outlet, resulting in a build-up of pressure and incurring secondary velocity maxima near the wall (Figure 5.4).

Velocity fields in the diffuser have been found to highly similar upstream of the 27 mm and 100 mm monoliths (Mat Yamin et al., 2013). A comparison of CFD and PIV is only made upstream of the 27 mm monolith as any disagreements are deemed to be consistent across systems with different length monoliths.

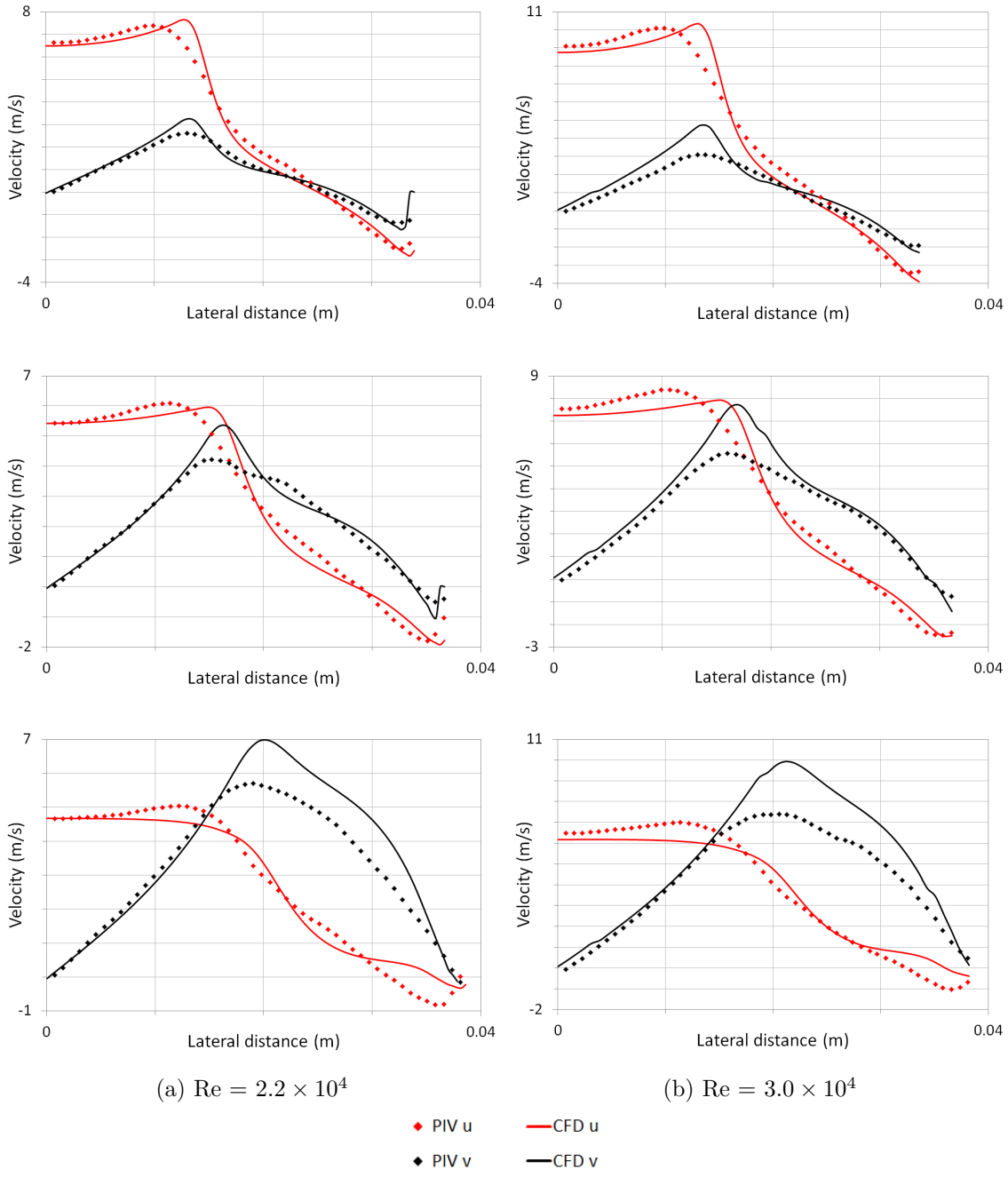

(a) Re = 2.2×10^4 (b) Re = 3.0×10^4

Figure 5.4: Velocity profiles in diffuser 10.13 mm (top), 5.55 mm (centre) and 2.5 mm upstream of 27 mm monolith. u and v respectively denote axial and transverse velocity.

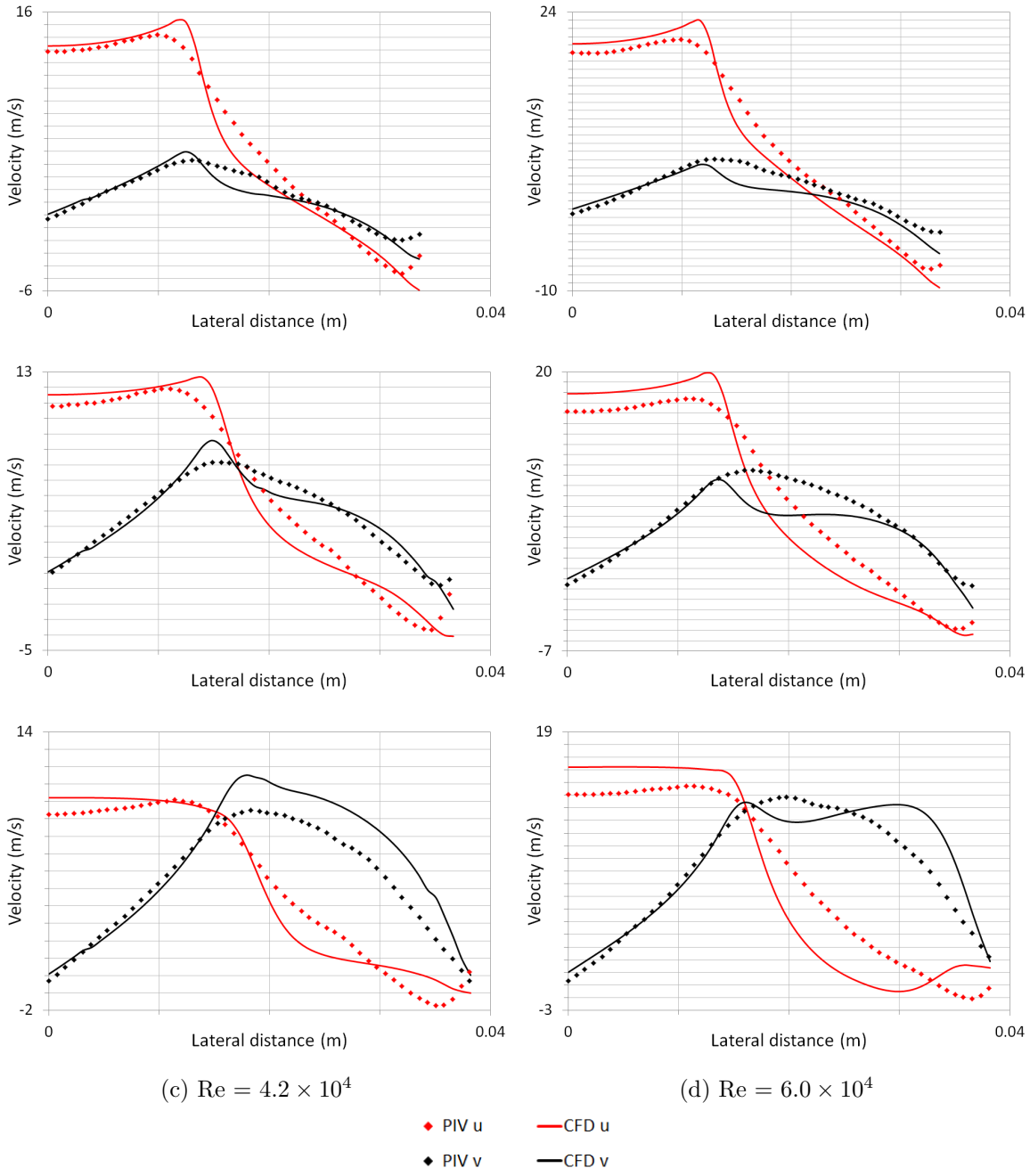

(c) Re $= 4.2 \times 10^4$ (d) Re $= 6.0 \times 10^4$

Figure 5.4: Velocity profiles in diffuser 10.13 mm (top), 5.55 mm (centre) and 2.5 mm upstream of 27 mm monolith. u and v respectively denote axial and transverse velocity. (cont.)

Oblique Entrance Effects

Velocity profiles downstream of the monolith are representative of flow inside the monolith, therefore they are often used as part of the design process for the assessment of flow uniformity. Figure 5.5 compares velocity profiles downstream of the monolith. HWA measurements are compared to predictions from CFD models with various oblique entrance effect formulations, namely the K-W, critical angle and subcritical angle formulations given in Section 4.4.1.2. HWA measurements were taken across the full width of the outlet sleeve. The velocity profiles denoted by 'HWA 1' and 'HWA 2' in Figure 5.5 show measurements either side of the symmetry plane of the system, and variability between the two measurements is observable. Similar variability of around ±5% was observed by Mat Yamin, (2012).

The model was first run with only pressure losses associated with axial flow taken into account (Figure 5.5, solid green curve). As observed by Benjamin et al., (1996), such a model flow underestimates the maldistribution of the flow downstream. Maximum velocities are underpredicted and the jet width is very large, with little to no trough in the profile. Secondary maxima are also slightly underpredicted. Agreement is particularly poor for the shorter monolith (Figure 5.5(a)–(d)), and the discrepancy in maldistribution increases with Re, with a difference in maxium velocity of 0.3 u/U shown in Figure 5.5(d). However, disagreement of flow maldistribution for the longer monolith is less severe and does not noticeably depend on Re (Figure 5.5(e)–(h)).

Inclusion of the entrance effect introduced by Küchemann-Weber (Eq. 2.7) dramatically increases flow maldistribution downstream of the monolith. The profile is in better qualitative agreement with the experimental data but the non-uniformity of the flow is now overpredicted (Figure 5.5, solid black curve).

For the shorter monolith, the inclusion of an oblique entrance effect markedly improves the prediction of the flow profile and velocity maxima at the centre. Values at sencondary maxima are also increased, now overpredicting those measured by HWA. The high Re cases show a particularly overly maldistributed flow, with very low axial velocities at the trough. The case with highest inlet velocity (Figure 5.5(d)) even features negative axial velocity values. This suggests that the resistance presented by the porous region is not sufficient to confine the recirculation zone to the diffuser and that flow is entrained from inside the porous region and downstream.

For the longer monolith, the maldistribution is highly overpredicted and does not agree well with the relatively flat profile measured by HWA. Comparing predictions from models with and without entrance effect, the inclusion of an oblique entrance effect for the longer monolith case generally reduces

the accuracy of CFD predictions. Secondary maxima are well-matched for low Re only. Over-predicted velocities at the wall for high Re cases suggest that it may not be necessary to incorporate pressure losses at locations of extremely transverse flow. This may be achieved by 'capping' the magnitude of losses due to oblique entry using a critical angle formulation, as presented in Sections 2.2 and 4.4.1.2.

A critical angle entrance effect (Eq. 2.11) is tested for $\alpha_c = 69°, 75°, 81°$ (Figure 5.5, solid yellow, orange and red curves respectively). For certain cases only small portions of flow reach highly oblique angles and a critical angle of 81° makes negligible difference to the downstream velocity profile, particularly for the longer monolith. As the critical angle is reduced, maldistribution in the downstream profile decreases. Keeping the pressure loss constant for flow of obliqueness α_c and above incurs higher velocities at the corresponding locations downstream. The maximum velocity is thereby reduced, as is the secondary maximum at the wall. For the shorter monolith, a critical angle of 81° provides the necessary pressure loss correction to sufficiently improve the predicted profile. The longer monolith high Re cases are best improved when $\alpha_c = 69°$ (Figure 5.5(g),(h)), however this overpredicts maxima and underpredicts secondary maxima for the low Re cases. With the objective of identifying a model suitable for all cases, a critical angle of 69° is considered as providing the most consistent agreement across the two monolith lengths studied.

The fact that the inclusion of an oblique angle pressure loss over-predicts velocity maxima on the centre-line for the 100 mm length monolith suggests that the angle of attack at the central region of the monolith face may be insignificant. Neglecting pressure loss for flow at low angles below 40°, the sub-critical angle entrance effect (Eq. 4.12) is applied to the 100 mm monolith system with low Re (Figure 5.5(e)). The adjustment has a very minimal effect on the profile, slightly flattening and widening the central jet.

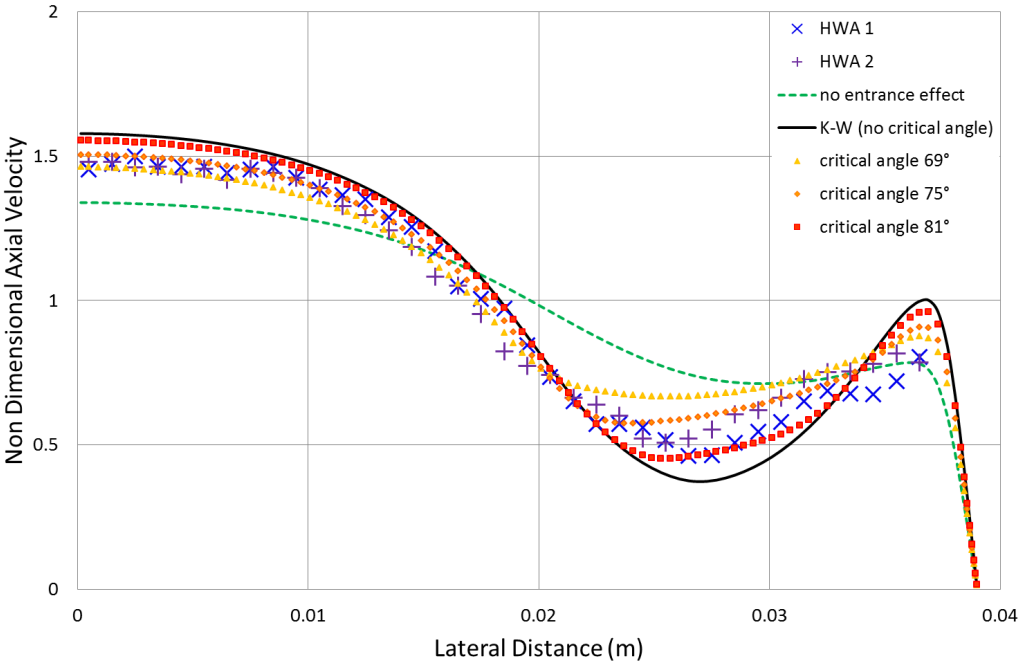

(a) $L = 27$ mm, $\mathrm{Re} = 2.2 \times 10^4$

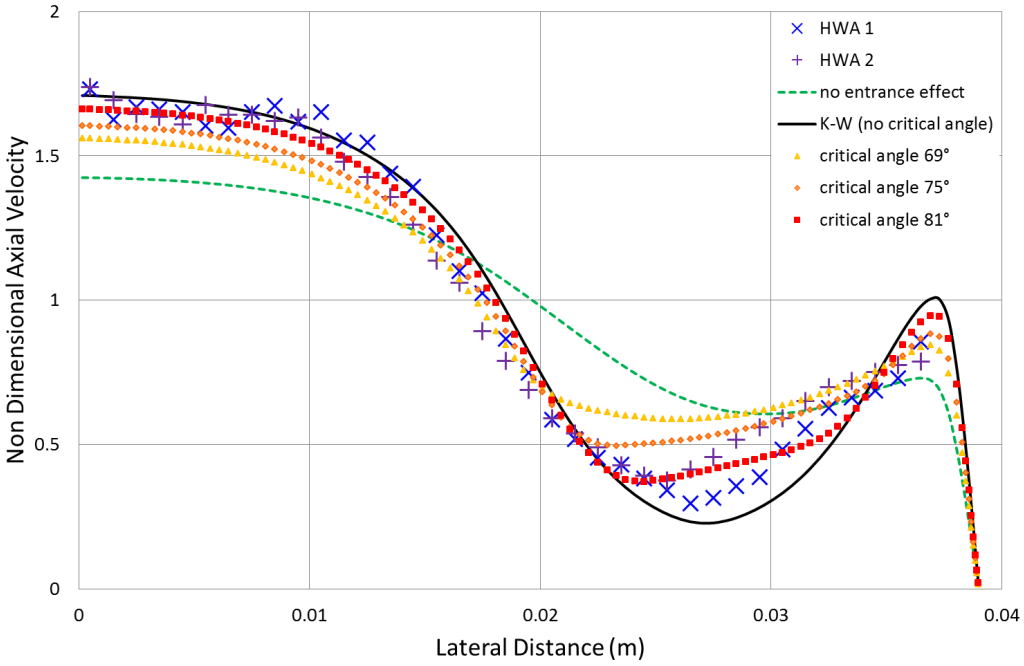

(b) $L = 27$ mm, $\mathrm{Re} = 3.0 \times 10^4$

Figure 5.5: Axial velocity profiles 40 mm downstream of monolith

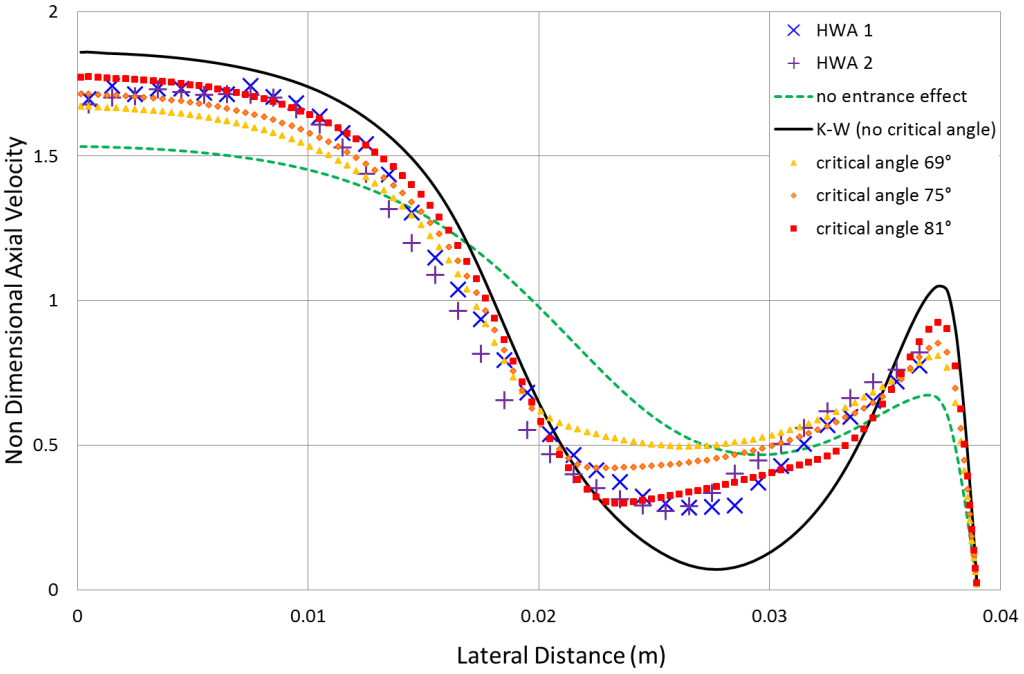

(c) $L = 27$ mm, $\mathrm{Re} = 4.2 \times 10^4$

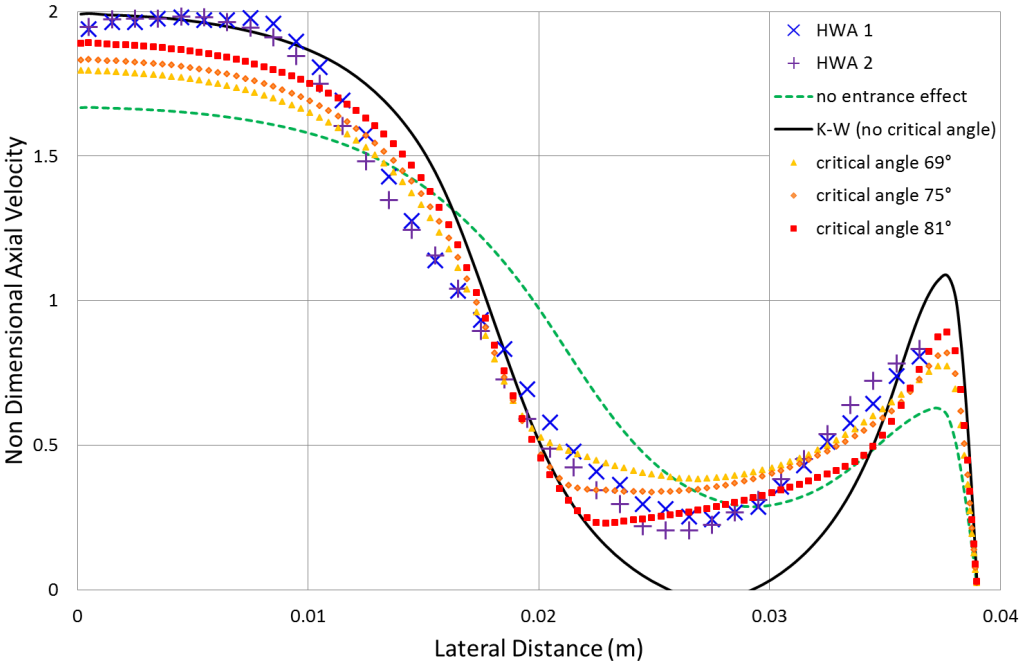

(d) $L = 27$ mm, $\mathrm{Re} = 6.0 \times 10^4$

Figure 5.5: Axial velocity profiles 40 mm downstream of monolith (cont.)

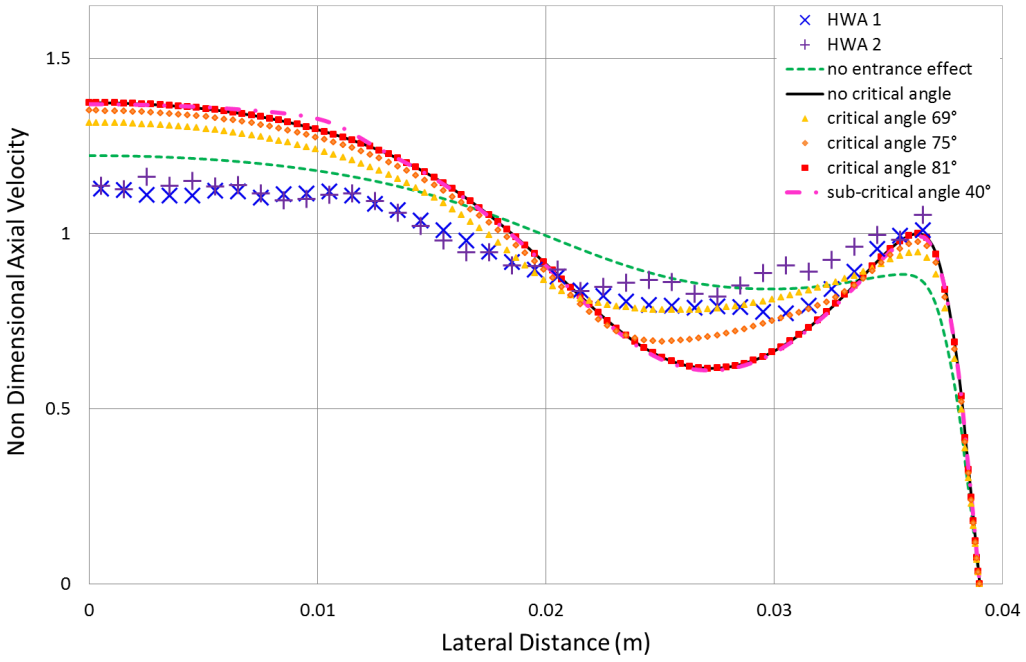

(e) $L = 100$ mm, $\mathrm{Re} = 2.2 \times 10^4$

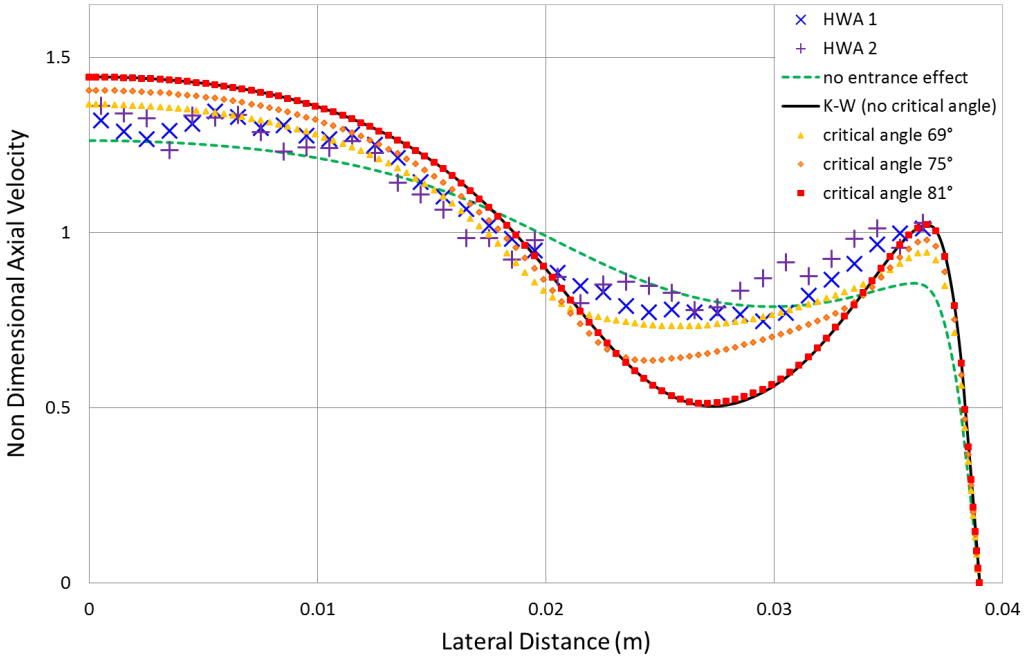

(f) $L = 100$ mm, $\mathrm{Re} = 3.0 \times 10^4$

Figure 5.5: Axial velocity profiles 40 mm downstream of monolith (cont.)

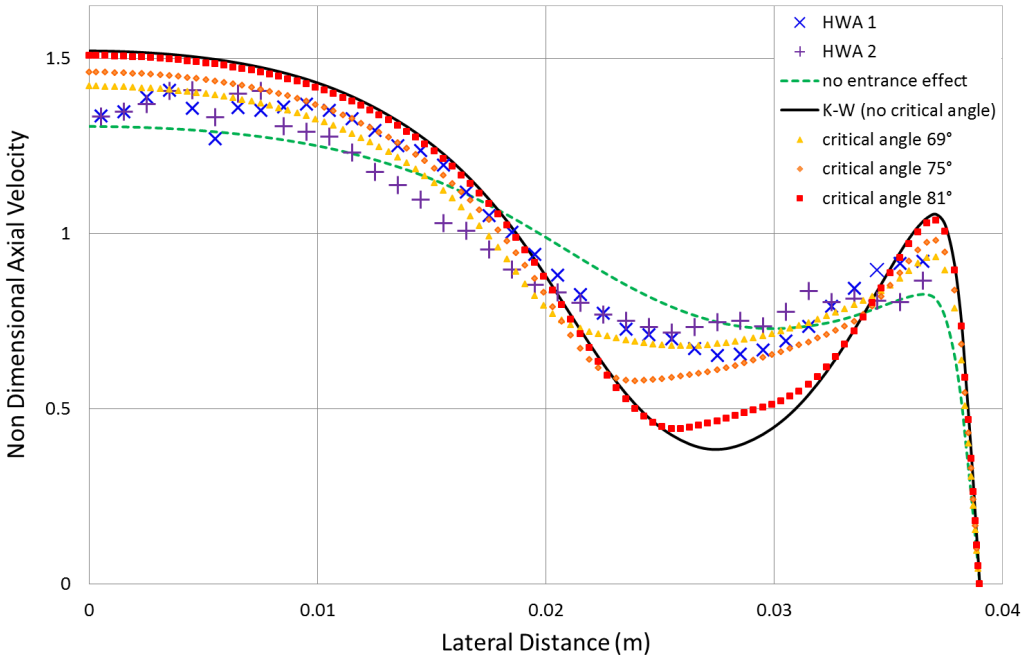

(g) $L = 100$ mm, $\mathrm{Re} = 4.2 \times 10^4$

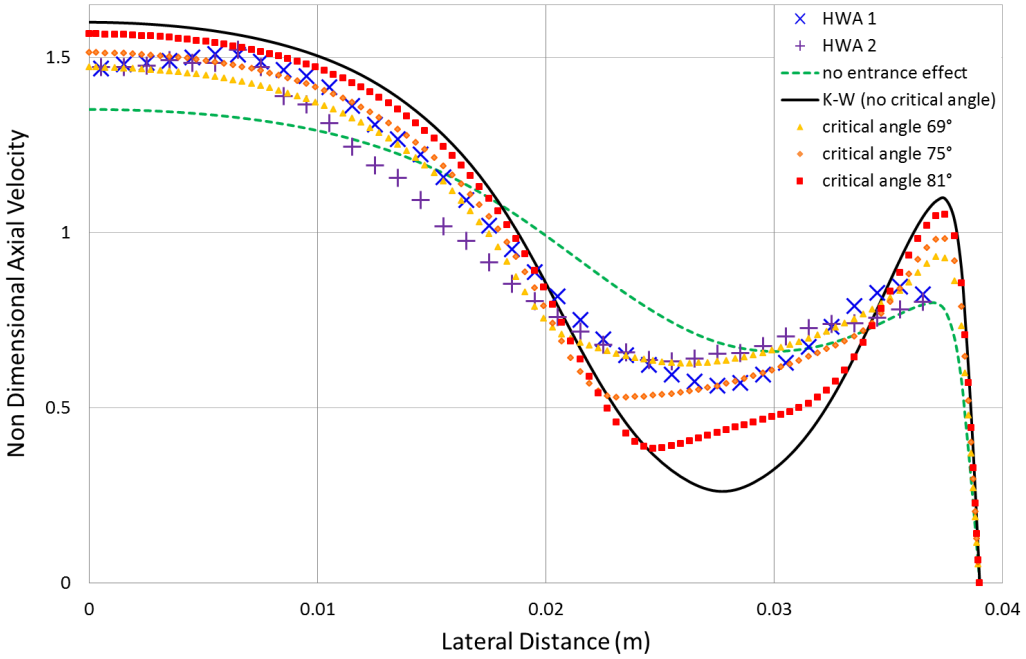

(h) $L = 100$ mm, $\mathrm{Re} = 6.1 \times 10^4$

Figure 5.5: Axial velocity profiles 40 mm downstream of monolith (cont.)

Wide Outlet Sleeve

Additional simulations were carried out in order to compare CFD with the steady flow measurements taken by Mat Yamin, (2012), with an outlet sleeve wider than the diffuser outlet. CFD predictions are presented for the entire outlet width, however HWA measurements are only available for the central section of the sleeve corresponding to the diffuser outlet dimensions. The HWA profiles 'HWA 1' and 'HWA 2' denote measurements either side of the symmetry plane of the system. Velocities, presented in Figure 5.6, are normalised by the mean outlet velocity U_{out}.

A single case is considered for the wide sleeve system, with $L = 27$ mm, $\text{Re} = 3.0 \times 10^4$. Predictions from the analogous fitted sleeve case are given in Figure 5.5(b).

The porous medium model does not predict the downstream velocity profile well for this geometry. The porous medium model with pressure losses associated only with unidirectional flow results in a wide central jet with underpredicted maximum velocity. Inclusion of an entrance effect based upon angle of attack dramatically increases flow maldistribution. Maximum values at the centre are in good agreement and the shape of the core jet is well matched, however velocities are in poor agreement outside of the central region. The introduction of a critical angle of 69° improves predictions, as seen for fitted sleeve cases. Magnitudes at the trough and secondary maximum are in excellent agreement, with the global maximum velocity somewhat underpredicted.

The pressure loss calculation has negligible effect on the predicted lateral distance of the secondary maximum from the centre-line and it is overpredicted by all porous medium models presented. However the predicted distance of the trough form the centre-line is reduced, and therefore improved, by the dependency of the pressure drop on the obliqueness of flow entering the monolith, demonstrating the importance of accurately capturing oblique entry effects.

The wide sleeve system is only considered for one case since the study predominantly serves to demonstrate the limitations of the porous medium approach.

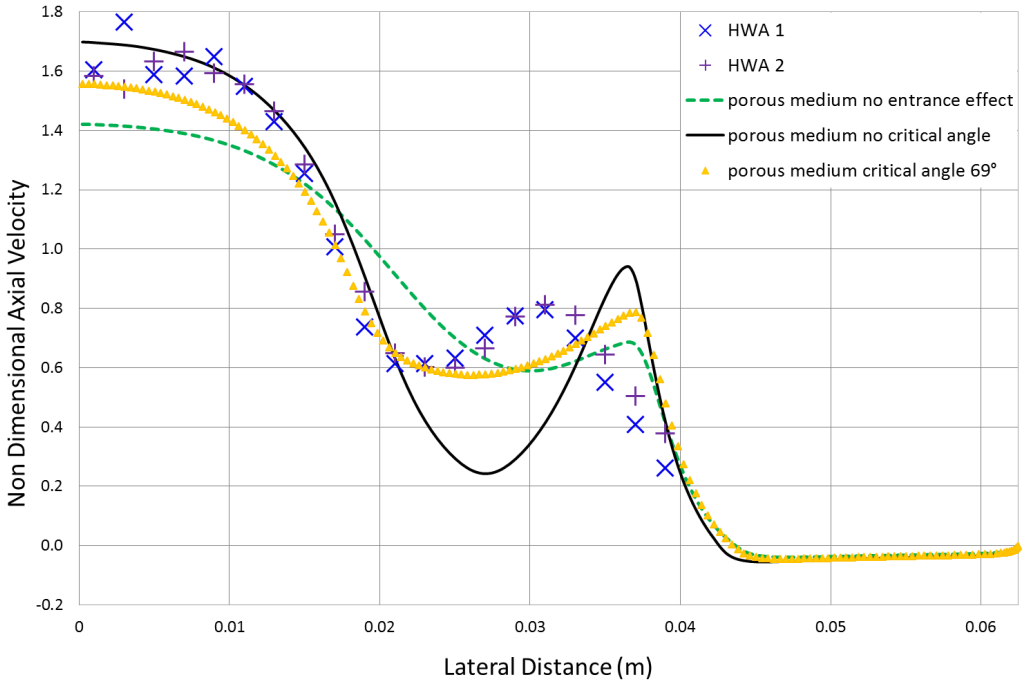

Figure 5.6: Velocity profiles downstream of porous medium model with wide outlet sleeve. $L = 27$ mm, $\mathrm{Re} = 3.0 \times 10^4$.

Condensed monolith

The monolith is modelled using a reduced geometry and correspondingly increased resistance tensors, as presented in Section 4.5.1.2. Figure 5.7 shows that this has negligible effect on downstream velocity profile prediction. This is as expected, since the macroscopic pressure losses remain constant, with minimal changes attributed to rounding error. This approach therefore has the advantage of greatly reducing the computational demand of the model.

Since there is negligible difference to the full monolith model, the study is not considered in more detail and results are included for completion. Although similar methods have been applied elsewhere (e.g. high aspect cell ratio by Benjamin and Roberts, (2000)), the method presented in this work is more suitable for application in Star-CCM+.

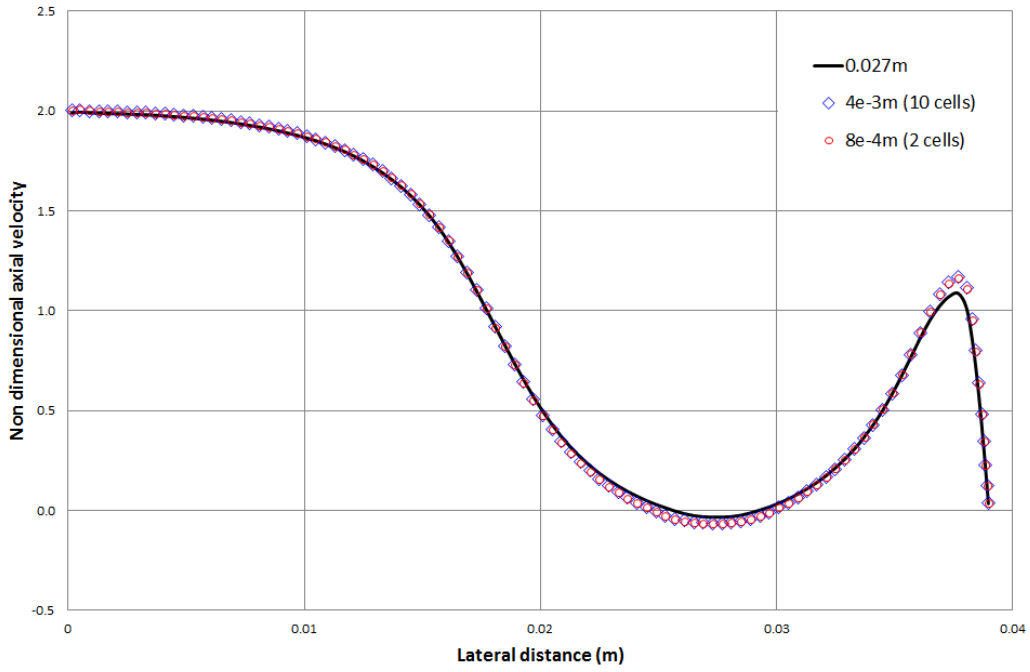

Figure 5.7: Velocity profiles downstream of porous medium with resistance tensors equivalent to 27 mm monolith, Re $= 6.0 \times 10^4$

5.2 Individual Channels Model

Figure 5.8 shows a typical flow field as modelled using the individual channels model presented in Section 4.5.2. The analogous porous medium approach model is given in Figure 5.1.

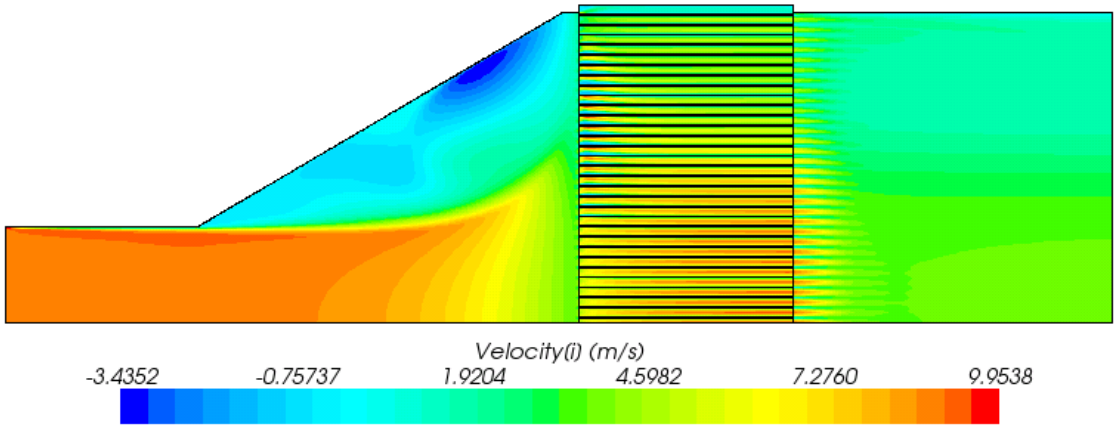

Figure 5.8: Velocity contour plot of individual channels model, $L = 27$ mm, Re $= 2.2 \times 10^4$.

Developing boundary layers are present in the channels and channel flow is asymmetric as a result of the oblique entry of flow into the channels. Small recirculation bubbles are evident at the entrance of channels with highly oblique angle of attack, as demonstrated in Figure 5.9. This shows that the model inherently accounts for restriction of the flow as it enters and traverses the monolith. Jets are present as the flow enters the outlet sleeve. Mixing of the jets is sufficient for a relatively smooth profile 40 mm downstream.

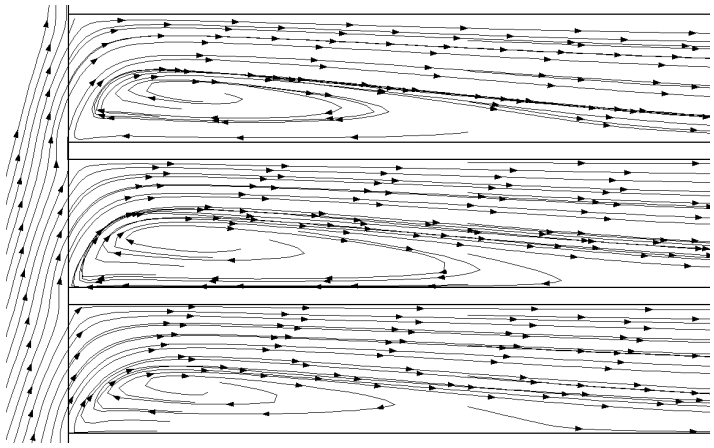

Figure 5.9: Recirculating flow at entrance to channels

Predictions from this model are compared with results when employing the porous medium approach and experimental data. Figure 5.10 presents velocity profiles in the diffuser. Results from the two models are similar, with any differences more evident as flow approaches the monolith and with increased Re. This is as expected, since the different methods for modelling the monolith produce distinct predictions of pressure distribution.

Figure 5.11 compares axial velocity profiles 40 mm downstream of the monolith. HWA velocity profiles 'HWA 1' and 'HWA 2' in Figure 5.11 show measurements either side of the symmetry plane of the system.

The model provides good qualitative description of the flow profile, however omits secondary peaks for the longer monolith (Figure 5.11(f)). Maximum velocities agree well, particularly for the case of low Re and short monolith (Figure 5.11(a)). They are however underpredicted for the majority of cases. The same is also true for secondary maxima at the walls. Underprediction is particularly observed for the longer monolith, where the profile is similar to the porous medium approach with no entrance effect (see Figures 5.11(e)–(h)). For these cases the flow predicted by the individual channels model is too uniform downstream. The individual channels model overestimates the jet width and troughs are located closer to the wall than as measured. This is consistent with discrepancies in axial velocity profile immediately upstream of the monolith (Figure 5.10).

Discrepancies between model predictions and experimental data may arise from assumptions in the model. The geometry for the channels is derived from the manufacturer's specifications, however this assumes uniformity throughout the monolith. In reality, channels are not perfectly square and channel dimensions are not identical across the monolith. Channels are not perfectly straight and the walls are rough and porous.

Nonetheless the model has consistent accuracy across the two monolith lengths and in this regard it represents an improvement on the porous medium models.

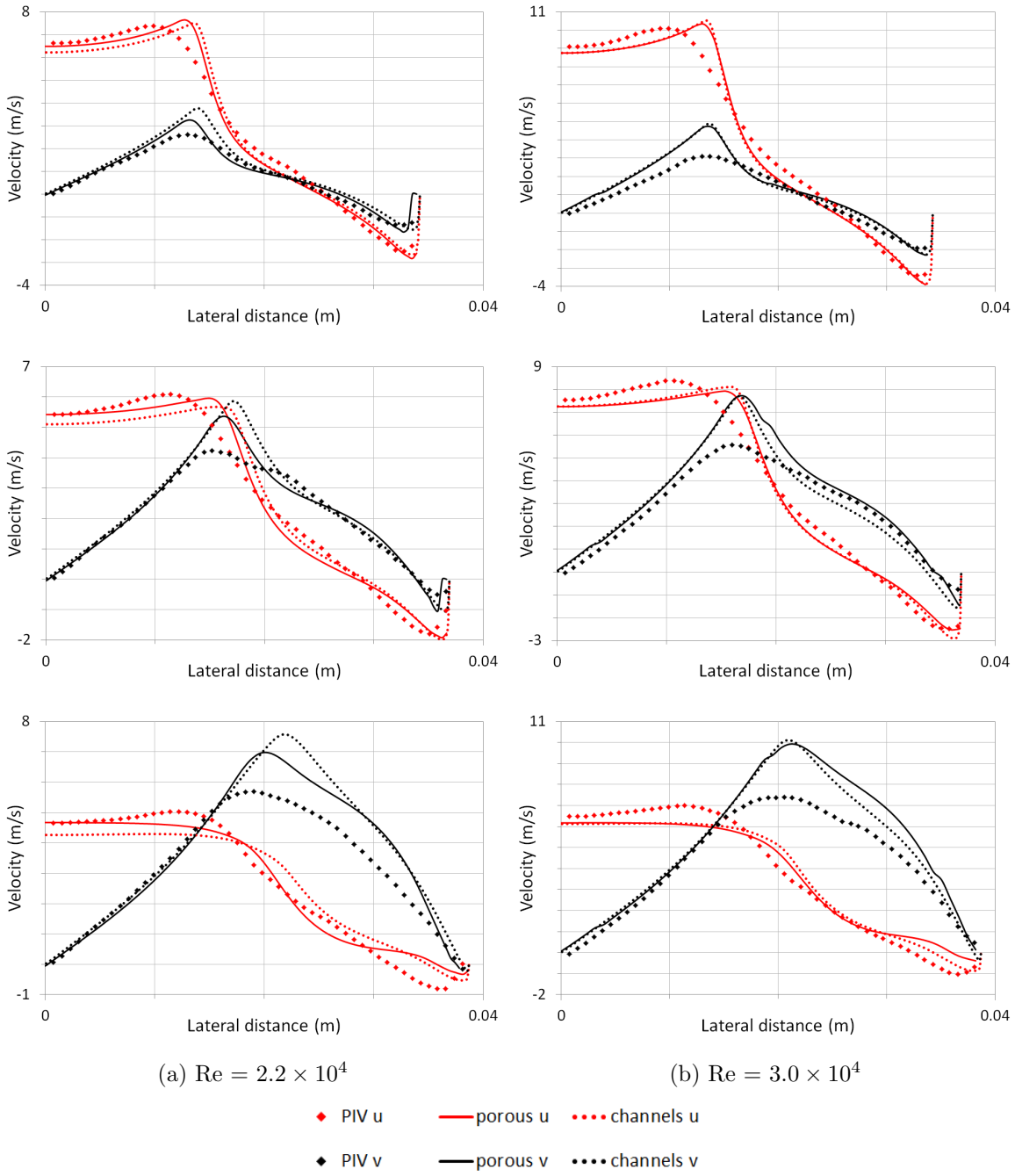

(a) $\mathrm{Re} = 2.2 \times 10^4$ (b) $\mathrm{Re} = 3.0 \times 10^4$

Figure 5.10: Velocity profiles in diffuser 10.13 mm (top), 5.55 mm (centre) and 2.5 mm upstream of 27 mm monolith. u and v respectively denote axial and transverse velocity.

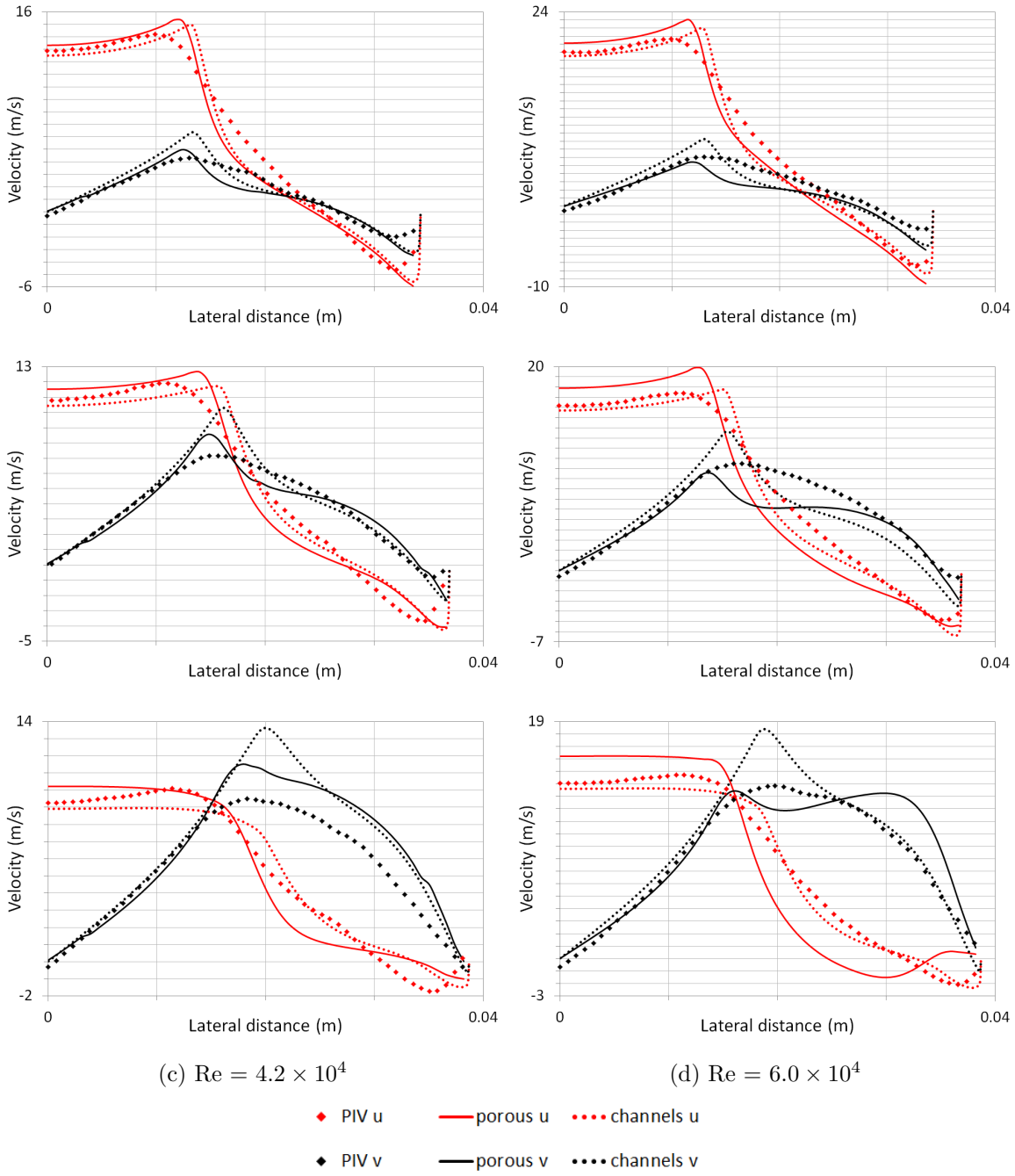

(c) Re $= 4.2 \times 10^4$ (d) Re $= 6.0 \times 10^4$

Figure 5.10: Velocity profiles in diffuser 10.13 mm (top), 5.55 mm (centre) and 2.5 mm upstream of 27 mm monolith. u and v respectively denote axial and transverse velocity. (cont.)

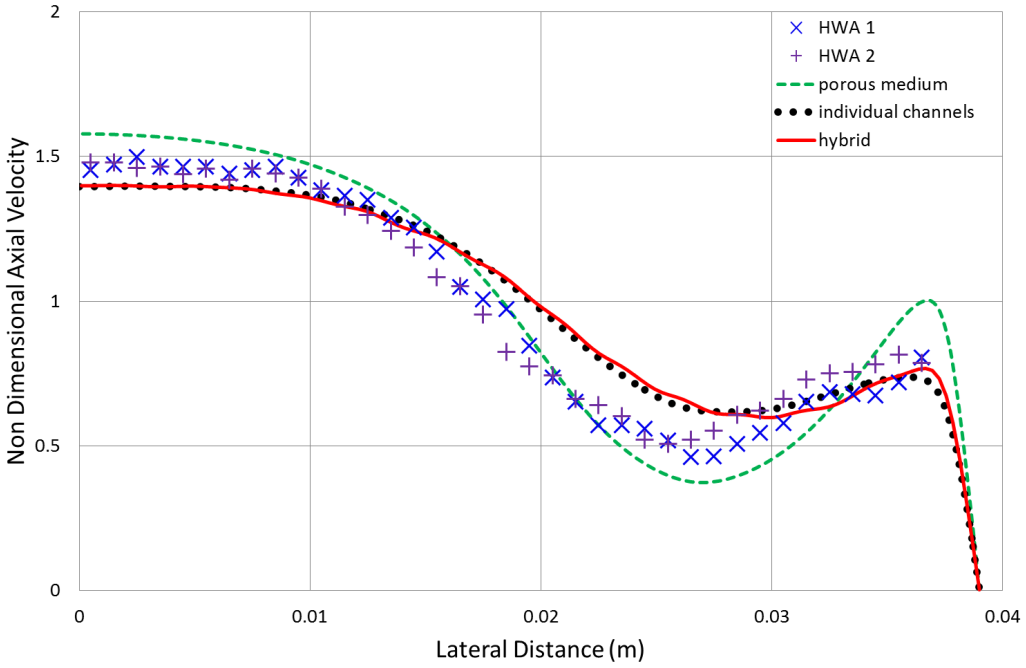

(a) $L = 27$ mm, $\mathrm{Re} = 2.2 \times 10^4$

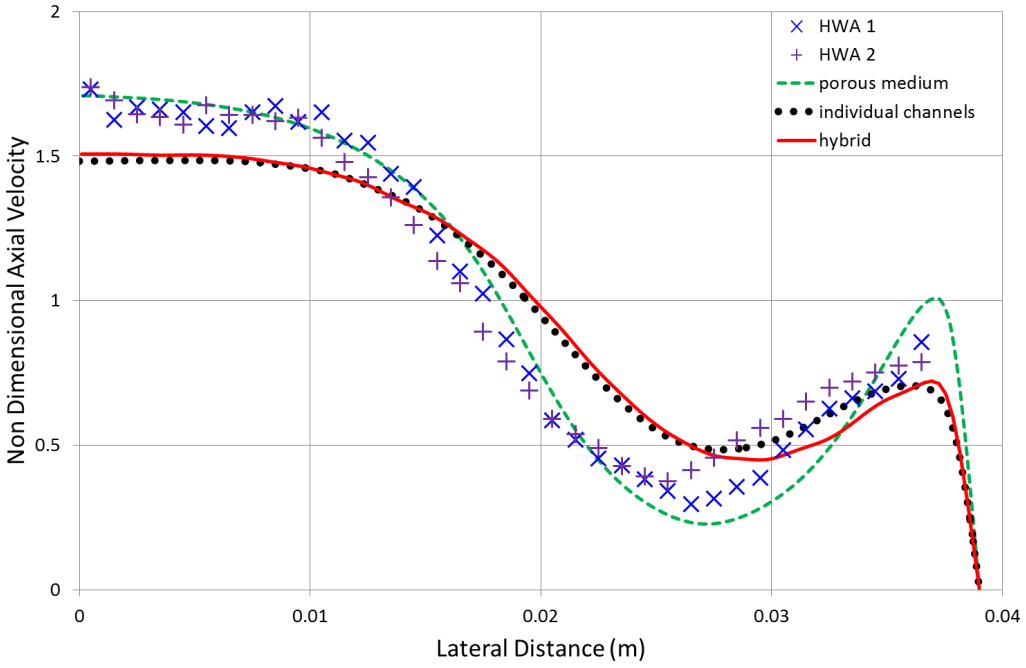

(b) $L = 27$ mm, $\mathrm{Re} = 3.0 \times 10^4$

Figure 5.11: Axial velocity profiles 40 mm downstream of monolith

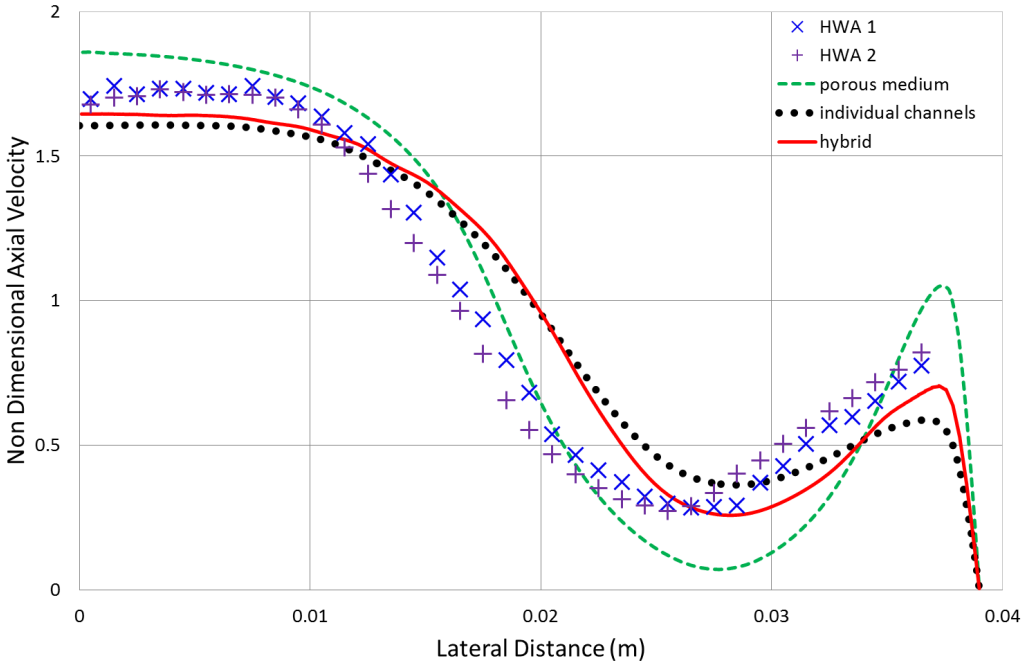

(c) $L = 27$ mm, $\mathrm{Re} = 4.2 \times 10^4$

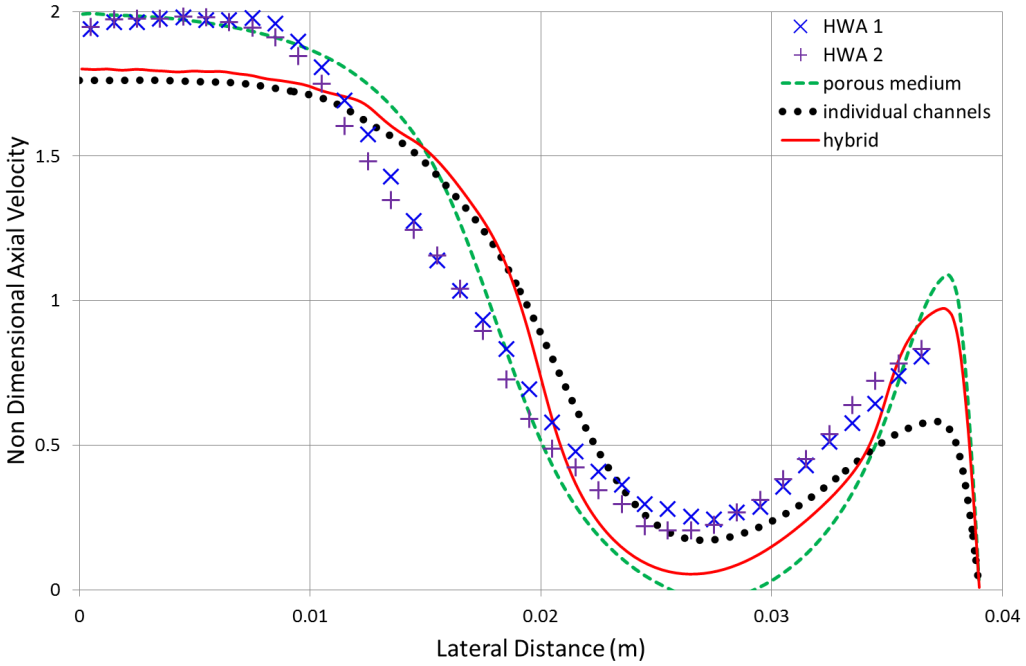

(d) $L = 27$ mm, $\mathrm{Re} = 6.0 \times 10^4$

Figure 5.11: Axial velocity profiles 40 mm downstream of monolith (cont.)

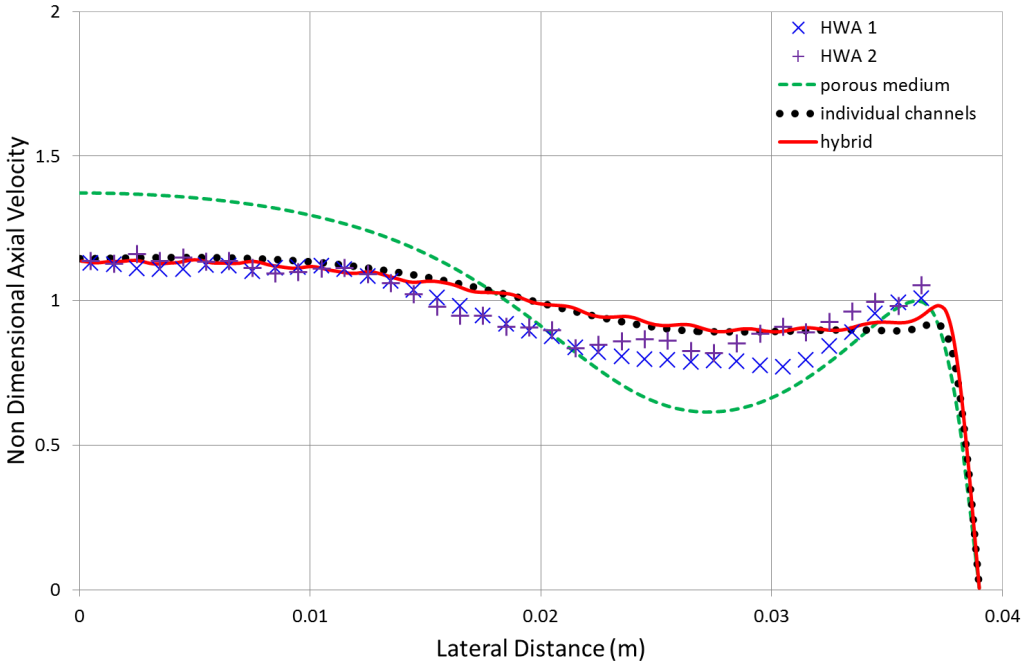

(e) $L = 100$ mm, $\mathrm{Re} = 2.2 \times 10^4$

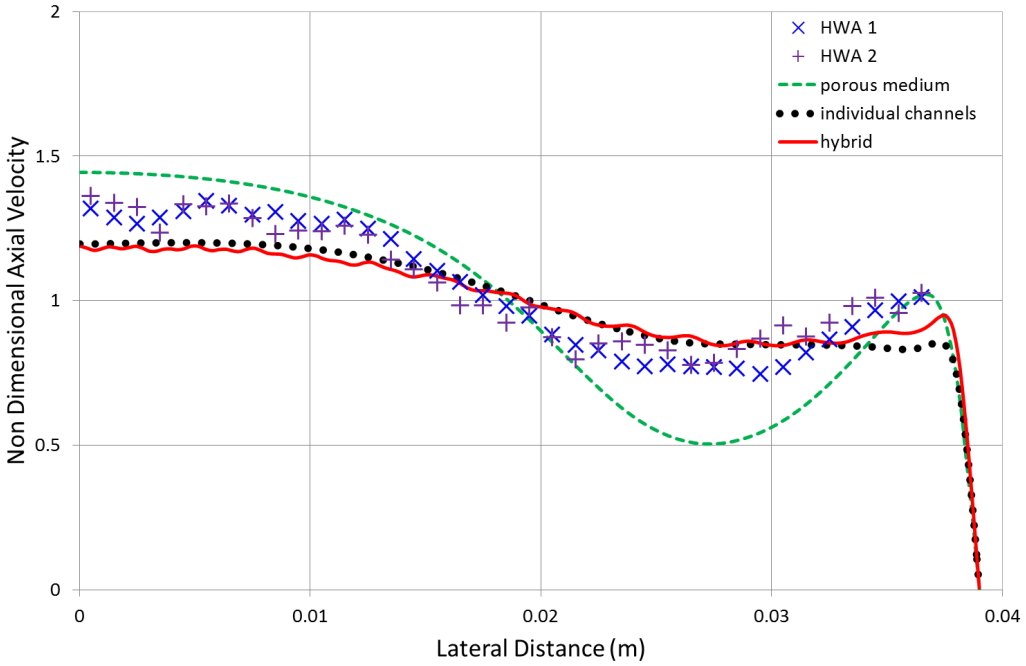

(f) $L = 100$ mm, $\mathrm{Re} = 3.0 \times 10^4$

Figure 5.11: Axial velocity profiles 40 mm downstream of monolith (cont.)

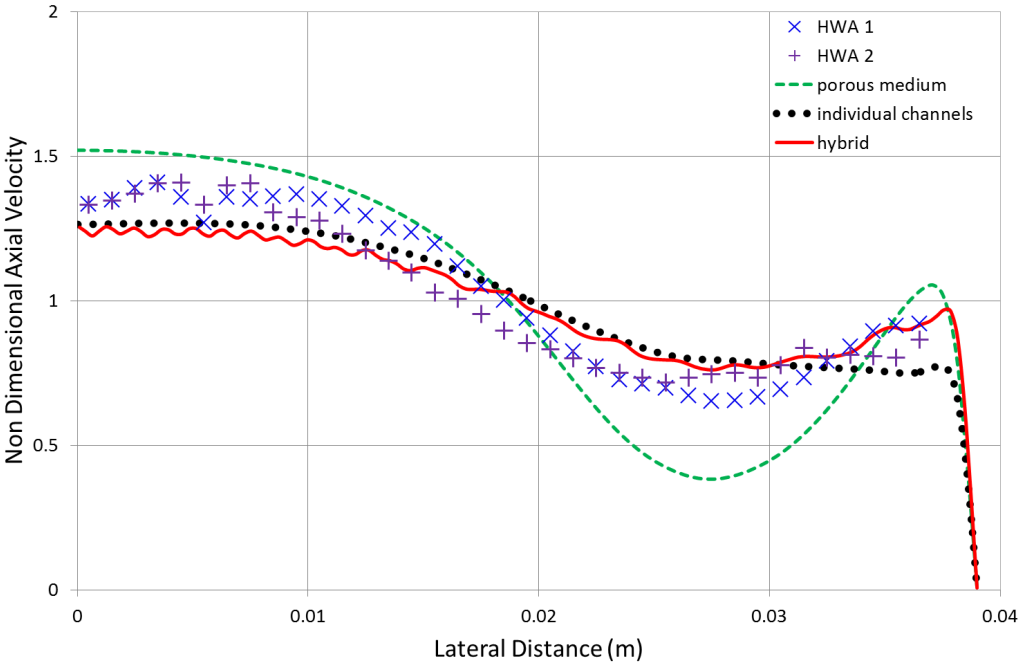

(g) $L = 100$ mm, $\mathrm{Re} = 4.2 \times 10^4$

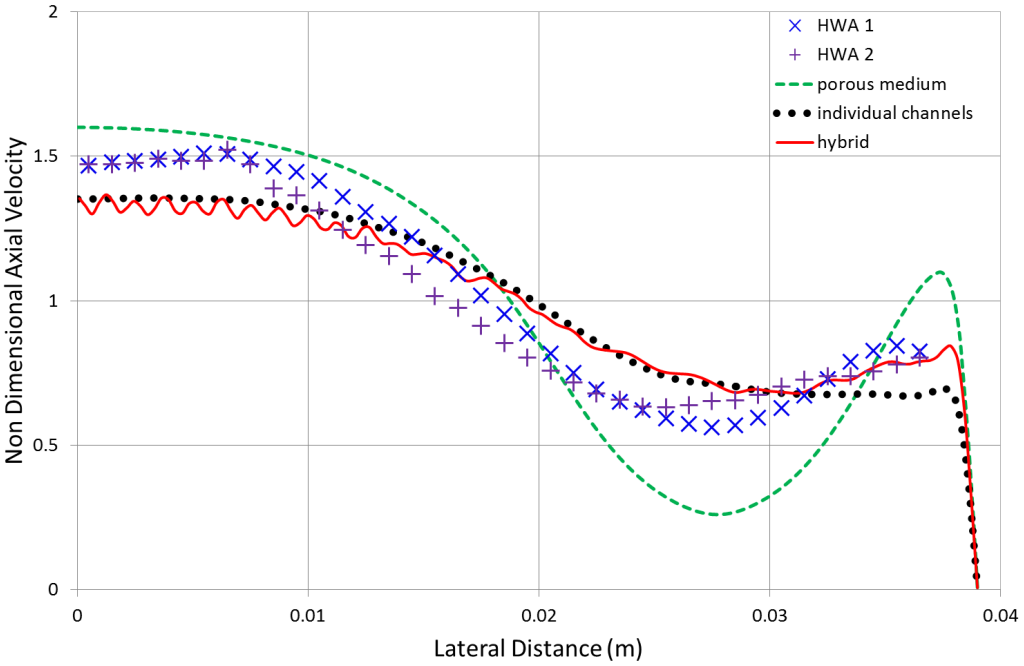

(h) $L = 100$ mm, $\mathrm{Re} = 6.1 \times 10^4$

Figure 5.11: Axial velocity profiles 40 mm downstream of monolith (cont.)

Wide Outlet Sleeve

The application of the individual channels model to the wide sleeve system is compared to results from the porous medium model. Figure 5.12 compares axial velocity profiles 40 mm downstream of the monolith exit. Velocities are normalised by the mean outlet velocity U_{out}. Since the 69° critical angle model has been shown to provide the best results using the porous medium approach, only the prediction from this model is presented for comparison.

The individual channels model provides improvement compared to the predictions from the porous medium simulations. The total width of the profile is in better agreement, however the central jet is slightly wider than experimental measurements. Velocity values at maxima and minima are in good agreement.

The improvement presented by the individual channels model may be attributed to an accurate description of flow behaviour upon entrance to the monolith channels. The presence of boundary layers at the channel walls produces individual jets in the outlet sleeve, preserving the flow profile from the monolith and thus better predicting the profile downstream.

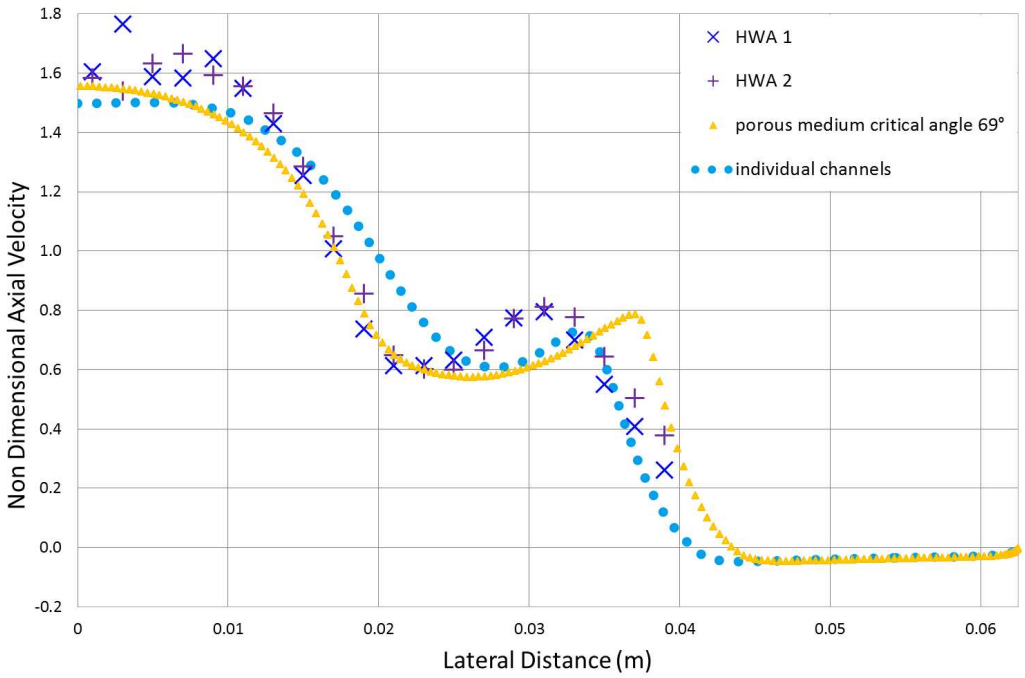

Figure 5.12: Velocity profiles downstream of individual channels model with wide outlet sleeve. $L =$ 27 mm, Re $= 3.0 \times 10^4$.

5.3 Hybrid Model

As presented in Section 4.5.3, a novel hybrid modelling approach has been developed and tested for the same configurations as for the porous medium approach and individual channels models (Porter et al., In press).

The computational demand of a model may be demonstrated by the number of cells required for a mesh independent solution. Table 5.1 compares the computational mesh of models using the porous medium, individual channel, and hybrid approaches. Compared to the individual channels model, the novel hybrid model greatly reduces the number of cells required and has the benefit of being independent of monolith length.

Table 5.1: Computational resources required for different monolith modelling approaches

Model	Monolith length (mm)	
	27	100
Porous medium	2.8×10^4	4.7×10^4
Individual channels	4.0×10^6	8.8×10^6
Hybrid	9.1×10^5	9.1×10^5

Figure 5.13 shows velocity contours on the symmetry plane of the model for the case of a 27 mm monolith with $\mathrm{Re} = 4.2 \times 10^4$. At the expansion of the diffuser, flow separates and a jet traverses the diffuser. The resistance presented by the channels forces the flow to spread radially upstream of the monolith face. Flow enters the channels obliquely away from the diffuser centre, causing recirculation bubbles to form at the inlet of the individual channels as seen previously (Figure 5.9). As the flow progresses along the channel, a boundary layer develops and the velocity profile becomes increasingly parabolic. The porous region results in a high resistance to the flow in the axial direction. Individual jets from the channels are present at the monolith outlet, and are less visible as more spreading occurs downstream, resulting in a relatively smooth velocity profile at the outlet.

Flow distribution in the catalyst is largely dependent on the behaviour of the flow at the monolith face. Accurate predictions in this critical region are therefore highly important. Figure 5.14 compares velocities in the diffuser, 2.5 mm upstream of the monolith, with PIV experimental measurements (Mat Yamin, 2012) and with predictions from the porous medium and individual channels models. At such close proximity to the monolith, the method of modelling the monolith resistance affects the upstream velocity. Predictions from the hybrid model fall between those from the two separate

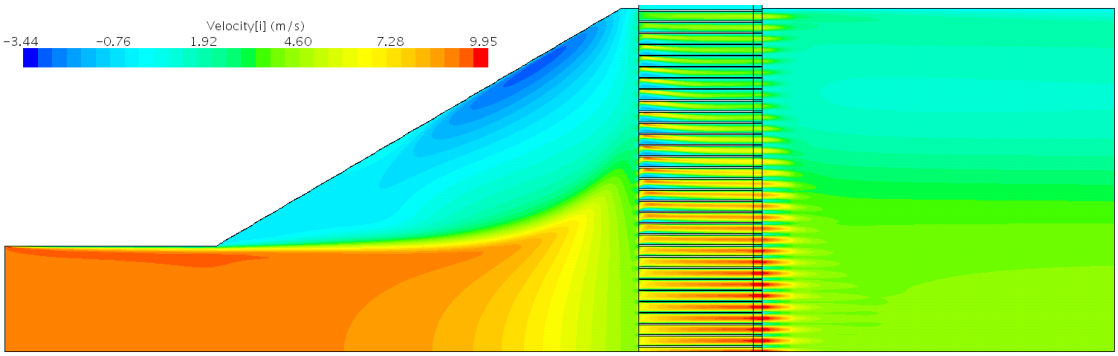

Figure 5.13: 27 mm monolith, Re = 2.2×10^4

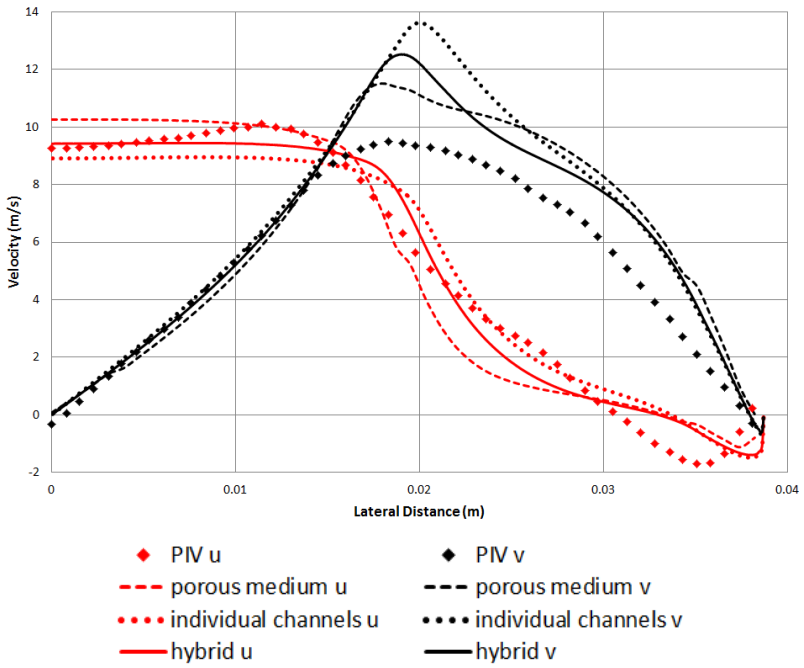

Figure 5.14: Velocity 2.5 mm upstream of 27 mm monolith, Re = 4.2×10^4

approaches. Axial velocity plots show a slight over-prediction of the central jet width and transverse velocity shows over-predicted obliqueness outside of the central region, corresponding to a high level of shear at the edge of the spreading core.

Predictions downstream of the monolith are presented in Figure 5.11. Results from the hybrid model fall between those from the individual channels and porous model. Profiles have high similarity to the individual channels model, demonstrating the importance of accurately capturing flow behaviour at the entry to the monolith. However, the hybrid modelling approach has the advantage of reducing computational time compared to the individual channels model.

The effect of combining the individual channels model with a porous section is most visible near to the sleeve wall. Flow maldistribution is increased compared to the individual channels model. Particularly present for the short monolith higher Re case shown in Figure 5.11(c),(d), maxima at the centre and near the wall are higher and velocity at the trough is lower, showing improved agreement with experimental data.

Profile predictions for the longer monolith are fairly uniform, with the hybrid model showing improvement compared to the individual channels model near to the wall. Profiles are noticeably unsmooth, with the jet from each channel remaining identifiable downstream, particularly for the high Re cases (Figure 5.11(g),(h)). This is not observed for the individual channels model, and it is therefore suggested that this is due to the method used for calculating the pressure drop across the porous section.

Discrepancies between hybrid model predictions and experimental data may be attributed to assumptions in the model. The geometry of the channels assumes cell uniformity and channels walls are treated as flat surfaces. In the porous region, an uncertainty arises from the application of the theoretical Hagen-Poiseuille equation.

Wide Outlet Sleeve

In the contour plot shown in Figure 5.15, jets are visible in the outlet sleeve. Figure 5.16 presents the predicted downstream axial velocity profile. The individual jets are preserved and the width of the flow profile is in good agreement with experimental data. Compared to the porous medium model, the hybrid model benefits from the inclusion of channels at the monolith entrance in this regard.

Increased maximum velocity compared to the individual channels model is consistent with the difference in velocity immediately upstream of the monolith, shown in Figure 5.14. In turn, the upstream flow profile is affected by the monolith modelling approach applied downstream.

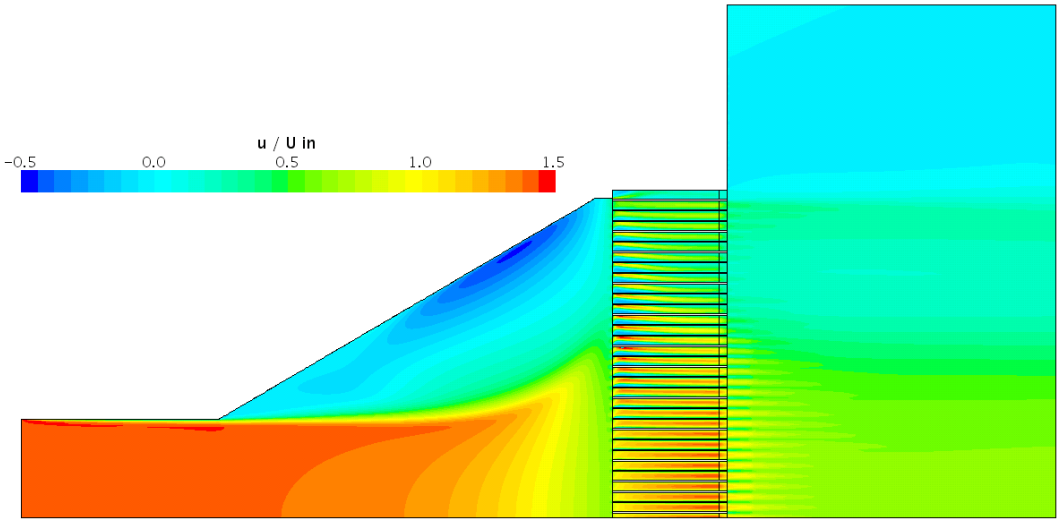

Figure 5.15: Axial velocity prediction for hybrid model with wide outlet sleeve.
$L = 27$ mm, $\mathrm{Re} = 3.0 \times 10^4$.

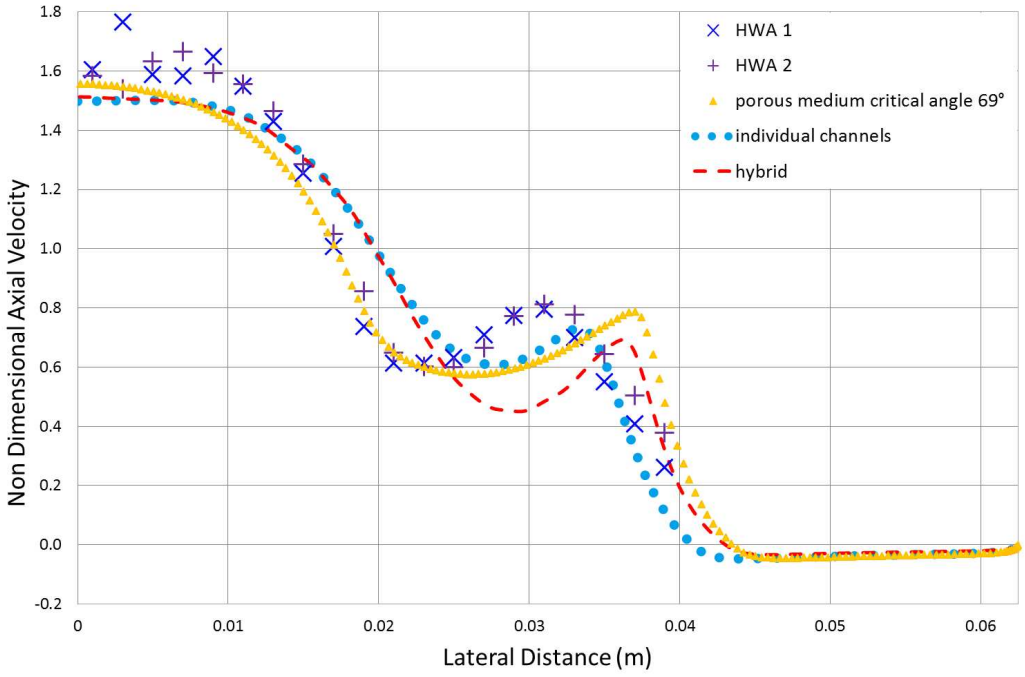

Figure 5.16: Velocity profiles downstream of hybrid model with wide outlet sleeve.
$L = 27$ mm, $\mathrm{Re} = 3.0 \times 10^4$.

5.4 Non Uniformity Index

The level of flow maldistribution is a key factor in the design process of catalytic converters and is commonly used in the automotive industry. A relatively simple measure of conversion efficiency can then be obtained for post light-off conditions where reactions are mass-transfer limited (Karvounis and Assanis, 1993; Benjamin et al., 2004; Jeong and Kim, 2001). Conversion efficiency η as a function of flow velocity can then be described by Equation 5.1 (Benjamin et al., 2004):

$$\eta = 1 - \exp\left(\frac{-4Lk_c}{u_c d_h}\right) \tag{5.1}$$

where L is the length of the monolith channel, u_c is the channel velocity, d_h is the channel hydraulic diameter, and k_c is the mass transfer coefficient which may be determined theoretically (Bhattacharya et al., 2004).

Figure 5.17 compares the non-uniformity index ψ from the model predictions and the experimental data. The non-uniformity index is defined as

$$\xi = \frac{\zeta}{U} \tag{5.2}$$

and is calculated using the mass flow weighted velocity over the monolith face. ζ is defined as

$$\zeta = \frac{1}{\dot{m}} \int_A |u_i - U| \, \delta\dot{m} \tag{5.3}$$

which is equivalent to

$$\zeta = \frac{1}{n} \sum_{i=1}^{n} |u_i - U| \, u_i \tag{5.4}$$

for a velocity profile of discrete data, where u_i and U respectively denote the local axial velocity and the mean axial velocity. Non-uniformity values of experimental data are approximately equidistant to the predicted values from CFD for the shorter monolith. However for the longer monolith case, the porous medium model performs markedly worse in the prediction of flow maldistribution than the other models. Figure 5.17 shows simulations exhibiting the same trend as experiment, with the maldistribution index increasing with Re and as monolith resistance is reduced. This is consistent with studies for axisymmetric assemblies, e.g. Benjamin et al., (1996). For the important case where maldistribution is greatest, $\mathrm{Re} = 6.0 \times 10^4$ and 27 mm monolith, it is encouraging to note that hybrid model predictions are within 10% of experiment.

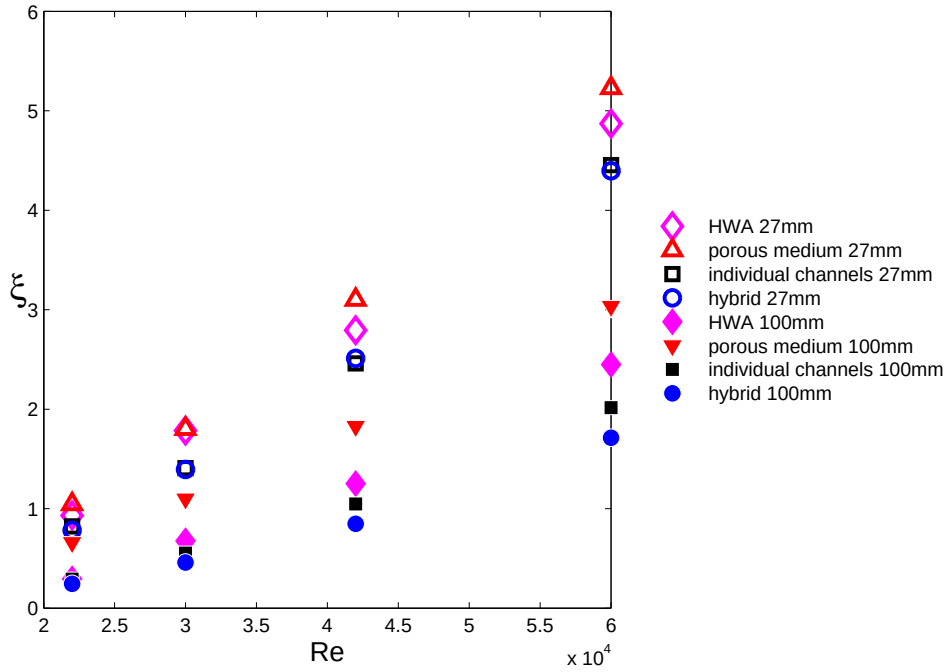

Figure 5.17: Non-uniformity index

5.5 Pressure

The pressure drop across the monolith affects the performance of the engine and fuel efficiency. It is therefore important to be able to accurately predict the change in pressure across the catalyst system. CFD predictions of pressure distribution are presented here. Figure 5.18 shows symmetry plane contour plots from different modelling approaches for the same steady flow case.

The first porous medium model presented in this work only calculates the pressure drop due to unidirectional flow in the monolith channels. The axial pressure drop is based on the superficial velocity at the first cell of the monolith inlet, with porous resistance coefficients derived via experimental measurement (Eq. 4.7). The additional pressure loss $\Delta P = \rho v^2/2$ accounts for oblique entry into the channels. The monolith section in Figure 5.18(a) shows the effect of the specified pressure drop function. Particularly high pressure is seen at the centre of the front face of the monolith, where flow is normal to the porous region.

In contrast, the pressure drop predicted across the monolith using the individual channels model is due entirely to the geometry of the monolith channels and the characteristics of the fluid. Figure 5.18(b) shows the pressure increase at areas of oblique flow entering the channels, and the negative pressure present in the outlet sleeve.

The hybrid model, shown in Figure 5.18(c), combines the two: pressure losses at the most upstream part of the monolith, across the channels section, are derived by the model itself, whereas the porous region downstream uses resistance tensor coefficients, here derived using the Hagen-Poiseuille formulation, to account for the pressure loss of fully-developed flow along a rectangular duct.

Comparing the models, the similarity of pressure distribution shown by the individual channels and hybrid models supports the use of the truncated porous section of the hybrid model to represent the downstream channel flow of the monolith. Comparatively higher pressures present in the diffuser of the porous medium model illustrate the effects of applying theoretical pressure drop calculations to the system.

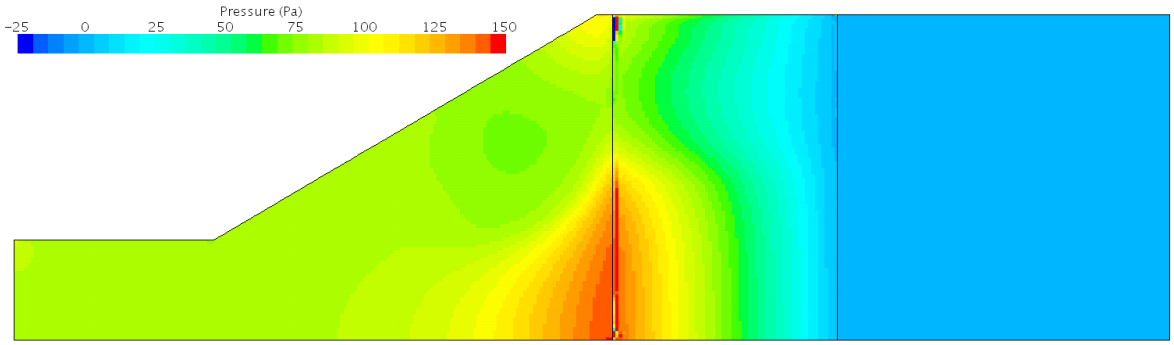

(a) Porous medium model

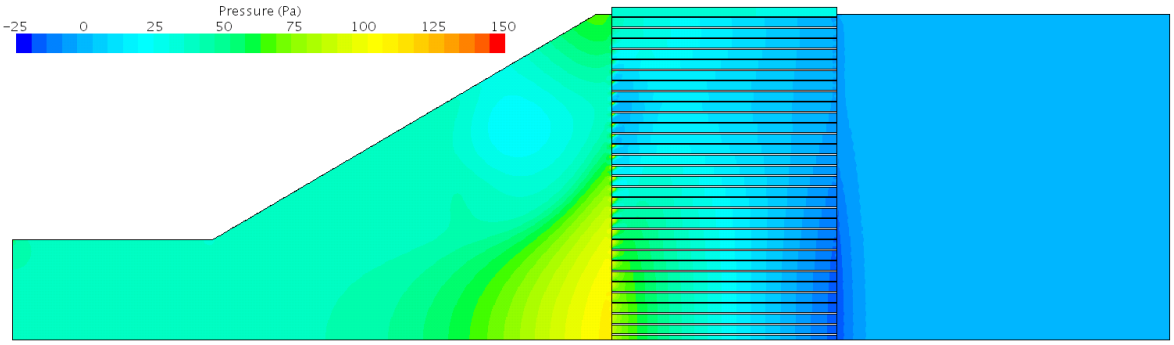

(b) Individual channels model

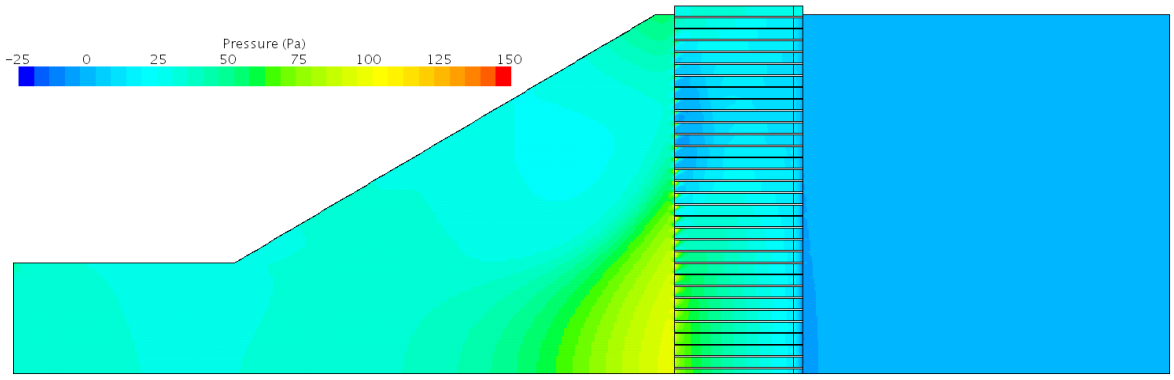

(c) Hybrid model

Figure 5.18: Pressure contour plots of CFD models. $L = 27$ mm, $\mathrm{Re} = 3.0 \times 10^4$.

6 | Pulsating Flow

Results are presented and discussed for the pulsating flow study. The model is presented in Section 4.6 and case numbers and relavant flow parameters are specified in Table 3.2. CFD predictions are initially compared to phase-averaged PIV data, which leads to the consideration of instantaneous flow fields. The results discussed in this chapter have been presented at an international conference (Porter et al., 2015) and have also contributed to the study by Saul et al., (2015).

6.1 Phase-Averaged Flow Fields

Flow fields in the diffuser from PIV and CFD are compared at regular non-dimensional times throughout the pulse cycle. PIV data is averaged from 100 individual cycles. Figures 6.1–6.3 show velocity vector fields, where velocities are normalised by the cycle-averaged mean inlet velocity. For Case 1, velocities are further examined via comparison of cross-sectional profiles upstream of the monolith in Figure 6.5. Figures 6.6–6.8 show vorticity contours in the diffuser. The non-dimensional unit $\omega L/U$ denotes the normalisation of the vorticity magnitude by the diffuser length and the cycle-averaged mean inlet velocity.

Peak inlet velocities occur in the range $t/T = 0.6$–0.7. At this phase of the cycle, a central jet traverses the diffuser and there is separation of the flow from the wall. The jet spreads immediately upstream of the monolith face. Flow either enters the monolith or forms large recirculating regions either side of the jet. The shear layer is then incorporated into the recirculation region. At time $t/T = 0.8$, the flow field is similar to the steady state case (Mat Yamin et al., 2013). During inlet flow deceleration ($t/T = 0.7$–1.0) the recirculation regions dominate the diffuser and the central jet width is narrowed as a result of pulsation (Medina et al., 2013).

Vorticity decreases and dissipates within the diffuser. When not fully dissipated during the cycle, recirculating flow remains in the diffuser and is denoted *residual vorticity*. Acceleration of the inlet flow ($t/T = 0.1$–0.5) sees the residual vortices of the previous cycle carried along the length of the diffuser. Flow is able to reattach to the diffuser wall downstream of the small recirculation region, resulting in a relatively uniform velocity profile upon exit from the diffuser.

Comparing experimental and numerical results, best qualitative agreement is observed mid-cycle, for $t/T = 0.4$–0.8. PIV shows high variation of the jet core width, and it noticeably narrows at $t/T = 0.1$ compared to the rest of the cycle. For high inlet velocities, PIV data show more diffusion of

the jet, with the shear layer wider than for CFD. There is significant difference in vortex structure at time-steps $t/T = 0.1$–0.3, where residual vorticity is negligible for PIV data. The retention of vorticity by CFD suggests an underestimation of vortex dissipation.

Figure 6.5 compares velocity profiles in the diffuser for the case with Re $= 2.2 \times 10^4$, $f = 50$ Hz. Axial and transverse components, normalised by the mean inlet velocity, are presented from four cross-sections in the diffuser. The locations shown are 2.5, 5.3, 10.6 and 20.5 mm upstream of the diffuser outlet, as illustrated in Figure 6.4. Consistent with velocity contour plots (Figures 6.1–6.3), best agreement of profiles is observed at the time of maximum inlet velocity ($t/T = 0.6$–0.7), with moderate agreement during the deceleration period ($t/T = 0.8$–1.0). During inlet velocity acceleration, highly over-predicted CFD velocities demonstrate the contrast in residual vorticity from the previous cycle.

Figures 6.6–6.8 show vorticity distribution in the diffuser. CFD results show peak vorticity magnitudes at vortex centres and within the jet shear layer. Maximum PIV vorticity magnitudes are low in comparison throughout the cycle. For example, at $t/T = 0.7$ the predicted vorticity at the centre of the vortex is twice as high as PIV measurements.

Vortex centres are identifiable for the majority of time-steps presented. CFD and PIV data are further studied via comparison of the vortex core location at each time-step. For simplicity, the location of the data point with highest vorticity magnitude in the region of interest is considered. CFD predictions exhibit high levels at vorticity at the separation point and at near-wall regions. Maxima located in these regions are therefore ignored for the purpose of this analysis, such that the point identified denotes the centre of the dominant vortex in the main body of the diffuser. Figure 6.9 presents the location of local vorticity maxima for the three cases studied. Data labels T1 to T10 denote the time-steps $t/T = 0.1$ to 1.0 respectively. Where residual vorticity is present and two vortex centres are distinguishable, both locations are determined and the respective data label is repeated, giving a representation of the overall path of each vortex structure.

Regarding CFD predictions, the two cases with identical $J = 3.4$, shown in Figures 6.9(a) and 6.9(c), show the vortex structure following a well-defined path. The paths also have a similar shape, as illustrated in Figure 6.9(d). This demonstrates the suitability of flow regime characterisation by the ratio J, as found by Mat Yamin, (2012). The case of $J = 6.8$, shown in Figure 6.9(b), shows a clear path at the beginning of separation of the vortex from the wall. High residual vorticity later in the cycle sees the vortex remaining in the same region with slight movement, and the locations of vorticity maxima are clustered.

Vorticity contour plots of averaged PIV measurements in Figures 6.6–6.8 show the same qualitative

trend in the cyclic behaviour of vortex structures. However, the path of the traced vortex centre point is not smooth, and sometimes the vortex seems to move backwards against the direction of the flow. Nonetheless a certain level of order in traced vortex movement is observed for all three cases. For example, Figure 6.9(c) shows PIV data split into three regions. Each cluster is associated with a segment of the cycle, namely $t/T = 0.1$–0.4, $t/T = 0.3$–0.5, and $t/T = 0.6$–1.0. Moreover, the trajectory of residual vorticity across time-steps $t/T = 0.1$–0.4 shows sequential behaviour.

The $J = 6.8$ case presented in Figure 6.9(b) shows a clear path directly after separation from the diffuser wall, $t/T = 0.2$–0.5, and clustered locations later in the cycle. In this respect, the experimental data and the model predictions are in good agreement.

The lack of order in the PIV data of Figure 6.9(a) is consistent with the low vorticity presented by PIV in Figures 6.6–6.8. Vorticity levels are particularly weak at times when inlet velocity approaches a minimum ($t/T = 1.0$, 0.1–0.3) and no clear vortex structure is identifiable. The local maximum therefore has no real significance for this data set and a statistical definition of vortex location would be more appropriate.

The disagreement between CFD and PIV may be explained by one or more of the following. Firstly, it is possible that the computational model does not accurately predict the turbulent characteristics of the flow. Turbulence modelling is a complex field with many variables and no one model to suit all flows. Another reason for the difference in values is the level of data resolution. The computational model is more refined than the PIV data set. It is possible that the interrogation window used for PIV measurements was too large to capture high velocity gradients.

Finally, it must be noted that the post-processed PIV data have been phase-averaged from multiple cycles. Any variation in vortex location between cycles would then result in the absence of higher vorticity magnitudes once all fields have been averaged. Section 6.2 presents analysis of instantaneous data fields to determine the presence of cycle-to-cycle variation.

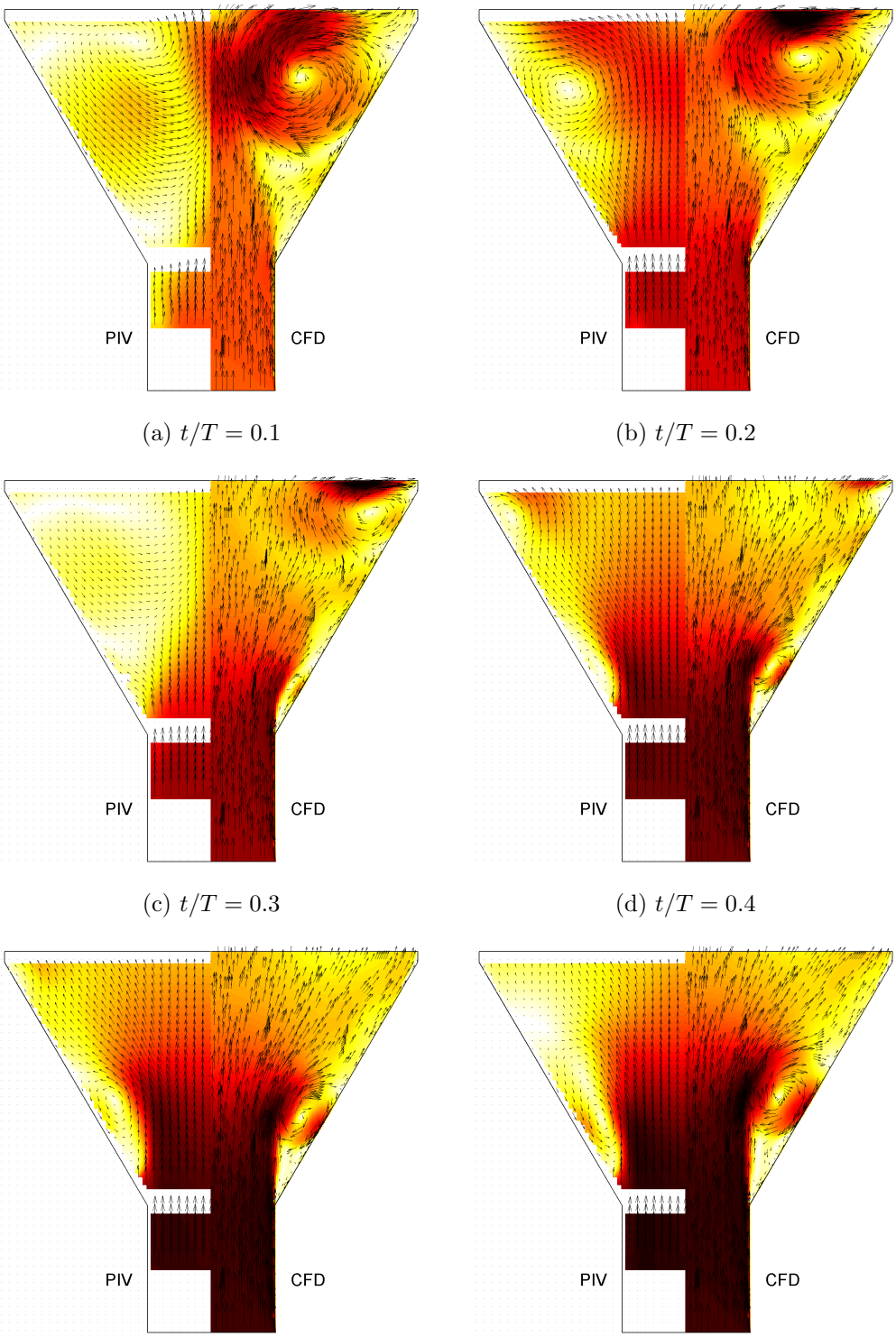

(a) $t/T = 0.1$ (b) $t/T = 0.2$

(c) $t/T = 0.3$ (d) $t/T = 0.4$

(e) $t/T = 0.5$ (f) $t/T = 0.6$

Figure 6.1: Velocity vector fields for Case 1 ($\mathrm{Re} = 2.2 \times 10^4$, $f = 50$ Hz, $J = 3.4$)

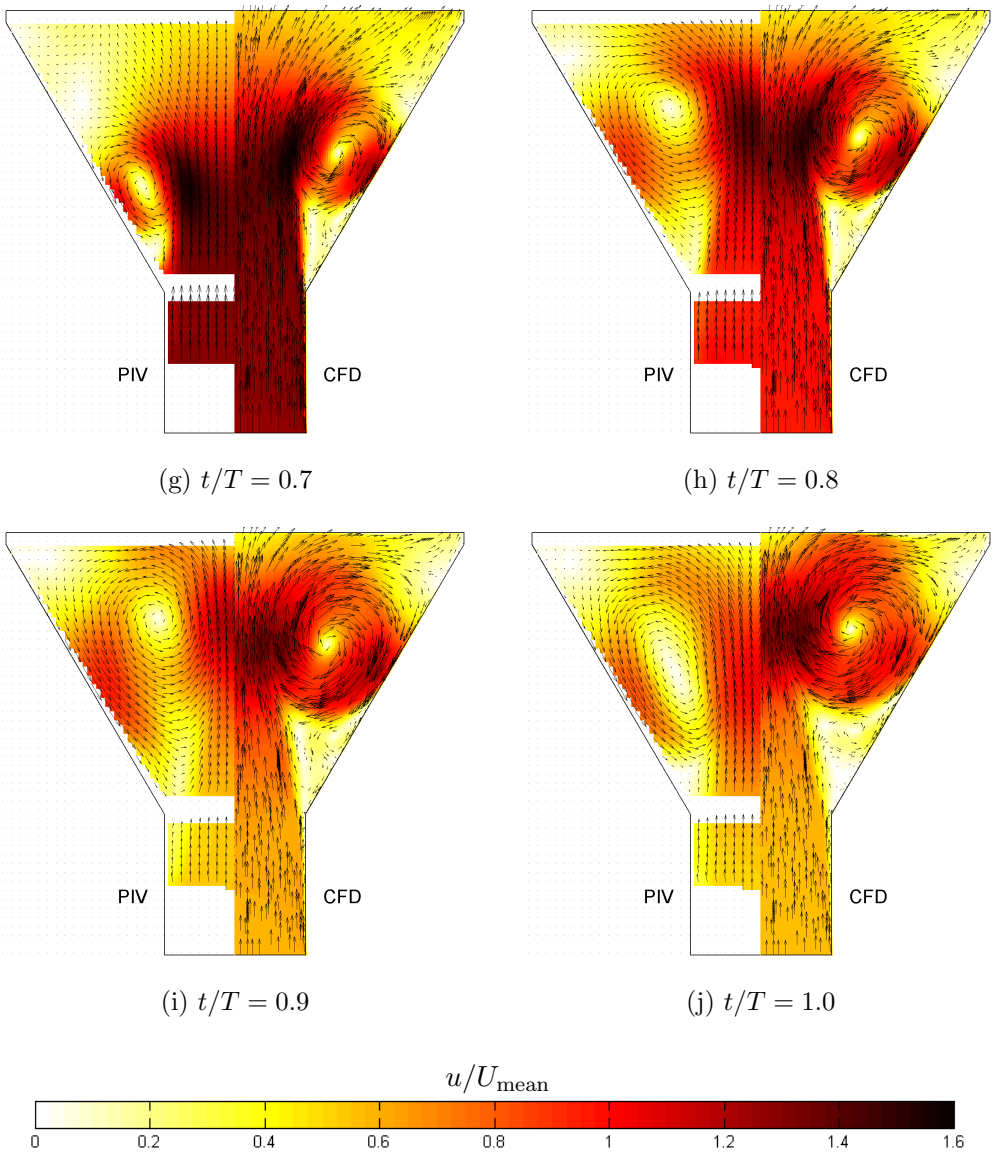

(g) $t/T = 0.7$ (h) $t/T = 0.8$

(i) $t/T = 0.9$ (j) $t/T = 1.0$

Figure 6.1: Velocity vector fields for Case 1 ($\text{Re} = 2.2 \times 10^4$, $f = 50$ Hz, $J = 3.4$) (cont.)

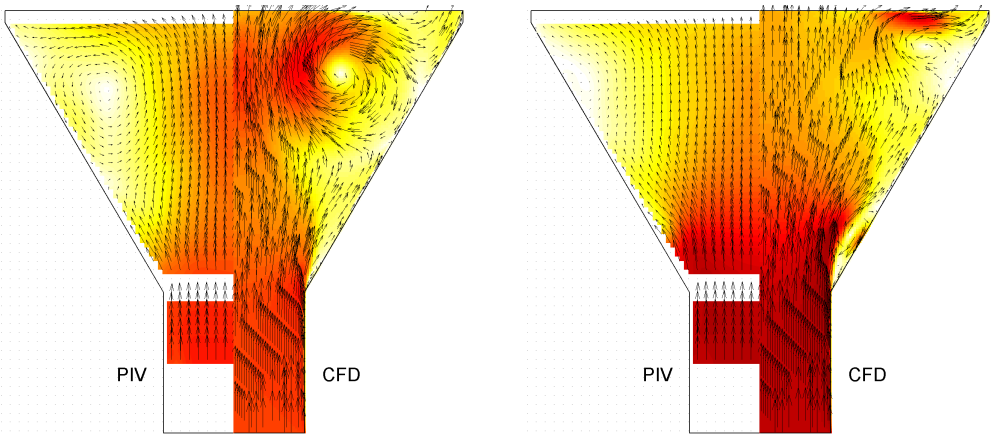

(a) $t/T = 0.1$ (b) $t/T = 0.2$

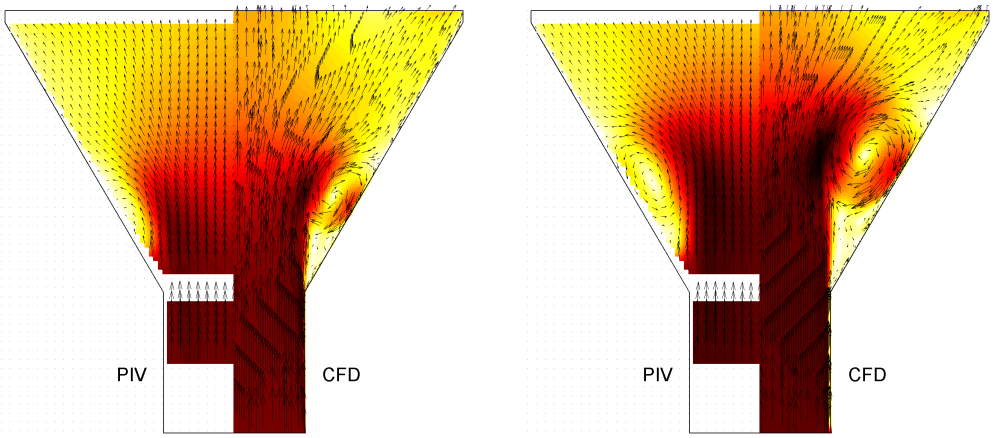

(c) $t/T = 0.3$ (d) $t/T = 0.4$

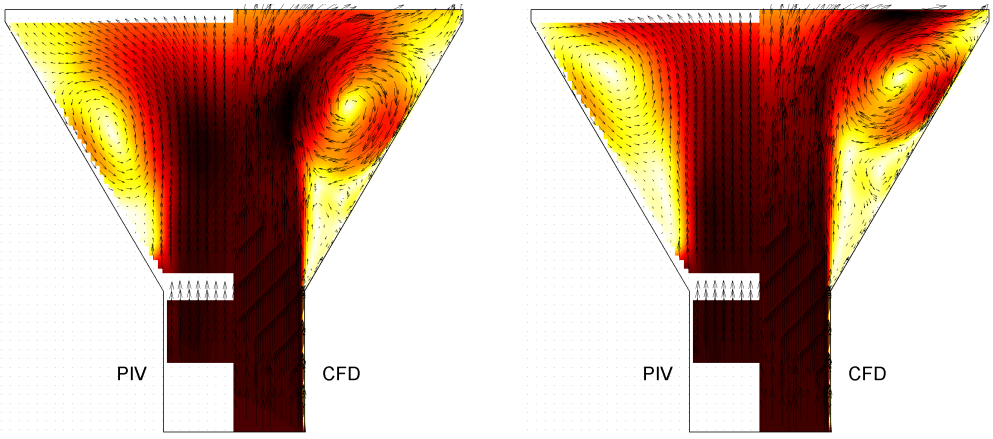

(e) $t/T = 0.5$ (f) $t/T = 0.6$

Figure 6.2: Velocity vector fields for Case 2 ($\mathrm{Re} = 4.2 \times 10^4$, $f = 50$ Hz, $J = 6.8$)

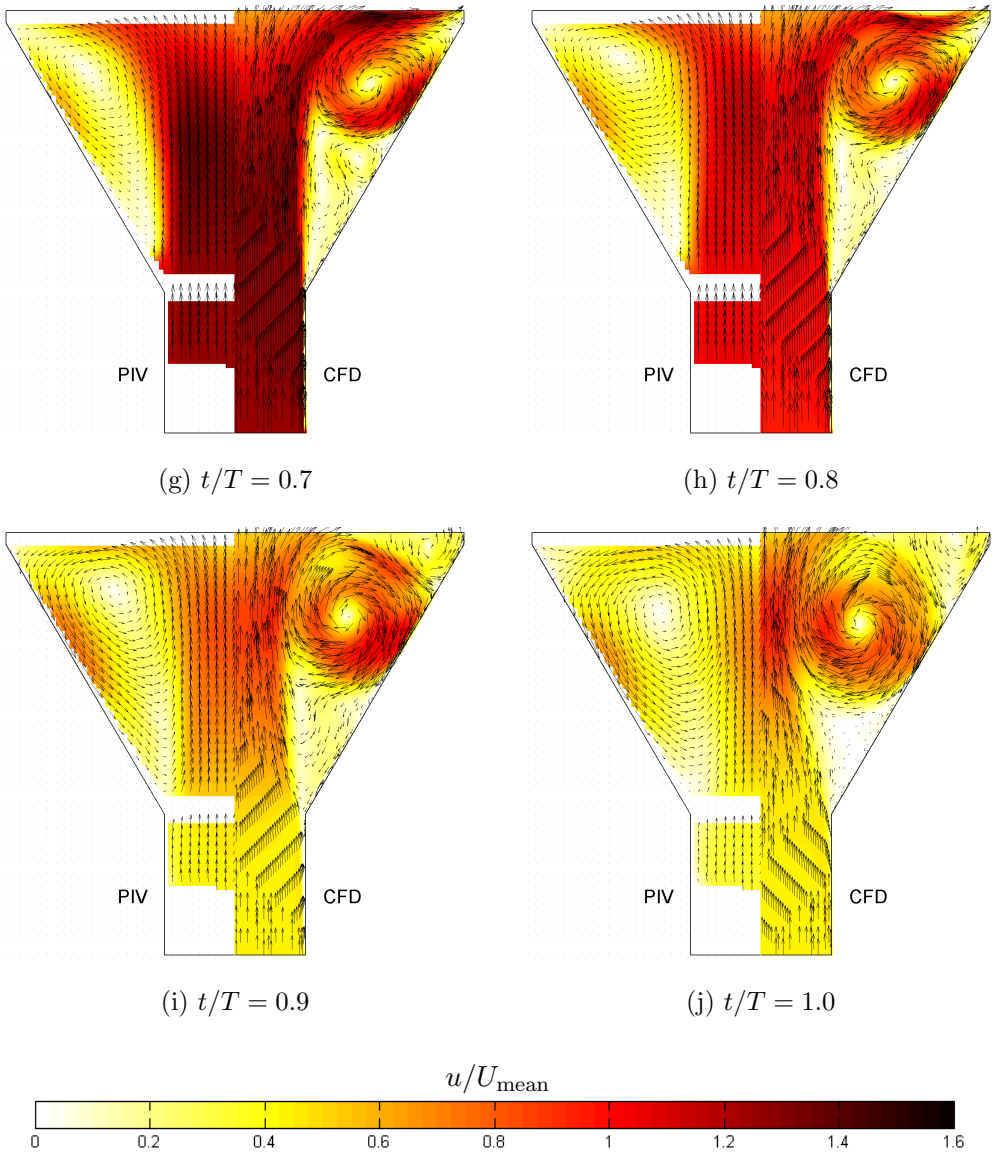

(g) $t/T = 0.7$ (h) $t/T = 0.8$

(i) $t/T = 0.9$ (j) $t/T = 1.0$

Figure 6.2: Velocity vector fields for Case 2 ($\text{Re} = 4.2 \times 10^4$, $f = 50$ Hz, $J = 6.8$) (cont.)

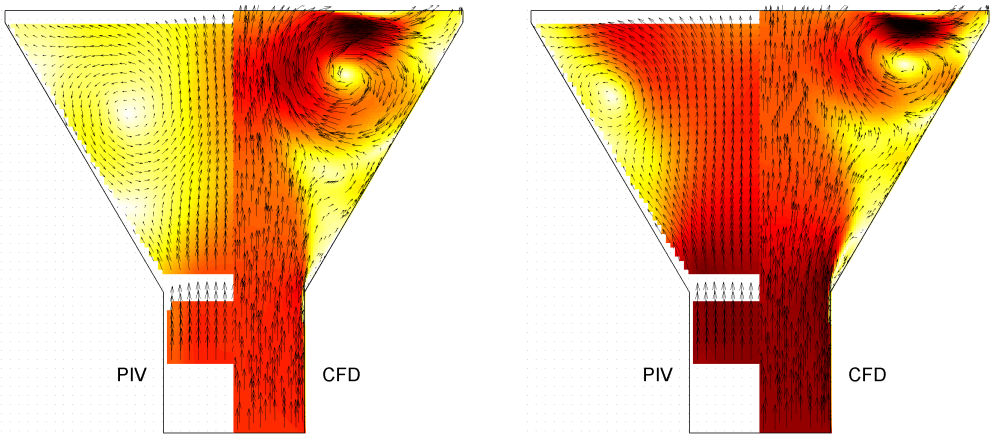

(a) $t/T = 0.1$ (b) $t/T = 0.2$

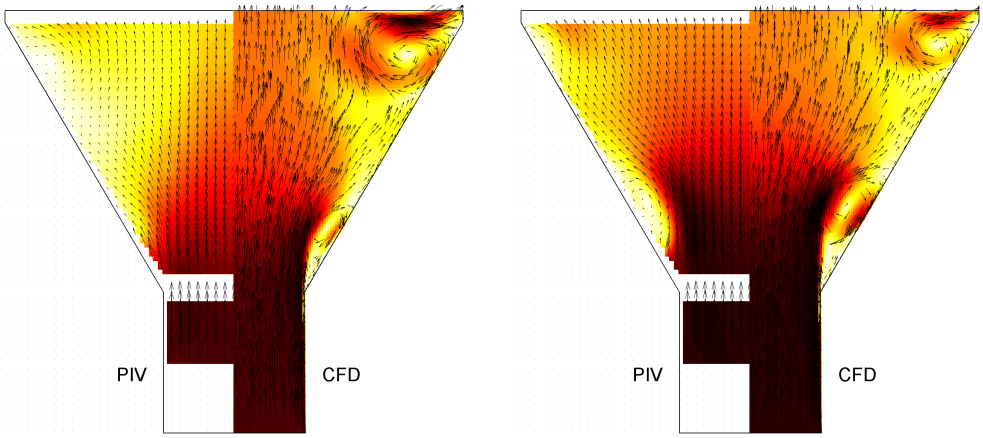

(c) $t/T = 0.3$ (d) $t/T = 0.4$

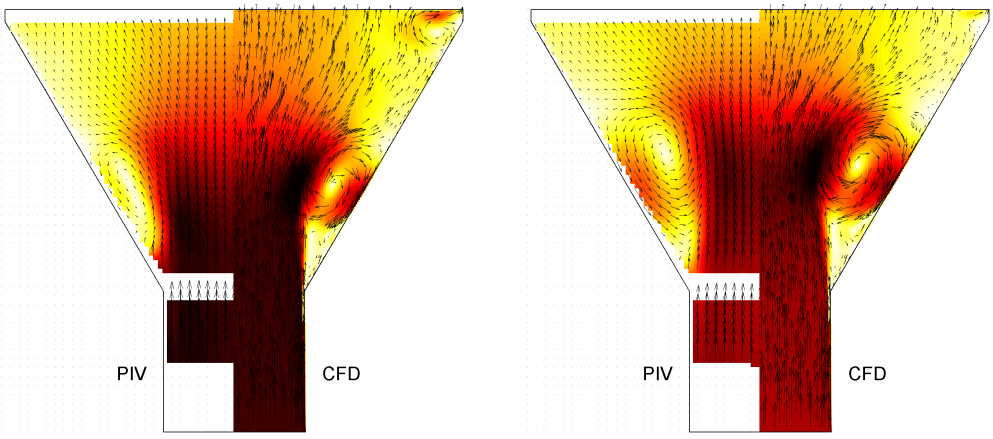

(e) $t/T = 0.5$ (f) $t/T = 0.6$

Figure 6.3: Velocity vector fields for Case 3 ($\mathrm{Re} = 4.2 \times 10^4$, $f = 100$ Hz, $J = 3.4$)

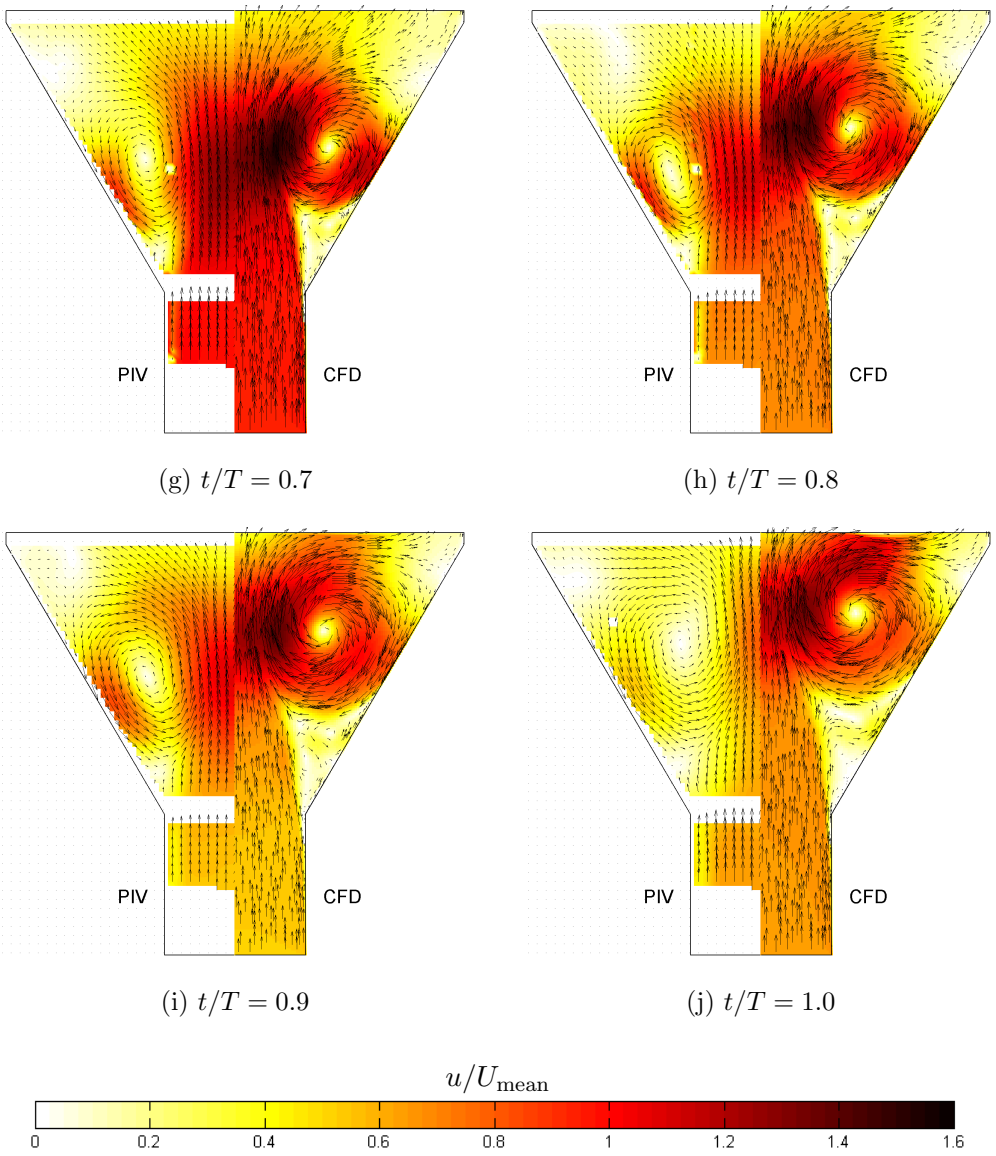

(g) $t/T = 0.7$ (h) $t/T = 0.8$

(i) $t/T = 0.9$ (j) $t/T = 1.0$

Figure 6.3: Velocity vector fields for Case 3 ($\text{Re} = 4.2 \times 10^4$, $f = 100$ Hz, $J = 3.4$) (cont.)

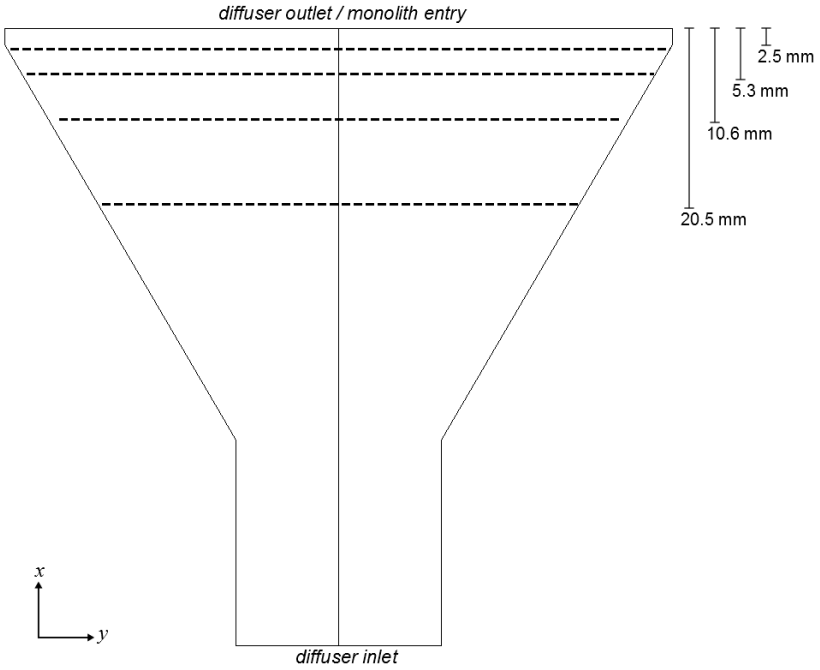

Figure 6.4: Location of examined velocity profiles

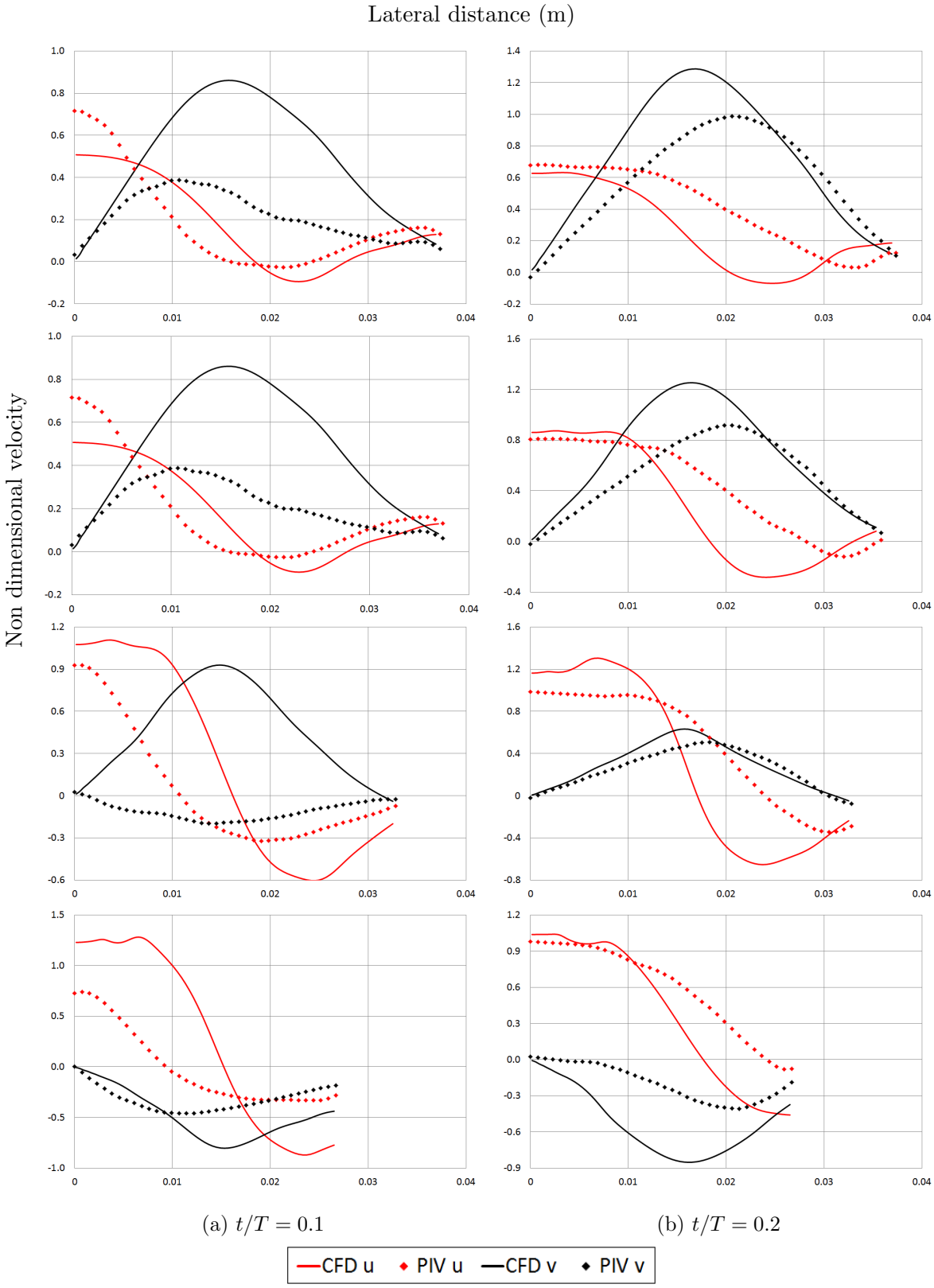

(a) $t/T = 0.1$ (b) $t/T = 0.2$

Figure 6.5: Velocity profiles (from top to bottom) 2.5, 5.3, 10.6 and 20.5 mm upstream of the monolith for Case 1. (cont.)

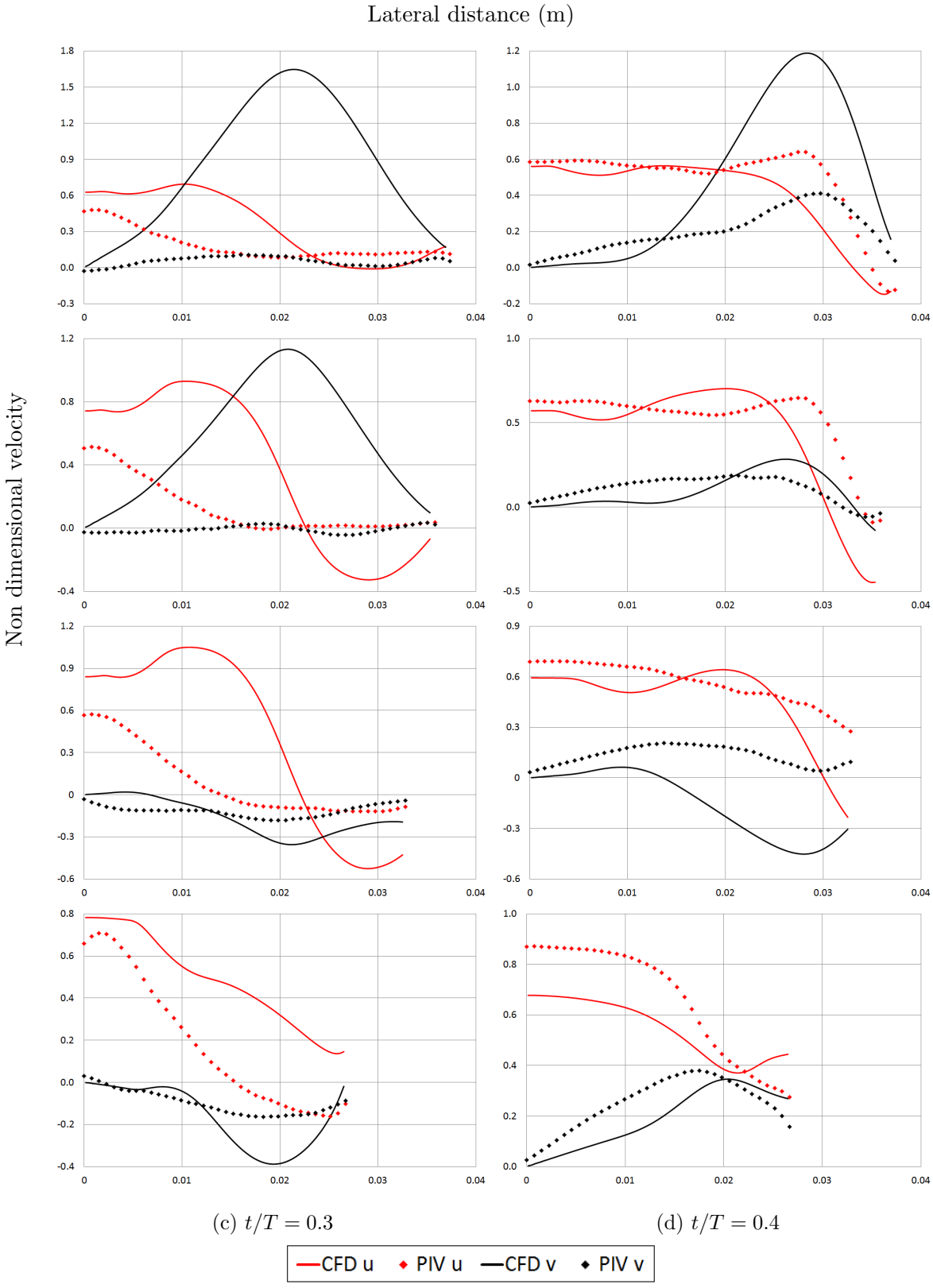

(c) $t/T = 0.3$ (d) $t/T = 0.4$

Figure 6.5: Velocity profiles (from top to bottom) 2.5, 5.3, 10.6 and 20.5 mm upstream of the monolith for Case 1. (cont.)

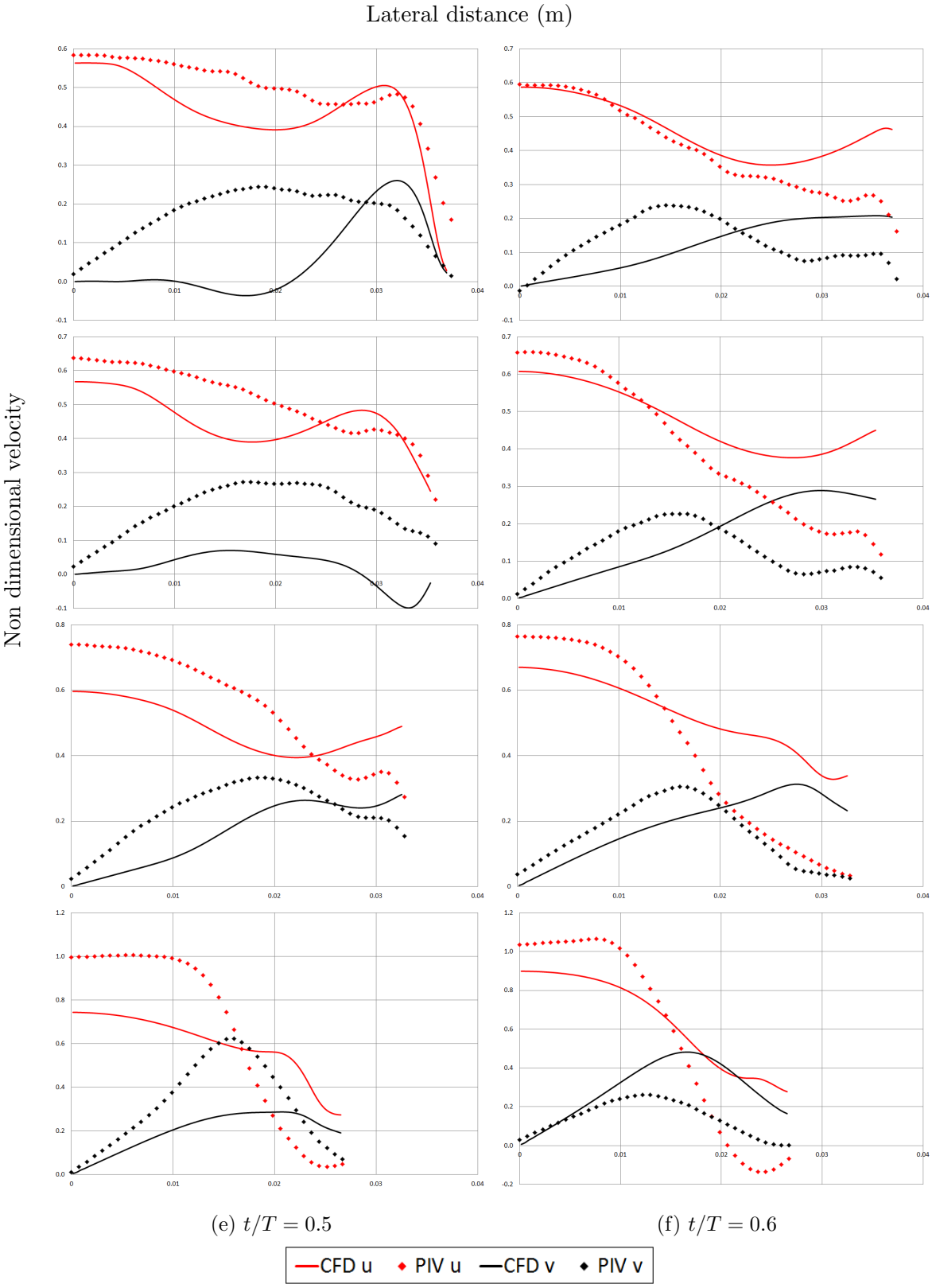

(e) $t/T = 0.5$ (f) $t/T = 0.6$

Figure 6.5: Velocity profiles (from top to bottom) 2.5, 5.3, 10.6 and 20.5 mm upstream of the monolith for Case 1. (cont.)

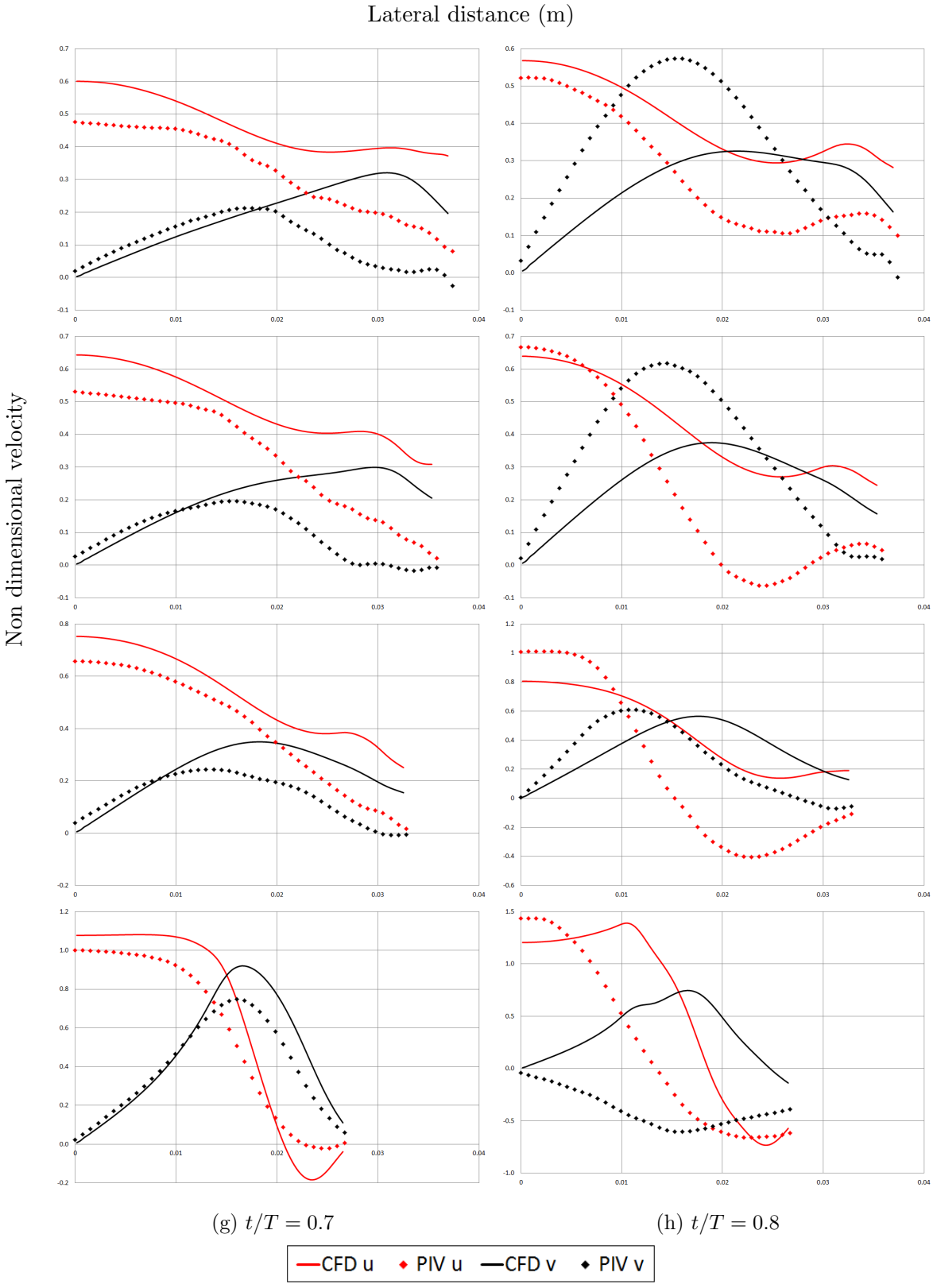

(g) $t/T = 0.7$ (h) $t/T = 0.8$

Figure 6.5: Velocity profiles (from top to bottom) 2.5, 5.3, 10.6 and 20.5 mm upstream of the monolith for Case 1. (cont.)

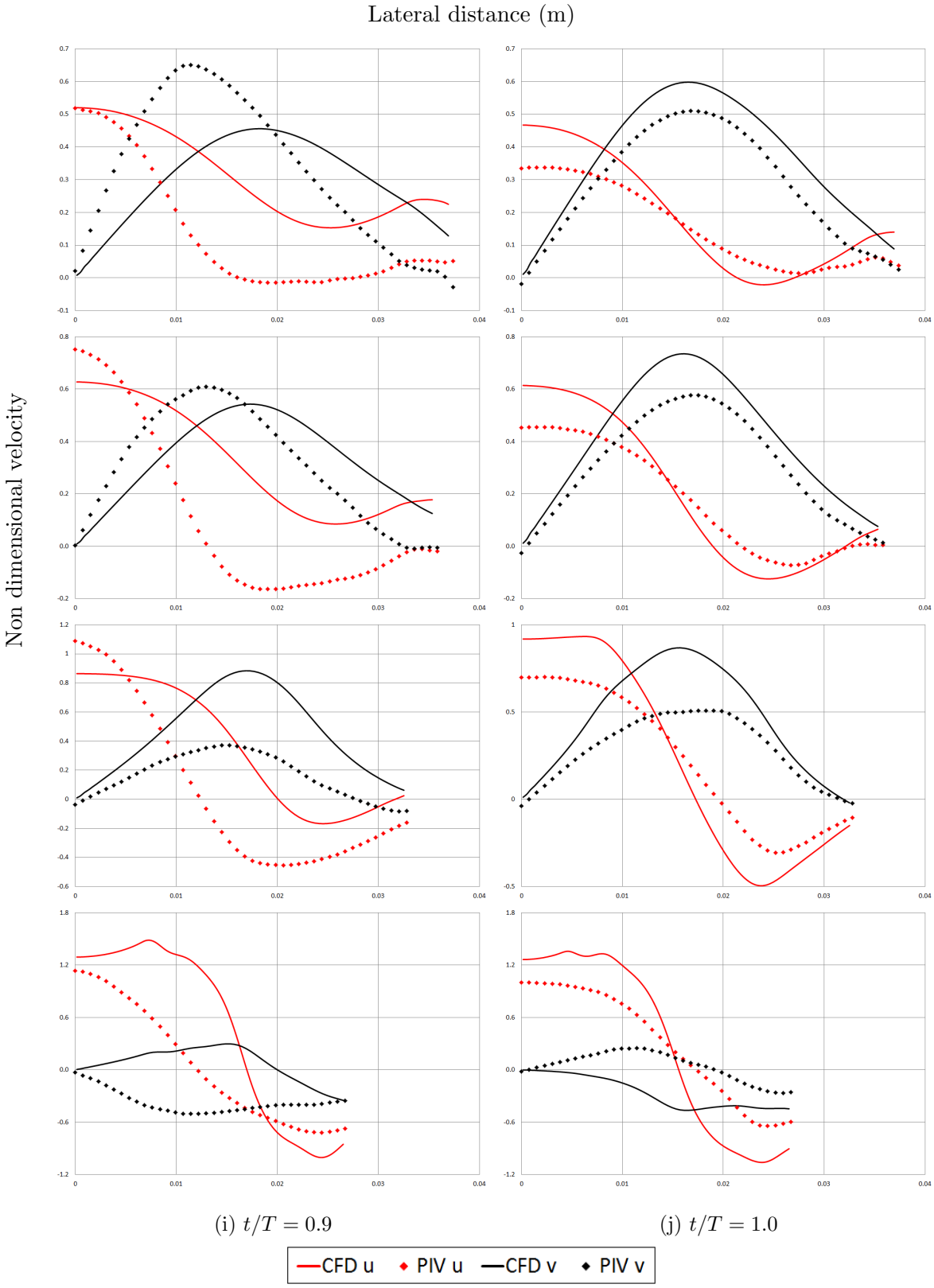

Figure 6.5: Velocity profiles (from top to bottom) 2.5, 5.3, 10.6 and 20.5 mm upstream of the monolith for Case 1. (cont.)

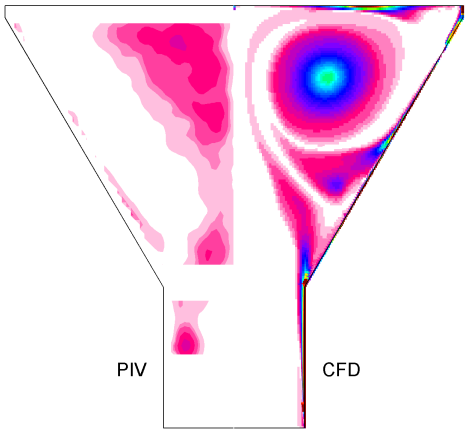

(a) $t/T = 0.1$

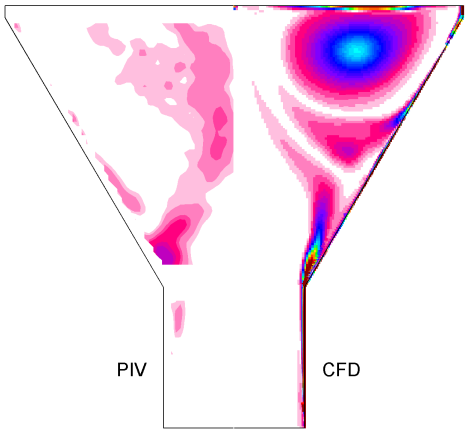

(b) $t/T = 0.2$

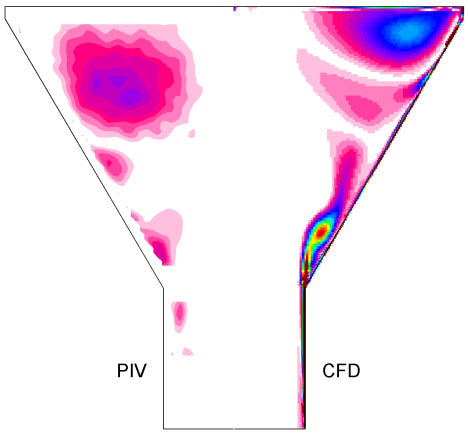

(c) $t/T = 0.3$

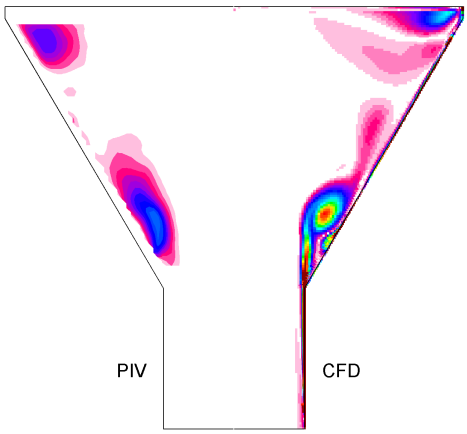

(d) $t/T = 0.4$

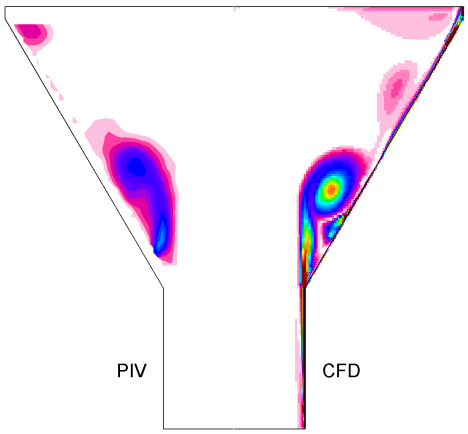

(e) $t/T = 0.5$

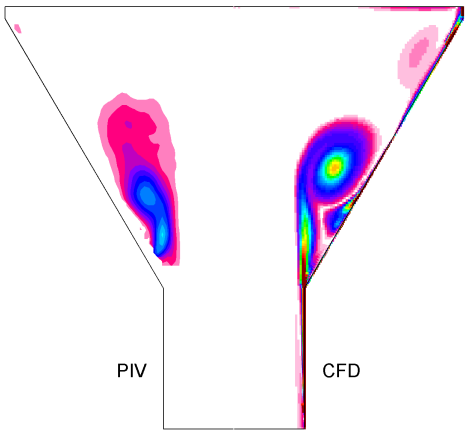

(f) $t/T = 0.6$

Figure 6.6: Vorticity contours for Case 1 ($\mathrm{Re} = 2.2 \times 10^4$, $f = 50$ Hz, $J = 3.4$)

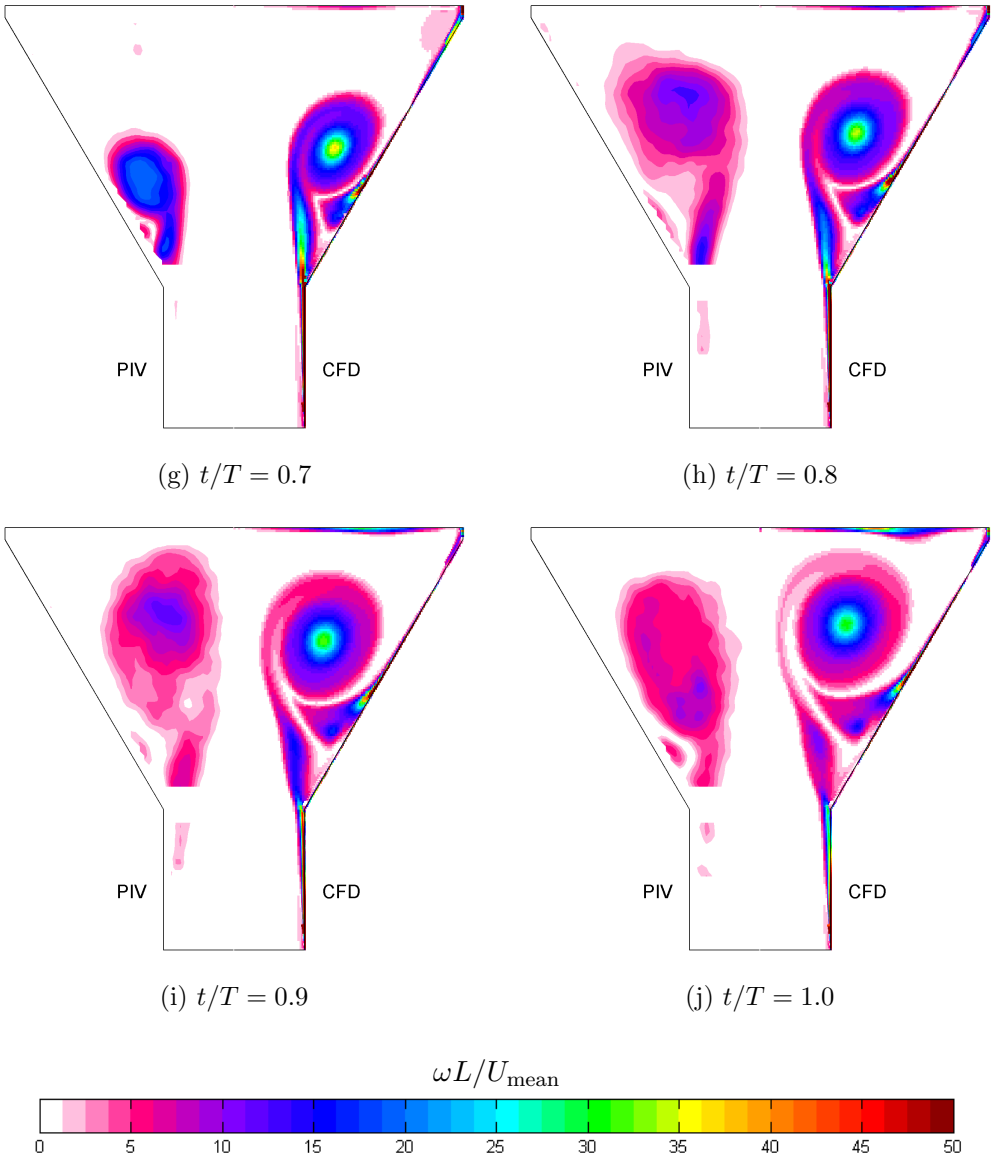

(g) $t/T = 0.7$ (h) $t/T = 0.8$

(i) $t/T = 0.9$ (j) $t/T = 1.0$

Figure 6.6: Vorticity contours for Case 1 ($\text{Re} = 2.2 \times 10^4$, $f = 50$ Hz, $J = 3.4$) (cont.)

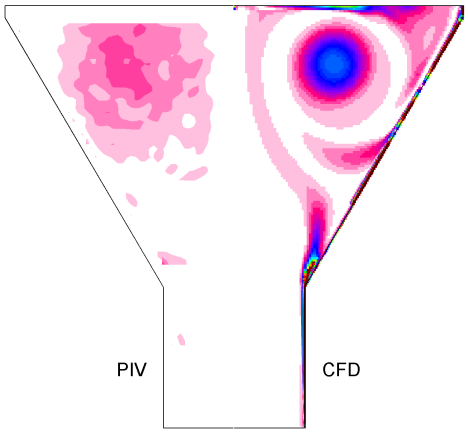

(a) $t/T = 0.1$

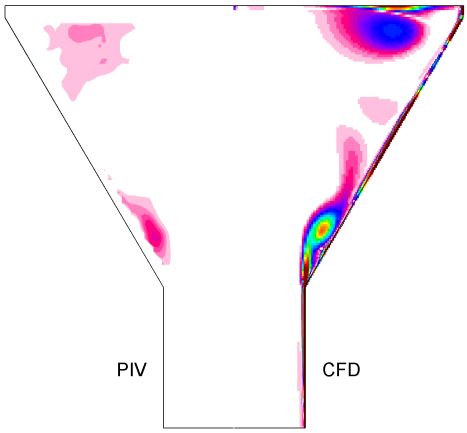

(b) $t/T = 0.2$

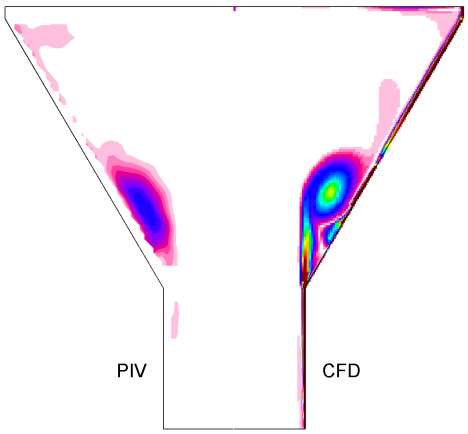

(c) $t/T = 0.3$

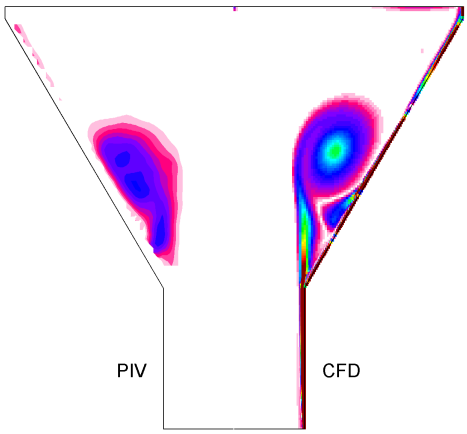

(d) $t/T = 0.4$

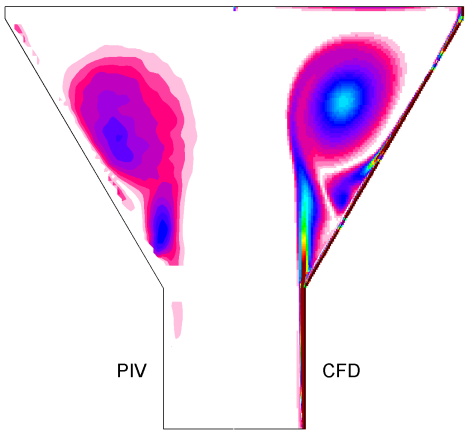

(e) $t/T = 0.5$

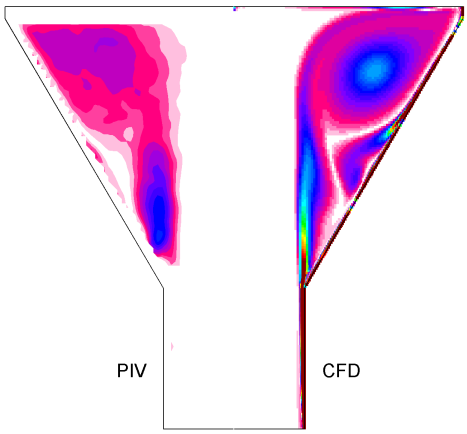

(f) $t/T = 0.6$

Figure 6.7: Vorticity contours for Case 2 ($\mathrm{Re} = 4.2 \times 10^4$, $f = 50$ Hz, $J = 6.8$)

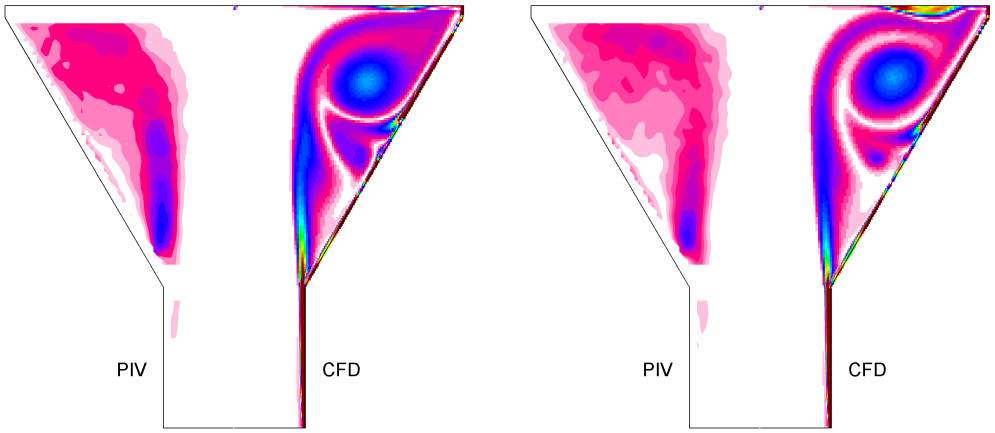

(g) $t/T = 0.7$ (h) $t/T = 0.8$

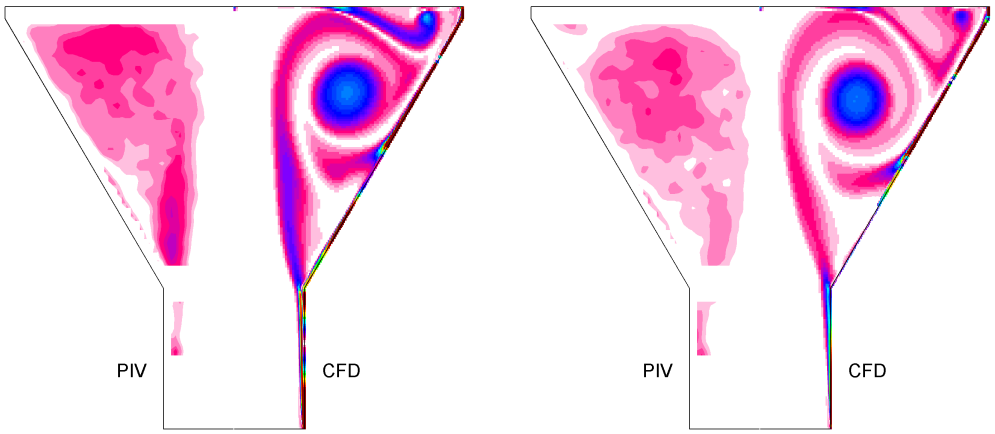

(i) $t/T = 0.9$ (j) $t/T = 1.0$

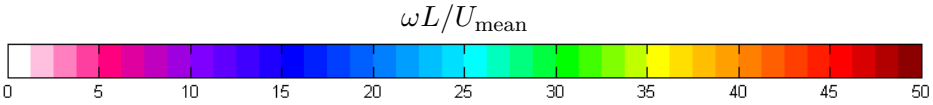

Figure 6.7: Vorticity contours for Case 2 ($\text{Re} = 4.2 \times 10^4$, $f = 50$ Hz, $J = 6.8$) (cont.)

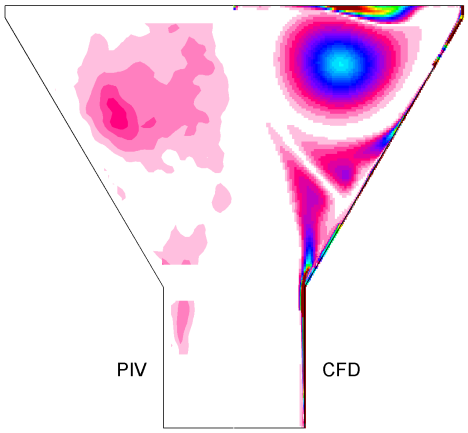

(a) $t/T = 0.1$

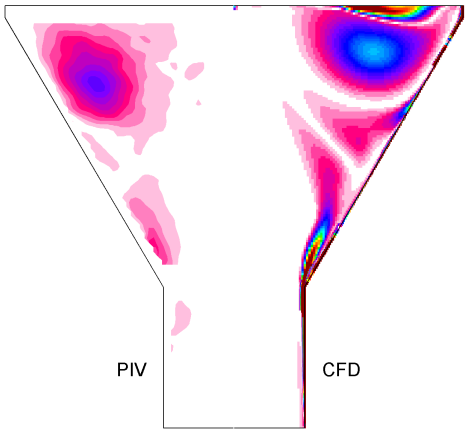

(b) $t/T = 0.2$

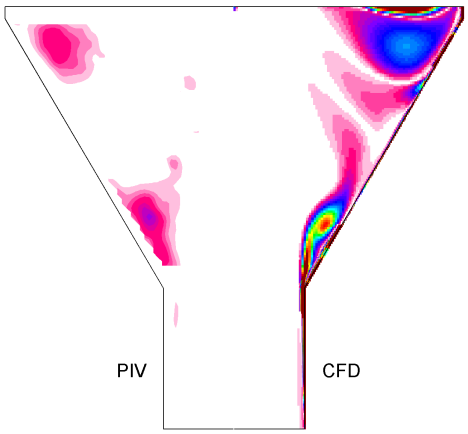

(c) $t/T = 0.3$

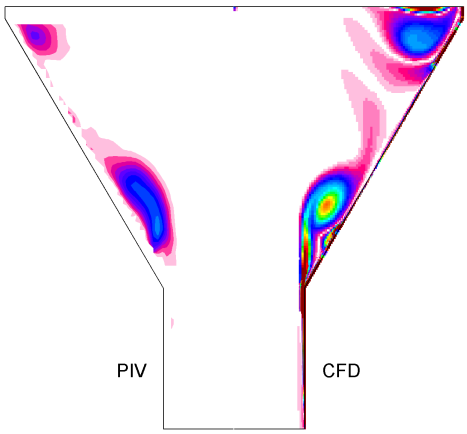

(d) $t/T = 0.4$

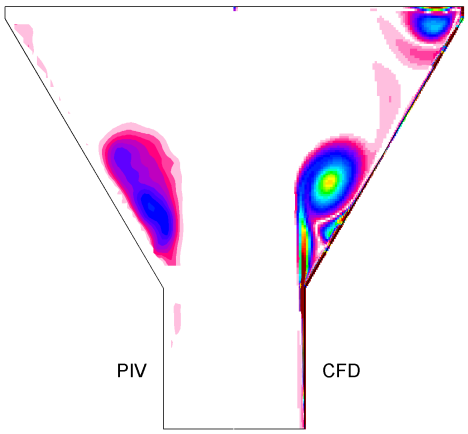

(e) $t/T = 0.5$

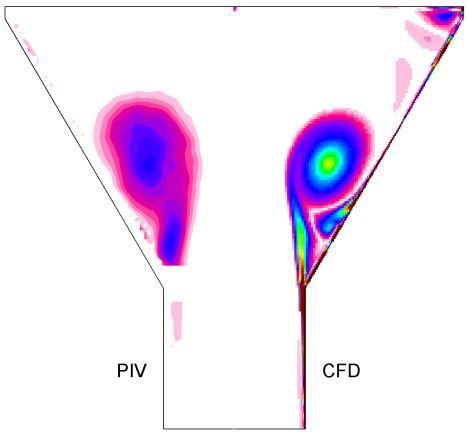

(f) $t/T = 0.6$

Figure 6.8: Vorticity contours for Case 3 ($\mathrm{Re} = 4.2 \times 10^4$, $f = 100$ Hz, $J = 3.4$)

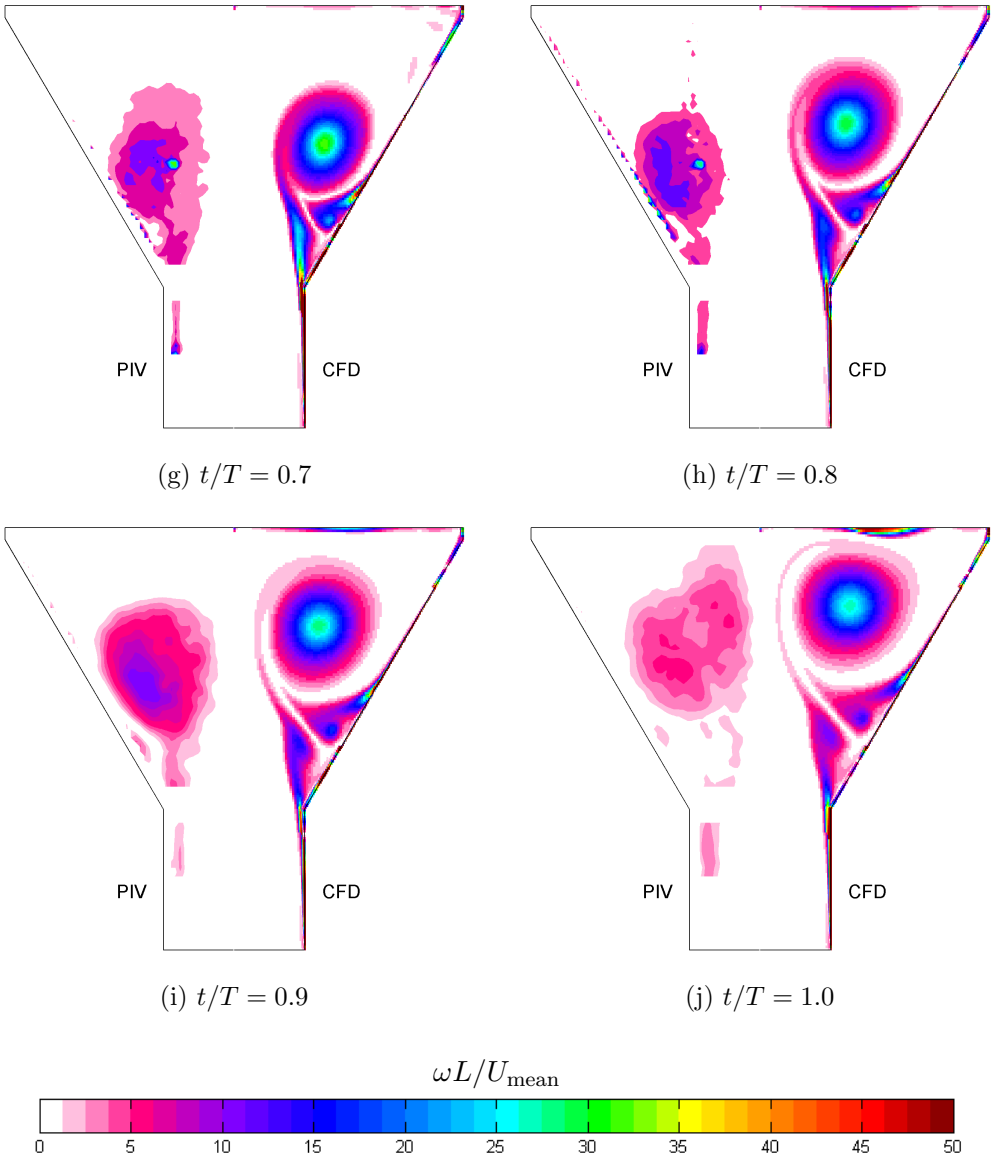

(g) $t/T = 0.7$ (h) $t/T = 0.8$

(i) $t/T = 0.9$ (j) $t/T = 1.0$

Figure 6.8: Vorticity contours for Case 3 ($\text{Re} = 4.2 \times 10^4$, $f = 100$ Hz, $J = 3.4$) (cont.)

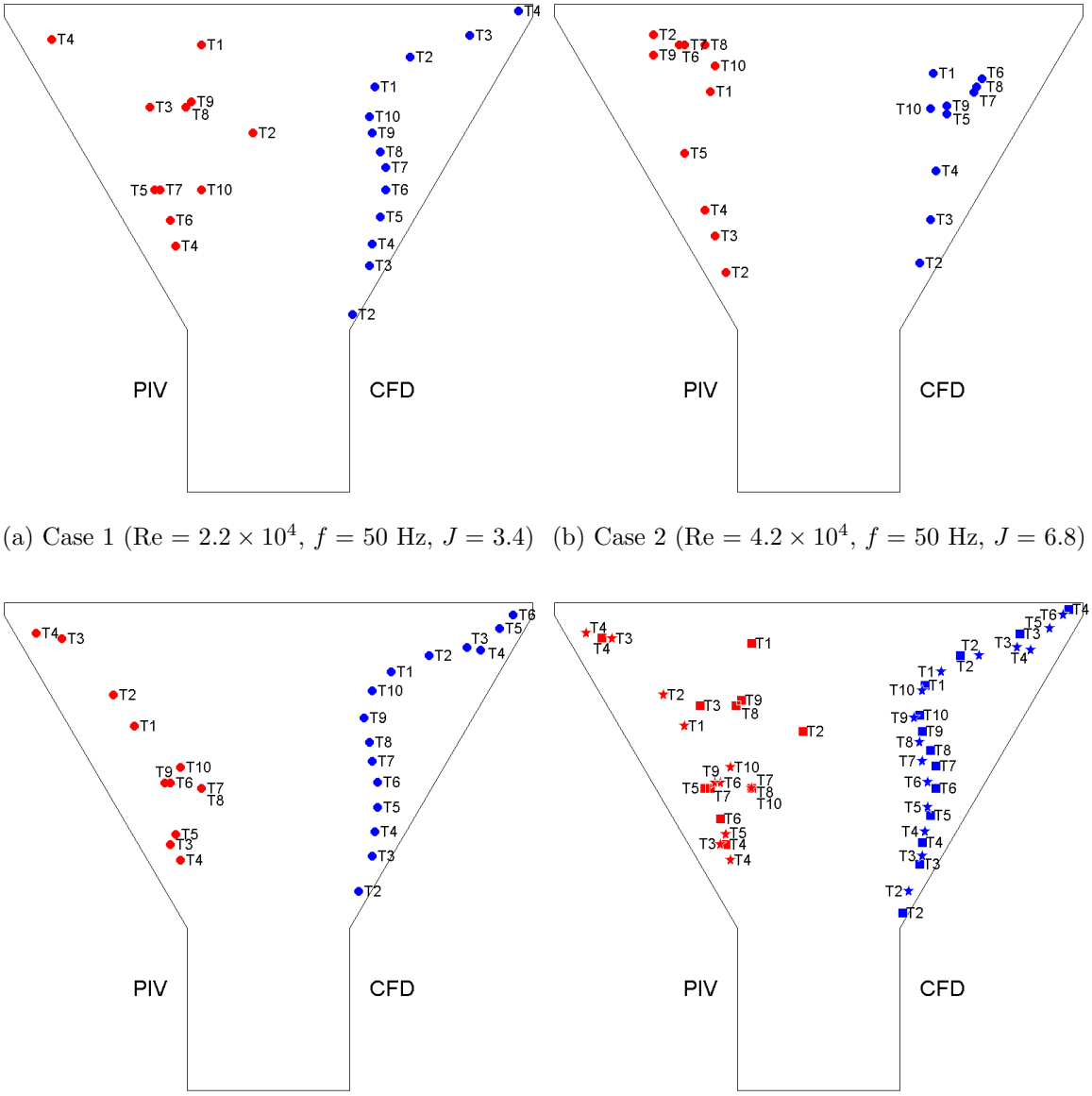

(a) Case 1 (Re $= 2.2 \times 10^4$, $f = 50$ Hz, $J = 3.4$) (b) Case 2 (Re $= 4.2 \times 10^4$, $f = 50$ Hz, $J = 6.8$)

(c) Case 3 (Re $= 4.2 \times 10^4$, $f = 100$ Hz, $J = 3.4$) (d) Cases 1 (■) and 3 (★) ($J = 3.4$)

Figure 6.9: Location of vorticity maxima throughout pulse cycle

6.2 Instantaneous Flow Fields

To examine the effect of phase-averaging on PIV data, instantaneous vorticity fields are considered for Case 2 ($\mathrm{Re} = 4.2 \times 10^4$, $f = 50$ Hz, $J = 6.8$).

PIV measurements were obtained by Mat Yamin, (2012) for 100 cycles. Fluctuations of inlet velocity are presented in Figure 6.10, with values normalised by the cycle-averaged inlet velocity U_{mean}. Figure 6.10(a) shows the mean inlet velocity, with standard deviation at each time-step of the pulse, and Figure 6.10(b) presents the standard deviation at each time-step, as an absolute value and also as a coefficient of variation σ/U_{mean}. Maximum standard deviation is sufficiently small to eliminate velocity variation at the inlet as a contributing factor to differences in the diffuser.

Figures 6.11 and 6.12 compare CFD predictions with instantaneous PIV measurements for the time-steps $t/T = 0.2$ and $t/T = 0.5$ respectively. 10 cases have been randomly selected, as presented by (Saul et al., 2015).

At $t/T = 0.2$ (Figures 6.7(b), 6.11), the inlet velocity is increasing and the vortex present in the diffuser is residual from the previous cycle. Instantaneous vorticity plots (Figure 6.11) are quite dissimilar to the averaged values presented (Figure 6.7(b)). Vorticity is scattered and clear vortex centres are not identifiable, however peak magnitudes in the main diffuser body are comparable to those predicted by CFD.

More correlation is seen at time-step $t/T = 0.5$ (Figures 6.7(e), 6.12). The cycle averaged flow field in Figure 6.7(e) shows adequate agreement with CFD for size and location of the vortex at the diffuser expansion, however peak magnitudes are approximately 50% less than predicted by CFD. The instantaneous plots in Figure 6.12 show variation of vortex location and peak magnitude from cycle to cycle, however the majority of cases display the same peak magnitude, $\omega L/U_{\mathrm{mean}} \sim 45$ as for CFD predictions.

Examination of instantaneous flow field measurements reveals a large amount of cyclic variation. This is not accounted for in a RANS-based simulation, which is therefore inappropriate for this case. The more detailed solutions provided by LES or DNS are desirable. The variation between the instantaneous flow field and the corresponding phase-average is the subject of ongoing research at Coventry University (Saul et al., 2015).

(a) Average inlet pulse shape, with error bars indicating standard deviation (Saul et al., 2015)

(b) Standard deviation of inlet velocities at each point of the cycle

Figure 6.10: Inlet pulse shape statistics of 100 individual cycles, Case 2.

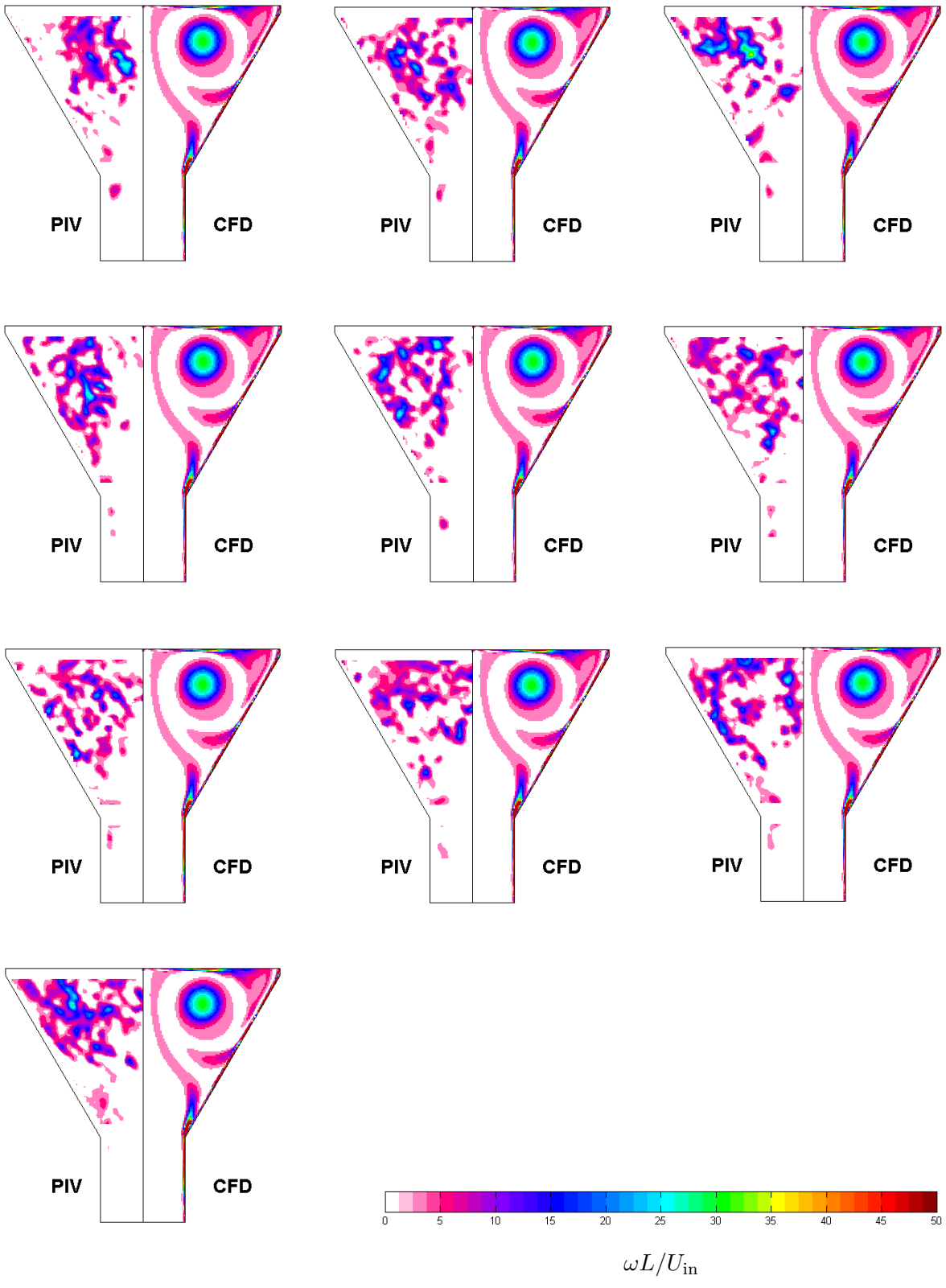

Figure 6.11: Instantaneous vorticity contour plots at $t/T = 0.2$, Case 2 ($\text{Re} = 4.2 \times 10^4$, $f = 50$ Hz, $J = 6.8$)

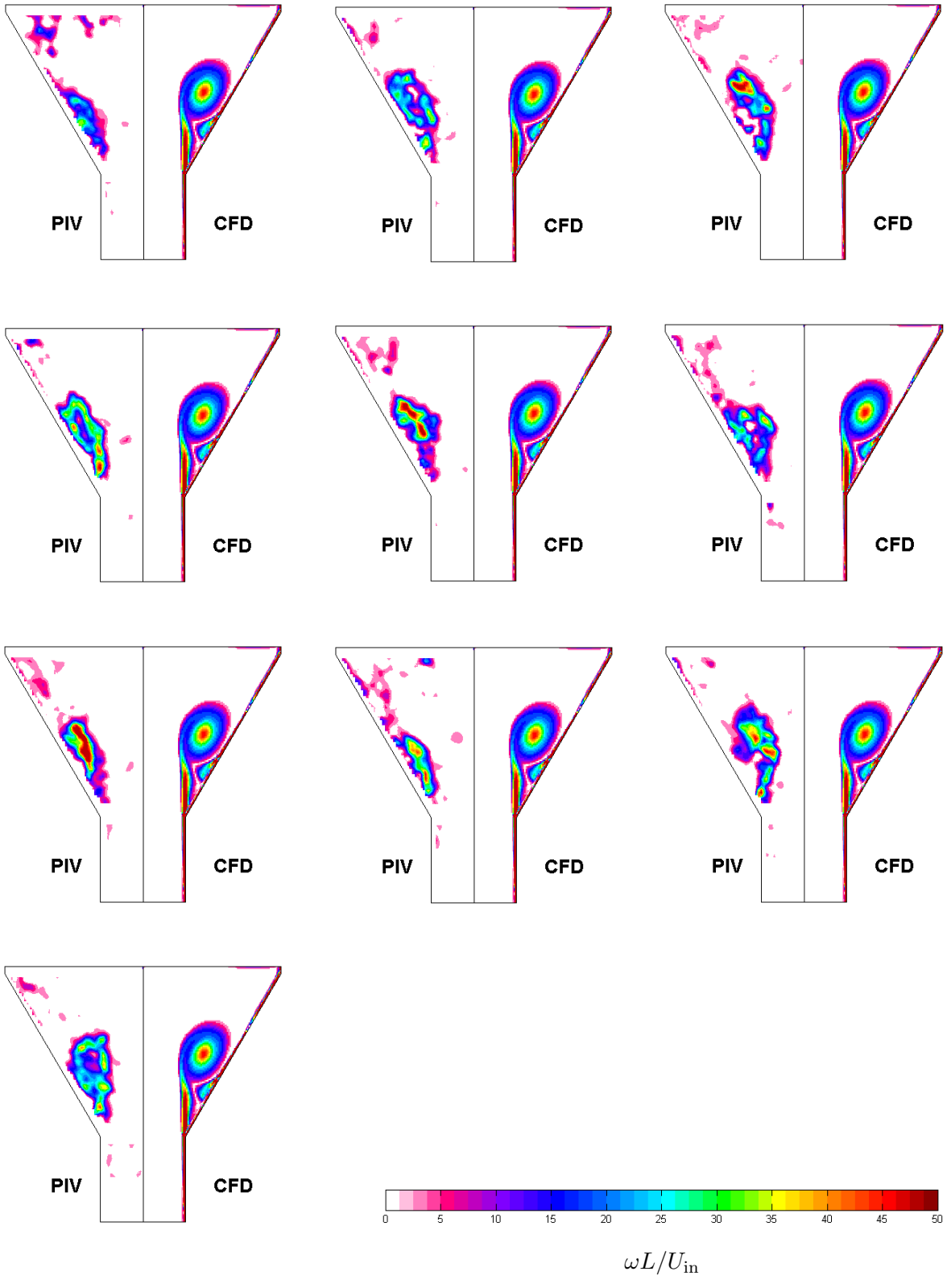

Figure 6.12: Instantaneous vorticity contour plots at $t/T = 0.5$, Case 2 ($\text{Re} = 4.2 \times 10^4$, $f = 50$ Hz, $J = 6.8$)

7 | Conclusion

7.1 Conclusions

The main aim of this work was to assess the performance of RANS-based computational fluid dynamics as applied to catalytic converter systems. To this end, the v^2f and RST turbulence models have been used to resolve the flow features in an idealised planar diffuser configuration representative of a generic catalyst system.

Modelling approaches have been implemented using the commercial CFD code Star-CCM+ and the performance of each model has been evaluated via comparison with the experimental data from PIV and HWA measurements performed by Mat Yamin, (2012), complemented with additional measurements collected as part of this project.

Established porous medium approaches were employed for modelling the pressure drop across the catalyst monolith, including oblique entry, critical angle and 'condensed monolith' formulations. Representing the monolith as a porous medium requires a semi-empirical approach for entry losses and does not provide detailed information about flow inside the monolith. A model with individual channels was therefore considered to gain insight into the flow physics within the monolith structure.

From the initial assessment it was found that the individual channel approach (with a few exceptions - for example, see Figure 5.11(b)) consistently produced more accurate predictions than the porous medium approach (Porter et al., 2014). Results from the individual channels model confirmed the influence of the oblique entry effect on the flow structure both upstream and downstream of the monolith as well as on the pressure loss across the monolith. Separation zones are clearly observed in channels with highly oblique entrance flow. Furthermore, the individual channels model demonstrates the formation of microjets at the monolith exit and the mixing of the jets downstream of the monolith, which the porous medium approach fails to capture. However, the detail achieved by this model is counteracted by the high computational demand associated with the refined mesh necessary inside each channel. It is therefore not a cost-effective solution needed to support the initial design process, where CFD is routinely used in industry.

In order to provide a methodology combining the cost-effectiveness of the porous medium approach with the fidelity of the individual channels approach, a novel hybrid approach was proposed, implemented and evaluated. Since the benefits of the individual channels approach mostly result from

detailed modelling of the region where flow enters the monolith, the new method includes individual channels at the inlet area of the monolith. The Hagen-Poiseuille expression for friction losses in fully developed channel flow was used to determine the length of the developing flow region covered by the individual channel approach. Once the channel flow is fully developed, the remaining part of the monolith was treated as porous medium with resistance coefficients calculated theoretically based on the Hagen-Poiseuille formulation.

The proposed hybrid model was found to generate results comparable with those obtained using the individual channels model ($\sim 2\%$ difference in maximum axial velocity downstream of the monolith), while reducing the number of mesh elements by an order of magnitude. The most important feature of the proposed hybrid model is that it eliminates the need for experimental estimation of oblique entry losses, which is required by the porous medium model and is subject to uncertainty. The hybrid model also preserves the individual jets exiting the monolith and thus provides improved predictions for mixing downstream of the monolith.

Although steady flow studies provide a useful insight into the performance of catalytic converters, the flow through the exhaust system is pulsating under operating conditions. It is therefore highly important to understand and assess the suitability of URANS for modelling such flows. Due to the extra computational demand associated with unsteady flow simulations, the standard porous medium model was used since it requires the lowest mesh density and is considered adequate for assessing the flow behaviour in the diffuser, upstream of the monolith.

The simulation results presented in this work show that a URANS approach adequately predicts general flow features, capturing the formation of vortices and their motion through the diffuser during the pulse cycle. Consequently, URANS could potentially be useful in the initial design stage of aftertreatment systems. However, the results also show that URANS overpredicts the PIV phased-averaged vortex strength (estimated using vorticity magnitudes), especially towards the end of the pulse and approximately by a factor of two. This was attributed to several factors, including turbulence model limitations in general, fundamental deficiencies of the URANS approach, as well as an inherent variance of the vortex strength and location observed in experiments (Saul et al., 2015).

Due to the existing gap in knowledge on the effect of cyclic variance on the phased-averaged flow field, it has been investigated in detail. Interestingly, it was found that despite relatively small cycle to cycle variance in the inlet conditions ($< 0.08\%$), the instantaneous vorticity fields show significant change in the location of the vortex core from cycle to cycle, and this has the effect of reducing the calculated phased-averaged peak vorticity. The instantaneous peak vorticity was found to be up to three times higher than the phase-averaged value and was comparable in magnitude to the peak values

obtained from the URANS predictions. This contribution suggests that other simulation techniques such as DNS or LES are more suitable for later stages in the design process where more detailed information about the flow is required.

7.2 Original Contribution

The contributions to knowledge resulting from this work are:

- Implementation and evaluation of several porous medium approaches in Star-CCM+, including oblique entry effect with and without critical angle, and 'condensed monolith' method;
- Using the individual channels model, establishment of the relative importance of capturing the flow structure in the entrance region of the monolith for improved CFD predictions for the whole system and in simulating mixing at the rear of the monolith;
- Proposal, development, implementation and validation of a novel hybrid approach for modelling the catalyst monolith, thus reducing computational time while accurately representing flow behaviour upon entry into the monolith channels;
- Identification of the effect of cyclic variance on phased-averaged PIV results and demonstration of an overprediction by CFD of phased-averaged vorticity values, but agreement of CFD predictions with instantaneous vorticity magnitudes.

7.3 Recommendations for Future Work

Based on the work undertaken as part of this study, recommendations are made for further research.

- Development of the CFD models presented in this work to a three-dimensional system;
- Inclusion of more complex flow phenomena such as swirl, with or without pulsation;
- Extension of the hybrid modelling validation to include pulsating flows;
- Assessment of the ability of DNS and/or LES to capture cyclic variance of pulsating flow.

References

Al-Haddad, A. A. and Al-Binally, N. (1989). 'Prediction of heat transfer coefficient in pulsating flow'. *International Journal of Heat and Fluid Flow* 10(2):131–133. ISSN: 0142727X. DOI: 10.1016/0142-727X(89)90006-4.

Arias-García, A, Benjamin, S. F., Zhao, H, and Farr, S (2001). 'A comparison of steady, pulsating flow measurements and CFD simulations in close coupled catalysts'. *SAE Technical Paper*:2001–01–36. DOI: 10.4271/2001-01-3662.

Aris, R. (1977). 'Models of the catalytic monolithic'. *Physicochemical Hydrodynamics: V. G. Levich Festschrift*. Ed. by Spalding, D. B. Oxford: Advance Publications Ltd, pp. 815–825. ISBN: 0903012405.

Benjamin, S. F. and Roberts, C. A. (2000). 'Warm up of an automotive catalyst substrate by pulsating flow: a single channel modelling approach'. *International Journal of Heat and Fluid Flow* 21(6):717–726. DOI: 10.1016/S0142-727X(00)00025-4.

Benjamin, S. F., Clarkson, R. J., Haimad, N., and Girgis, N. S. (1996). 'An experimental and predictive study of the flow field in axisymmetric automotive exhaust catalyst systems'. *SAE Technical Paper*:961208. DOI: 10.4271/961208.

Benjamin, S. F., Roberts, C. A., and Wollin, J. (2001). 'A study of the effect of flow pulsations on the flow distribution within ceramic contoured catalyst substrates'. *SAE International Journal of Fuels and Lubricants* 4(110):1380–1387. DOI: 10.4271/2001-01-1996.

– (2002). 'A study of pulsating flow in automotive catalyst systems'. *Experiments in Fluids* 33:629–639. DOI: 10.1007/s00348-002-0481-0.

Benjamin, S. F., Liu, Z., and Roberts, C. A. (2004). 'Automotive catalyst design for uniform conversion efficiency'. *Applied Mathematical Modelling* 28(6):559–572. ISSN: 0307904X. DOI: 10.1016/j.apm.2003.10.008.

Bhattacharya, M, Harold, M. P., and Balakotaiah, V (2004). 'Mass-transfer coefficients in washcoated monoliths'. *AIChE Journal* 50(11):2939–2955. DOI: 10.1002/aic.10212.

Bressler, H., Rammoser, D., Neumaier, H., and Terres, F. (1996). 'Experimental and predictive investigation of a close coupled catalytic converter with pulsating flow'. *SAE Technical Paper*:960564. ISSN: 0148-7191. DOI: 10.4271/960564.

Catalano, P., Wang, M., Iaccarino, G., and Moin, P. (2003). 'Numerical simulation of the flow around a circular cylinder at high Reynolds numbers'. *International Journal of Heat and Fluid Flow* 24(4):463–469. DOI: 10.1016/S0142-727X(03)00061-4.

CD-adapco (2013). *Star-CCM+ Version 8.04 User Guide*.

Cho, H. W. and Hyun, J. M. (1990). 'Numerical solutions of pulsating flow and heat transfer characteristics in a pipe'. *International Journal of Heat and Fluid Flow* 11(4):321–330. DOI: 10.1016/0142-727X(90)90056-H.

Clarkson, R. J. (1995). 'A theoretical and experimental study of automotive catalytic converters'. PhD thesis. Coventry University.

Cokljat, D, Kim, S. E., Iaccarino, G., and Durbin, P. A. (2003). 'A comparative assessment of the V2F model for recirculating flows'. *41st Aerospace Sciences Meeting and Exhibit*. Reno, Nevada. DOI: AIAA-2003-675.

Comfort, E. H. (1974). 'Monolithic catalytic converter performance as a function of flow distribution'. *ASME Winter Annual Meeting, Paper No.74-WA/HT-30*.

Dantec Dynamics (2014). *Probes for hot-wire anemometry*. Skovlunde, Denmark: Dantec Dynamics.

Day, E. G. W., Benjamin, S. F., and Roberts, C. A. (1999). 'Single channel studies of heat transfer in automotive exhaust catalytic converters'. *4th Joint IMechE/SAE Vehicle Thermal Management Systems Conference*. London, pp. 347–363.

DieselNet (2015). *Emissions Standards: European Union - Cars and Light Trucks* [https://www.dieselnet.com/standards/eu/ld.php].

Durbin, P. A. (1991). 'Near-wall turbulence closure modeling without 'damping functions''. *Theoretical and Computational Fluid Dynamics* 3.

– (1995). 'Separated flow computations with the k-ϵ-v^2 model'. *AIAA Journal* 33(4):659–664. DOI: 10.2514/3.12628.

El-Behery, S. M. and Hamed, M. H. (2011). 'A comparative study of turbulence models performance for separating flow in a planar asymmetric diffuser'. *Computers & Fluids* 44(1):248–257. ISSN: 00457930. DOI: 10.1016/j.compfluid.2011.01.009.

García-Villalba, M., Fröhlich, J., and Rodi, W (2006). 'Identification and analysis of coherent structures in the near field of a turbulent unconfined annular swirling jet using large eddy simulation'. *Physics of Fluids* 18(5):1–17. ISSN: 10706631. DOI: 10.1063/1.2202648.

Garde, R. J. (2010). *Turbulent flow*. Third. Kent: New Age Science Limited. ISBN: 978 1 906574 31 4.

Gibson, M. M. and Launder, B. E. (1978). 'Ground effects on pressure fluctuations in the atmospheric boundary layer'. *Journal of Fluid Mechanics* 86(3):491–511. DOI: 10.1017/S0022112078001251.

Haimad, N. (1997). 'A theoretical and experimental investigation of the flow performance of automotive catalytic converters'. PhD thesis. Coventry University.

Hauber, T., Zacke, P., Braun, J., and Ueberschär, D. (1998). 'Influence of the space between monoliths and the geometry of endcones on the conversion rate of a catalytic converter'. *SAE Technical Paper*:980424. DOI: 10.4271/980424.

Howitt, J. S. and Sekella, T. C. (1974). 'Flow effects in monolithic honeycomb automotive catalytic converters'. *SAE Technical Paper*:740244. DOI: 10.4271/740244..

Jeong, S.-J. and Kim, W. S. (2001). 'A three-dimensional numerical study of the effect of pulsating flow on conversion efficiency inside a catalytic converter'. *Proceedings of the Institution of Mechanical Engineers, Part D: Journal of Automobile Engineering* 215(1):45–61. DOI: 10.1243/0954407011525458.

Jeong, S. and Kim, T. (1997). 'CFD investigation of the 3-dimensional unsteady flow in the catalytic converter'. *SAE Technical Paper*:971025. DOI: 10.4271/971025.

Kandylas, I. P. and Stamatelos, A. M. (1999). 'Engine exhaust system design based on heat transfer computation'. *Energy Conversion & Management* 40(10):1057–1072. DOI: 10.1016/S0196-8904(99)00008-4.

Karvounis, E. and Assanis, D. N. (1993). 'The effect of inlet flow distribution on catalytic conversion efficiency'. *International Journal of Heat and Mass Transfer* 36(6):1495–1504.

Kašpar, J., Fornasiero, P., and Hickey, N. (2003). 'Automotive catalytic converters: Current status and some perspectives'. *Catalysis Today* 77(4):419–449. DOI: 10.1016/S0920-5861(02)00384-X.

Kim, J.-Y., Lai, M.-C., Li, P, and Chui, G. K. (1995). 'Flow distribution and pressure drop in diffuser-monolith flows'. *Journal of Fluids Engineering* 117(3):362–368. ISSN: 00982202. DOI: 10.1115/1.2817270.

Kim, S. Y., Kang, B. H., and Hyun, J. M. (1993). 'Heat transfer in the thermally developing region of a pulsating channel flow'. *International Journal of Heat and Mass Transfer* 36(17):4257–4266. ISSN: 00179310. DOI: 10.1016/0017-9310(93)90088-N.

Küchemann, D. and Weber, J. (1953). *Aerodynamics of propulsion*. New York: McGraw-Hill. Chap. 12.

Lai, M.-C., Kim, J.-Y., Cheng, C.-Y., Li, P, Chui, G. K., and Pakko, J. D. (1991). 'Three-dimensional simulations of automotive catalytic converter internal flow'. *SAE Technical Paper*:910200. DOI: 10.4271/910200.

Liu, Z. (2003). 'Pulsating flow maldistribution in automotive exhaust catalysts - numerical modelling and experimental correlation'. PhD thesis. Coventry University.

Liu, Z., Benjamin, S. F., and Roberts, C. A. (2003). 'Pulsating flow maldistribution within an axisymmetric catalytic converter - flow rig experiment and transient CFD simulation'. *SAE Powertrain & Fluid Systems Conference & Exhibition*. DOI: 10.4271/2003-01-3070.

Martin, A. P., Will, N. S., Bordet, A, Cornet, P, Gondoin, C, and Mouton, X (1998). 'Effect of flow distribution on emissions performance of catalytic converters'. *SAE Technical Paper* 980936:980936. DOI: 10.4271/980936.

Mat Yamin, A. K. (2012). 'Pulsating flow studies in a planar wide-angled diffuser upstream of automotive catalyst monoliths'. PhD thesis. Coventry University.

Mat Yamin, A. K., Benjamin, S. F., and Roberts, C. A. (2013). 'Pulsating flow in a planar diffuser upstream of automotive catalyst monoliths'. *International Journal of Heat and Fluid Flow* 40:43–53. ISSN: 0142727X. DOI: 10.1016/j.ijheatfluidflow.2013.01.014.

Medina, H. J., Bernard, E, and Early, J. M. (2013). 'Reynolds number effects on fully developed pulsed jets impinging on flat Surfaces'. *AIAA Journal* 51(10):2305–2318. DOI: 10.2514/1.J051203.

Medina, H. J., Beechook, A., Saul, J. M., Porter, S. J., Aleksandrova, S., and Benjamin, S. F. (2015). 'Open source Computational Fluid Dynamics using OpenFOAM'. *Royal Aero-*

nautical Society General Aviation Conference, Light Aircraft Design: Methods and Tools. London.

Ozhan, C., Fuster, D., and Da Costa, P. (2014). 'Multi-scale flow simulation of automotive catalytic converters'. *Chemical Engineering Science* 116:161–171. DOI: 10.1016/j.ces.2014.04.044.

Park, S.-B., Kim, H.-S., Cho, K.-M., and Kim, W.-T. (1998). 'An experimental and computational study of flow characteristics in exhaust manifold and close-coupled catalyst'. *SAE Technical Paper*:980128. ISSN: 0148-7191. DOI: 10.4271/980128.

Persoons, T, Vanierschot, M, and Van den Bulck, E (2008). 'Oblique inlet pressure loss for swirling flow entering a catalyst substrate'. *Experimental Thermal and Fluid Science* 32(6):1222–1231. ISSN: 08941777. DOI: 10.1016/j.expthermflusci.2008.02.002.

Porter, S. J., Mat Yamin, A. K., Aleksandrova, S., Benjamin, S. F., Roberts, C. A., and Saul, J. M. (2014). 'An assessment of CFD applied to steady flow in a planar diffuser upstream of an automotive catalyst monolith'. *SAE International Journal of Engines* 7(4):DOI: 10.4271/2014-01-2588.

Porter, S. J., Saul, J. M., Mat Yamin, A. K., Aleksandrova, S., Benjamin, S. F., and Medina, H. J. (2015). 'Pulsating Flow in a Planar Diffuser Upstream of Automotive Catalyst Monoliths: A CFD Study'. *10th Pacific Symposium on Flow Visualization and Image Processing*. Naples, Italy.

Porter, S. J., Saul, J. M., Aleksandrova, S., Medina, H. J., and Benjamin, S. F. (In press). 'Hybrid flow modelling approach applied to automotive catalysts'. *Applied Mathematical Modelling*.

Pundir, B. P. (2007). *Engine emissions: Pollutant formation and advances in control technology*. Oxford: Alpha Science International Ltd. ISBN: 978-1-84265-401-9.

Quadri, S. S. (2008). 'The effect of oblique entry into an automotive catalyst on the flow distribution within the monolith'. PhD thesis. Coventry University.

Quadri, S. S., Benjamin, S. F., and Roberts, C. A. (2009a). 'An experimental investigation of oblique entry pressure losses in automotive catalytic converters'. *Proceedings of the Institution of Mechanical Engineers, Part C: Journal of Mechanical Engineering Science* 223(11):2561–2569. ISSN: 0954-4062. DOI: 10.1243/09544062JMES1565.

Quadri, S. S., Benjamin, S. F., and Roberts, C. A. (2009b). 'Flow measurements across an automotive catalyst monolith situated downstream of a planar wide-angled diffuser'. *Proceedings of the Institution of Mechanical Engineers, Part C: Journal of Mechanical Engineering Science* 224(2):321–328. ISSN: 0954-4062. DOI: 10.1243/09544062JMES1735.

Rodi, W (1991). 'Experience with two-layer models combining the k-ϵ model with a one-equation model near the wall'. *29th Aerospace Sciences Meeting*. AIAA Paper 91-0216.

Rodi, W and Scheuerer, G (1986). 'Scrutinizing the k-ϵ turbulence model under adverse pressure gradient conditions'. *Journal of Fluids Engineering* 108(2):174–179. ISSN: 00982202. DOI: 10.1115/1.3242559.

Saul, J. M., Porter, S. J., Mat Yamin, A. K., Medina, H. J., Aleksandrova, S., and Benjamin, S. F. (2015). 'Influence of cycle variance on the performance of URANS for pulsating flow upstream of an automotive catalyst monolith'. *Internal Combustion Engines*. London.

Shah, R. K. (1978). 'A correlation for hydrodynamic entry length solutions for circular and noncircular ducts'. *Journal of Fluids Engineering* 100:177–179. DOI: 10.1115/1.3448626.

Shah, R. K. and London, A. L. (1978). *Laminar flow forced convection in ducts: A source book for compact heat exchanger analytical data*. New York; London: Academic Press.

Shuai, S.-J., Wang, J.-X., Dong, Q.-L., and Zhuang, R.-J. (2001). 'PIV measurement and numerical simulation of flows in automotive catalytic converters'. *SAE Technical Paper*:2001–01–3494. DOI: 10.4271/2001-01-3494.

Taylor, K. C. (1984). *Automobile catalytic converters*. Berlin: Springer-Verlag. ISBN: 3-540-13064-0.

TSI Incorporated (2010). *IFA 300 Constant Temperature Anemometer System Operation Manual*.

Turner, C., Thornhill, D., McCullough, G., and Patel, S. (2011). 'Comparison of experimental PIV data and CFD simulations for flow in a diesel particulate filter inlet diffuser'. *SAE International Journal of Engines* 4(1):1556–1570. DOI: 10.4271/2011-01-1241.

Weltens, H., Bressler, H., Terres, F., Neumaier, H., and Rammoser, D. (1993). 'Optimisation of catalytic converter gas flow distribution by CFD prediction'. *SAE Technical Paper*:930780. ISSN: 0148-7191. DOI: 10.4271/930780.

Wendland, D. W. and Matthes, W. R. (1986). 'Visualization of automotive catalytic converter internal flows'. *SAE Technical Paper*:930780. DOI: 10.4271/861554.

Wendland, D. W., Sorrell, P. L., and Kreucher, J. E. (1991). 'Sources of monolith catalytic converter pressure loss'. *SAE Technical Paper*:912372. DOI: 10.4271/912372.

Wilcox, D. C. (2006). *Turbulence modelling for CFD*. 3rd. California, USA: DCW Industries. ISBN: 978-1-928729-08-2.

Will, N. S. and Bennett, C. J. (1992). 'Flow maldistributions in automotive converter canisters and their effect on emission control'. *SAE Technical Paper*:922339. DOI: 10.4271/922339.

Wollin, J. (2002). 'A study of pulsating flow in automotive exhaust catalyst systems'. PhD thesis. Coventry University.

Young, M. E. and Ooi, A (2007). 'Comparative assessment of LES and URANS for flow over a cylinder at a Reynolds number of 3900'. *16th Australasian Fluid Mechanics Conference*. Queensland, Australia, pp. 1063–1070. ISBN: 9781864998948.

Appendix A : Implementation of entrance effect in Star-CCM+

The method and syntax used for the inclusion of entrance effects are detailed. For details of the creation and definition of tables and field functions in Star-CCM+, see the user manual (CD-adapco, 2013).

Entrance effects are applied to the monolith model as an additional momentum source term $\mathbf{S}_i^v$. The source term is defined by the vector $[-\lambda, 0, 0]$ where λ is a scalar value derived as a function of flow velocity.

The table '1mm upstream vel' extracts velocity values at cells located along a line-probe 1mm upstream of the monolith and λ is calculated using the values. The table automatically extracts and updates values with each iteration of the model. For monolith length L, critical angle α_c and subcritical angle α_s, λ is calculated from the following definitions.

K-W (Eq. 4.10)

```
$Density*pow(interpolatePositionTable(Table("1mm upstream vel"),"Velocity[j]"),2)/2/L
```

Critical angle (Eq. 4.11)

```
( ${tan alpha} < ${tan critical angle} ) ?
$Density*pow(interpolatePositionTable(Table("1mm upstream vel"),
"Velocity[j]"),2)/2/L
:
$Density*pow( ${tan critical angle}*interpolatePositionTable(Table("1mm upstream vel"),
"Velocity[i]"),2)/L
```

Subcritical angle (Eq. 4.12)

```
( ${tan alpha} > ${tan subcritical angle} ) ?
$Density*pow(interpolatePositionTable(Table("1mm upstream vel"),"Velocity[j]"),2)/2/L
:
0
```

where:

'tan alpha' is calculated from the definition

```
abs(interpolatePositionTable(Table("1mm upstream vel"),"Velocity[j]")/
interpolatePositionTable(Table("1mm upstream vel"),"Velocity[i]")
```

'tan critical angle' is defined as `$tan(`α_c`*3.141592654/180)$`

'tan subcritical angle' is defined as `$tan(`α_s`*3.141592654/180)$`

Appendix B

Appendix C

Appendix D

Appendix E